2017

Analytical Solutions and Multiscale Creep Analysis of Functionally Graded Cylindrical Pressure Vessels

Jasem Amjad Ahmed
Louisiana State University and Agricultural and Mechanical College

ANALYTICAL SOLUTIONS AND MULTISCALE CREEP ANALYSIS OF FUNCTIONALLY GRADED CYLINDRICAL PRESSURE VESSELS

A Dissertation

Submitted to the Graduate Faculty of the
Louisiana State University and
Agricultural and Mechanical College
in partial fulfilment of the
requirements for the degree of
Doctor of Philosophy

in

The Department of Mechanical and Industrial Engineering

by
Jasem Amjad Ahmed
B.Sc., Islamic University of Technology, Gazipur, Bangladesh, 2008
August 2017

ACKNOWLEDGEMENTS

I would like to express my utmost gratitude to my major advisor, Dr. M.A. Wahab for his guidance, motivation, patience, and support throughout this research; I will always be indebted to him. I would also like to express my gratitude to my committee members, Dr. T. Warren Liao and Dr. Ayman Okeil for critically reviewing my research, and providing helpful feedbacks on my dissertation. I would also like to thank the Dean's representative, Dr. Luis Escobar, for accepting to be part of my committee, and providing his support.

I gratefully acknowledge the financial support provided by the LSU Board of Regents in the form of Economic Development Assistantship (EDA) award. Supercomputing facilities provided by High Performance Computing (HPC) at the Louisiana State University are gratefully appreciated.

Finally, I wish to thank my wife, parents, colleagues, and friends especially Dr. Hari Konka, Dr. Mohammed Dewan, Daniel Huggett, Saad Aziz, and Moinul Mahdi for their continuous encouragements, suggestions, and comments.

TABLE OF CONTENTS

LIST OF TABLES

LIST OF FIGURES

ABSTRACT

This study deals with the time-dependent creep analysis of functionally graded thick-cylinders under various thermal and mechanical boundary conditions. Firstly, exact thermoelastic stress, and iterative creep solutions for a heat generating and rotating cylindrical vessel made of functionally graded thermal and mechanical properties are proposed. Equations of equilibrium, compatibility, stress-strain, and strain-displacement relations are solved to obtain closed-form initial stress and strain solutions. It is found that material gradient indices have significant influences on thermoelastic stress profiles. For creep analysis, Norton's model is incorporated into rate forms of the above-mentioned equations to obtain time-dependent stress and strain results using an iterative method. Validity of our solutions are at first verified using finite element analysis, and numerical results found in the recent literature have been enhanced. Investigation of effects of material gradients reveals that radial variation of density and creep coefficient have significant effects on strains histories, while Young's modulus and thermal property distributions only influence stress redistribution at an early stage of creep deformation.

Next, a more realistic model of introducing microscale creep effects into a macroscopic modeling is employed to investigate the creep behavior of functionally graded hollow cylinders. Finite element (FE) simulations are employed to evaluate the position-dependent parameters associated with creep constitutive law at the microscale. A macroscopic FE model solves the non-linear boundary value problem to determine the time-varying creep stresses and strains. The framework proposed is capable of predicting the creep response of functionally graded pressure vessels based on the constitutive behavior of the creeping matrix, and volume fraction profile. Effective creep properties have been computed using three different micromechanical models and the homogenized creep response and its effect on the macroscopic behavior are compared. Considering the computational expenses associated with the large 3D finite element models, the

simple 2D axisymmetric model is able to closely capture the creep behavior in such multiscale methods. Finally, a multi-objective particle swarm optimization algorithm is implemented to minimize the initial stress and final creep strain of functionally graded cylinder subjected to mechanical and thermal loads.

CHAPTER 1: INTRODUCTION

An overview of the dissertation, motivation, background, research objectives and contributions and out an outline of the dissertation are presented in this chapter.

1.1 Motivation

Aerospace and energy production applications require components to withstand high temperature, and demonstrate high strength at the same time. This can be achieved by designing advanced composites by utilizing special characteristics of different materials e.g. combining high strength of metals with high temperature resistance of ceramics. Coating of ceramic layers onto a metal surface leads high stress concentration due to abrupt transition of material properties at the interface, resulting in failure of the coating by cracking, spalling, delamination etc. In order to mitigate these damages, materials with smooth spatial gradient in properties, known as *functionally graded materials* (FGM) were developed in the 1980s by Japanese scientists working on thermal shock in space shuttles.

Hollow cylinders are widely used in engineering applications, often exposed to high stress levels at elevated temperatures. Under these conditions, creep deformations are significant and dictate the useful life of the structures. There is strong need for time-dependent analyses for predicting the performance and life-time of the cylindrical structures. Experimental creep evaluation of composite materials is time-consuming and expensive, so computational techniques become useful in predicting and assessing service life of structures. Although research is being done in analyzing thermoelastic behaviors, and on the steady-state creep response of FGM thick-walled cylinders, time-dependent creep analysis under various boundary conditions remains an active area of interest. Solving creep constitutive equations for FGMs is complicated. For this reason, development of analytical and numerical methods for analyzing creep behavior is of utmost

importance. It is typical in analytical and semi-analytical methods to make restrictive assumptions for material variation in order to simplify solutions. The analytical studies are applicable to limited cases only, and cannot be used directly for quantitative evaluation in design and decision making. This limitation can be overcome by moving towards advanced multiscale methods by unifying the creep behavior of FGMs at the microstructural level to the stress-strain response at the macroscale.

The dissertation has two major objectives. The first is to develop analytical solutions for thermo-elastic, and time-dependent creep deformations for FG thick-walled cylinders exposed to various thermal and mechanical loading conditions. An accurate analytical model contributes towards qualitative understanding of creep deformations of FG cylinders, and in numerical validation of advanced computational models. The second objective is to present a multiscale framework to predict and implement local creep behavior of the FGM it the macro body to obtain numerical solutions for FGM cylinders. This research is expected to significantly extend the current ability to incorporate creep deformations into the design of FG thick-cylinders, which are potential structural components operating under severe conditions. The models are beneficial to investigate the choice of material combinations and heterogeneity profiles, thereby reducing cost of materials, fabrication, testing associated with experimental trials.

1.2 General background

1.2.1 Functionally graded materials (FGMs)

FGMs are advanced composite materials of two or more constituents, tailored to exhibit a smooth variation of composition or microstructure with location. Advances in manufacturing techniques have allowed material ingredients to be combined and its composition engineered in ways to make the best use of properties unique to each constituent. This means that design

engineers have a wider choice of potential materials to meet functional requirements of applications, specifically under severe environments. Figure 1.1 shows a representation of a FG microstructure. There is a gradual transition from one constituent to another.

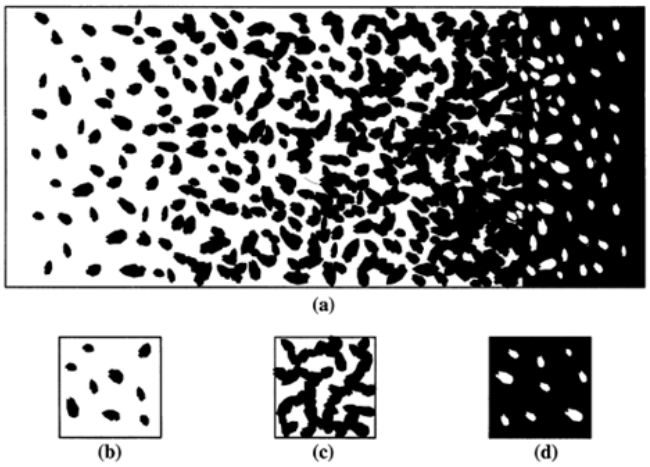

Figure 1.1: Representation of a FG microstructure [1]

FGMs take their motivation from natural structures such as bamboo, bone etc. Figure 1.2 shows the interior structure of bamboo. The gradual property variation is formed by varying chemical composition, microstructure etc. with location. Thus, components can be manufactured for applications where different properties are desired at different surfaces, e.g. a metal-rich side can be used in regions where superior mechanical properties are required, while a ceramic-rich side can be used to withstand high temperatures. The gradient can be built up continuously or in step-wise formation, followed by a consolidation process (drying, sintering or solidification) [2]. It is possible to optimize the material composition profile to extract maximum benefit of the inhomogeneity by minimizing stress-strain levels in a structure developed during both its processing and service life under extreme temperatures. Advantages of functional grading include [3]:

1. Reduced in-plane and transverse through-the-thickness stresses
2. Improved residual stress distribution

3. Reduced stress intensity factors
4. Enhanced thermal properties
5. Higher fracture toughness.

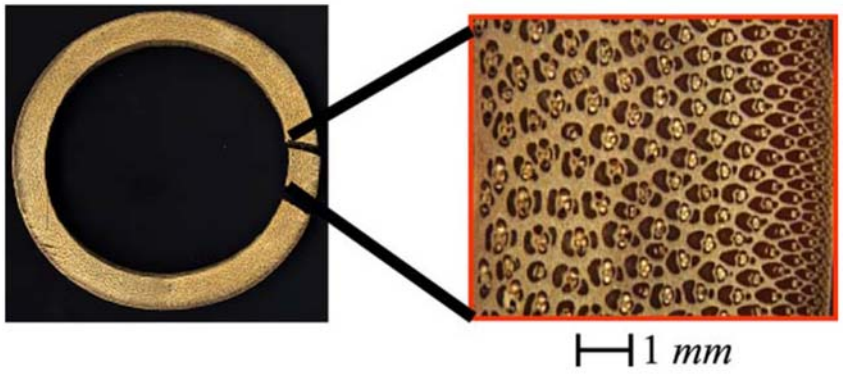

Figure 1.2: Distribution of fibers in bamboo [4], [5]

1.2.2 Potential applications of functionally graded materials

FGMs can effectively reduce thermal mismatch between neighboring materials, and can be used to manufacture components for applications where specific properties are favored at different surfaces. They have tremendous applications in joining dissimilar materials such as ceramics to super alloys for thermal barrier coatings (TBC), gas turbines, turbochargers etc. Plasma divertor designs of the International Thermonuclear Experimental Reactors (ITER) employ tungsten-copper alloy FG components to face high heat flux and efficiently transfer heat to a cooling base. The gradation alleviates high thermal stresses arising due to material property mismatch, and reduces temperature of the cooling base to prevent thermal softening.

Metal matrix composites (MMC) have been considered to fabricate pressure vessels and propellant tanks, providing strength against tensile loading at high pressures, and compressive loading without buckling. These multifunctional vessels can potentially reduce the overall weight, and improve efficiencies for propulsions technologies in aerospace, military, and commercial

systems. Tungsten matrix composite (TMC) pressure vessels are expected to reduce weight, and improve storage quantity by operating at higher pressures, enhance creep resistance, and improve cost savings and revenue as a result of greater operating life. These benefits can also be utilized in sub-sea and chemical operations, where system weight and corrosion are of important concerns. TISICS Ltd. designed titanium-silicon carbide composite pressure vessels and propellant tanks for spacecraft and satellite applications. Burst pressures of more than four times the expected operating pressure were tested. FMW Composite Systems proposed TMC pressure vessels for space-landing missions to Venus. It is important to model and compare the performance, manufacturability, cost, safety regulations of composite vessels to the current state-of-art of pressure vessels. Although initially developed as heat resistant materials for high temperature applications such as spacecraft, nuclear plants, FGMs also have potential usage in orthopedic and dental implants, fuel cells, blast protection systems, electromagnetic and piezoelectric sensors/actuators etc.

1.3 Research topics of FGMs

Several critical areas need to be addressed before FGMs can be extensively used. These are: i) fabrication and processing, ii) translation of local microstructure into macroscopic properties, iii) mathematical modeling to investigate structural responses under various conditions, and iv) optimization of material properties.

Most commonly considered FGM structures are plates, disks, beams, hollow cylinders, spheres, and films on metal surfaces. Due to differences in thermal expansivities, cooling from high temperatures (1100-1700 K) to room temperature will cause different regions to shrink to different extents, giving rise to residual stresses during fabrication processes. Typically, structures are solved for steady state or transient temperatures and residual stress profiles from temperature

loadings, thermal shock, and thermal cycling etc. In many cases, the critical bucking temperatures (temperature difference between the maximum heated temperature and initial temperature at which bucking starts) are investigated [6]. Commonly used mathematical procedures in analyzing behavior of FGMs are:

1. Analytical/semi-analytical methods restricting boundary conditions and gradation to special cases
2. Perturbation method
3. Finite Element Method (FEM)
4. Boundary Element Method (BEM)
5. Meshless methods
6. Higher-order discretization methods.

Sometimes the nature of function describing the inhomogeneity makes the governing equations very long and tedious. The difficulty is avoided by using a multi-layered method i.e. assuming the structure to be made of numerous homogenous sub-layers with continuity relations. When the number of layers is very large, the solutions will approach that of a continuously graded one. The finite element method (FEM) is extremely useful in analyzing complex material gradation, boundary conditions and non-linear material behavior (elastoplastic, creep etc.). However, this may come with significant computational cost due to discretization of the domain.

1.3.1 Functionally graded pressure vessels

Hollow cylinders are one the major structural components in many engineering applications. Examples are pressure vessels for aerospace vehicles or shuttles used in reentry to earth's atmosphere, nuclear reactors, military applications, and storage and transmission of pressurized chemical and fluids, boilers etc. In many cases, they are required to withstand high

temperature environments for sustained period of thermal loads causing significant creep damage which may trigger catastrophic failures. For extreme conditions, structures could be designed FGMs to alleviate damaging effects. A gradual property variation is usually formed by varying chemical compositions, mechanical properties, and microstructures, etc. with location. FGMs can effectively reduce thermal mismatch between neighboring materials, and can be used to manufacture components for applications where specific properties are favored at different surfaces to mitigate detrimental effects of severe environments. Temperature and stress solutions of engineering structures are of fundamental importance from a design point of view, as well as, in-service fitness assessment. Creep accumulation is a leading cause of crack initiation in components working at high temperatures. Evaluation of creep stresses and strains is essential in design, and as well as fitness analysis of aging structures. Successful implementation of the FGM technology into pressure vessel components necessitates the need for a comprehensive study for structural response. This is relatively new area of research and so far, experimental efforts have been quite limited, and needs innovative thinking and critical analysis and assessment of the materials properties and design loads understanding.

1.3.2 Creep damage in materials

Creep is an important material behavior occurring at elevated temperatures, especially at that higher than 50% of the melting temperature of the material. It is the time-dependent, inelastic deformation taking place when the material is subjected to a load over time. A structure undergoes changes in state of stress and strains, reduction in material strength etc. The deformation is commonly characterized in the form of strain versus time data, known as the creep curve. There are three regions in the creep curve: i) primary, ii) secondary), and iii) tertiary regions, as shown in Figure 1.3.

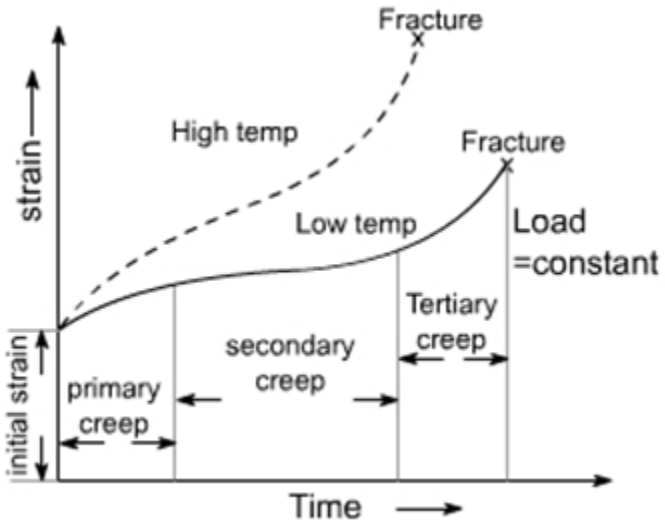

Figure 1.3: A typical creep curve showing variation of strain with time

The primary creep stage is characterized by an initial high creep rate which decreases with time. Eventually a secondary stage is attained at which significant deformation takes place at a constant rate. At the tertiary stage, the creep rate begins to increase leading to rupture due to necking and formation of cavities. Figure 1.3 highlights the three regions in a typical creep curve. Primary creep occurs in a short interval of time, and cylinders are mostly subject to secondary creep effects during their useful lifetime. Tertiary creep is usually not considered because it indicates imminent failure.

1.3.3 Multiscale analysis of functionally graded structures

FGMs allow spatial customization of material properties in order to derive maximum benefits from constituents with wide variation in properties. Several analytical and semi-analytical solutions FG cylinders have been developed based on restrictive assumptions. A widely-used assumption is the usage of separate power-law formulae for thermal, elastic and creep properties. In reality, correlation between the properties exist, and it becomes impractical to restrict these using such profiles. Detailed finite element models generated with microstructural inhomogeneity inside the macroscopic structure are limited by computing capacities. Multiscale numerical

techniques become extremely useful to predict the macroscopic behavior of FG structures, as these can be used to first evaluate location-dependent properties based on compositions. With limited FGM experimental progress, numerical models provide a driving force in comprehension the fundamentals in the field. To date, multiscale creep analysis of FGMs have not been investigated. A method is proposed in this dissertation is well suited for analyzing creep behavior of FG cylinders. An objective of this research is to develop a framework for generating two phase unit-cells to estimate creep properties over a range of volume fractions, and thereby using the information to predict the macroscopic time-dependent behavior of FG thick-walled cylinders. Optimization schemes could be later employed to determine the best spatial variation of material properties that would minimize creep deformation while taking stress constraints into considerations.

1.3.4 Estimation of FGM properties

Over the last two decades, significant amount of work is being done concerning the thermoelastic analysis of FGMs. Many times, the material properties of FGMs are assumed using simplified mathematical expressions e.g. power-law, exponential, piecewise linear, sigmoidal functions etc., facilitating closed form analytical, or numerical solutions to be derived. There are also several techniques to establish relationship between microscopic and macroscopic properties. Effective properties of FGMs are usually estimated from volume fraction and shape of dispersed phase. It is not always possible to obtain complete size, shape and particle distribution of the whole structure. Microstructure morphology would also depend on the volume fraction of constituents, as the matrix and particulate phases may be clearly defined only for low and high particulate volume fractions, while forming interconnecting networks for intermediate values [7]. The possibility of investigating material properties at smaller scales to establish a connection with the

microscopic structure has made multiscale modeling appealing. This idea has been implemented using homogenization schemes in the case of elastic, thermal properties etc. Creep data of metal-matrix composites are limited in the literature, and the experimental determination of creep parameters for a range of volume fractions, and stress levels and temperatures would be extremely labor and time intensive. Few numerical works focus their attention in understanding the creep properties of heterogeneous materials. Evaluation of effective material properties are further elaborated in the upcoming Section 2.2.1.

1.3.5 Optimization of FGMs

As thermally-induced stresses during fabrication and in-service are greatly influenced by the gradation shape, it is important to optimize the composition profile. Usually, an initial composition profile is selected as basis of optimization, and the stress, strain and temperature profiles are evaluated and assessed according to a design criterion e.g. based on critical temperature, magnitude of stresses, fracture toughness etc. The composition profile is varied using iterative procedures until an optimal objective function value is obtained. Metaheuristics such as *genetic algorithm, particle swarm optimization, differential evolution* etc. are generally used to facilitate the optimization process.

1.4 Overview of dissertation

The problem description, contributions of this study, and the dissertation layout are summarized here.

1.4.1 Problem description

Functionally graded thick-walled cylinders are considered in this study. Cylinders with different material gradation profiles are exposed to mechanical loadings such as internal/external pressures, and rotation, and thermal loadings due to internal heat generation, and temperature differences in convective environments. Other assumptions include: i) infinitely long cylinders, ii) temperature-independent material properties, and ii) incompressibility in the creep regime. The first portion develops of a semi-analytical formulation assuming individual material distributions varying according to a power-law profile. Next, a multiscale finite element framework is developed, incorporating primary and secondary creep characteristics of the material matrix using a combined time-hardening law.

1.4.2 Research contributions

Firstly, closed-form solutions for the thermoelastic response of a FG thick-walled cylinder are developed. The proposed solution pertains to different mechanical and thermal boundary conditions: internal and external pressures, rotation, heat transfer under convective environments, and internal heat generation. Non-steady creep solutions for the above problem is introduced. A finite element model is verified with the analytical solutions. A multiscale method is then employed to link local creep properties predicted from micromechanical models to the finite element macromodel to investigate the time-dependent behavior of a FG hollow cylinder.

1.4.3 Dissertation outline

The dissertation is organized in the following order. Chapter 2 details existing literature relevant to creep studies of FG thick-walled cylinders. Chapter 3 presents the research problem,

formulation of governing equations, and derivation of closed form analytic solutions for thermoelastic stress-strains, and iterative creep solutions. A finite element model built using ANSYS [8] is validated with the creep solutions. Chapter 4 employs a multiscale framework for creep analysis at the micro and macro scales. Chapter 5 presents parametric studies and results obtained from the: i) analytical solutions, and ii) multiscale method. Finally, concluding remarks, on-going work, and possible future research are discussed in Chapter 6, followed by references at the end of the dissertation.

CHAPTER 2: LITERATURE REVIEW

In the last decades, research has been going on in order to better understand responses of *functionally graded* (FG) cylindrical vessels. *Functionally graded materials* (FGM) have tremendous potential to work in extreme thermal and high-pressure applications. An overview of the state of art knowledge relevant to the proposed creep analyses of FG thick-cylinders is presented in this chapter. The review is divided into two major categories, one of which deals with the derivation of semi-analytical solutions, while the other highlights the development of multiscale methods.

2.1 Analytical and semi-analytical solutions for functionally graded (FG) cylinders

Most work found in the literature are dedicated to the derivation of analytic and semi-analytic solutions for stresses and strains. Three different gradation profiles have been widely adopted in the literature: i) exponential-law, ii) power-law, and iii) sigmoid-law. Numerical methods are also used due to complexity involved in analytical solutions. In an extensive review paper, Dai, et al. [9] gathered together research articles published on the coupled mechanics of FG cylindrical structures from 2005 to 2015.

2.1.1 Elastic behavior of functionally graded cylinders

A number of researchers have investigated functionally graded hollow-cylinders exposed to pressure loading only. Tutuncu and Ozturk [10] obtained closed-form stress and displacement solution for FG cylindrical and spherical vessels subjected to internal pressure. Xiang, et al. [11] studied the elastic behaviors of multi-layered, and continuously graded hollow cylinders applying Whitaker, and hypergeometric equations. Tutuncu [12] obtained power series stress and displacement solutions for FG cylindrical vessels subjected to internal pressure. Chen and Lin [13]

performed elastic analysis of a FG thick-cylinder with exponential Young's modulus profile. Tutuncu and Temel [14] determined axisymmetric displacement and stresses in FG hollow cylinder, disks, and spheres subjected to internal pressure using plane elasticity theory and complimentary functions method. A boundary value problem was transformed into an initial value problem and solved using the Runga-Kutta method. Li and Peng [15] studied the elastic analysis of a pressurized FG tube considering arbitrary material properties by forming a Fredholm integral equation and solving as a series of Legendre polynomials. Afshar, et al. [16] studied the viscoelastic behavior of FG cylinders using ANSYS. Sburlati [17] obtained analytical solutions for thick-walled cylinders with internally FG coatings subjected to pressures. Nejad, et al. [18] studied a semi-analytical solution of non-uniform pressure loading of a FG rotating thick-cylinder with variable thickness and clamped ends using a multi-layers method based on first order shear deformation theory. These articles have only investigated elastic behaviors of FG cylinders.

2.1.2 Thermoelastic behavior of functionally graded cylinders, spheres

Considerable amount of studies has been performed to obtain the response of FGM cylinders under temperature and pressure loadings. Tarn [19] determined temperature and thermoelastic deformations and stress fields for FG cylinders subjected to axial force, torque at ends, circumferentially varying surface loads, rotation etc. Jabbari, et al. [20] formulated analytical solutions for one-dimensional steady state thermal stress distributions considering power law gradation of elastic and thermal material properties. The boundary conditions acting on the thick-cylinder were internal and external pressures, with different ambient temperatures with convective heat transfer. No internal heat generation was considered, which would otherwise have a direct effect on the temperature and stress distributions of the cylinder. Liew, et al. [21] developed thermoelastic solutions for FG cylinders subjected to arbitrary steady or transient temperature

distributions considering large number of homogeneous layers. Ruhi, et al. [22] presented a semi-analytical thermoelasticity solution for FG thick-walled finite-length cylinders. Two-dimensional axisymmetric thermal and mechanical loads in short FG radially graded cylinder were investigated by Shao [23], and Jabbari, et al. [24], and long FG cylinder by Jabbari, et al. [25]. Pelletier and Vel [26] analyzed the steady-state response of FG thick cylindrical shell with orthotropic material properties varying arbitrarily in the radial direction subject to thermal and mechanical loads using a multi-layer technique. Kordkheili and Naghdabadi [27] studied thermoelastic response due to pressure, thermal, and axial loadings. Shao, et al. [28] obtained analytical time-dependent temperature and thermomechanical stress solutions for FG hollow cylinders subjected to non-axisymmetric mechanical and transient thermal loads using complex Fourier series and Laplace transform techniques. Peng and Li [29] proposed a numerical method for the thermoelastic solutions for arbitrarily varying properties (without specified gradient form). Zhang, et al. [30] derived an analytical solution to determine the thermo-mechanical stresses in multi-layered FG cylinder considering the influence of closed-ends. Mehrabadi and Aragh [31] investigated FG cylindrical shell with 2-D power law property distribution with temperature dependency. Xin, et al. [3] solved a similar problem, assuming the FGM as a combination of two constituents, and using a power-law assumption for the relative volume fraction. All studies dealt with thermoelastic stress analysis without considering internal heat generation. Leu and Chien [32] studied thermoelastic behavior of graded disks with variable thickness and non-linear heat generation using finite element and symbolic computations software. However, the solutions do not hold when the temperature profile is altered by internal heat generation within the structure.

2.1.3 Elastoplastic behavior of functionally graded cylinders

There are a few studies pertaining to elastoplastic behavior of FG cylinders and spheres. Eraslan [33] presented analytical solutions for thermally induced axisymmetric elastic and elastic-plastic deformations in non-uniform heat generating FG tubes with fixed ends, and different inner and outer boundary conditions. Eraslan and Akis [34] obtained elastic-plastic solutions for pressurized FG tubes. Heat generating FG solid cylinder was considered by Ozturk and Gulgec [35] in an elastic-plastic deformation study assuming parabolic material profile. Parvizi, et al. [36] presented analytical elastic-plastic solution for FGM cylinders subjected to internal pressure and thermal gradient. Nejad and Fatehi [37] obtained exact elastoplastic deformations and stresses of rotating thick-walled cylindrical pressure vessels made of FGMs assuming perfectly plastic behavior based on Tresca's yield criteria.

2.1.4 Piezo-electric, and magneto behaviors of functionally graded cylinders, discs

A few articles could be found in which piezo-electric and magnetic properties were taken into account in FG cylinders. Khoshgoftar, et al. [38] studied the thermos-piezoelectric behavior of thick-walled FG cylinders subjected to temperature gradient and uniform pressures. Dai, et al. [39] performed an analytical study on the electro-magneto-thermoelastic behaviors of a FG piezoelectric hollow cylinder, subject to uniform magnetic field, electric, thermal and mechanical loads. Dai, et al. [40] determined an exact solution for stresses and magnetic field vector perturbations for a FG hollow cylinder subjected to uniform magnetic field, thermal, and mechanical loads. Arani, et al. [41] investigated the thermo-piezo-magnetic behavior of a FG cylinder under mechanical and thermal loads. Bayat, et al. [42] studied the magneto-thermo-mechanical response of FG disc with variable thickness, subjected to uniform magnetic field and

thermal load. Zenkour [43] obtained an analytical solution for the hygrothermal response of a FG piezoelectric hollow cylinder subjected to a mechanical load and an electric potential. Atrian, et al. [44] presented an analytical thermo-electromechanical solution for thick-walled FG piezoelectric cylinders subjected to uniform electric field and non-axisymmetric thermo-mechanical loads.

2.1.5 Creep behavior of functionally graded vessels

At elevated temperatures creep responses are usually dominant and determine the failure of structures. Creep analysis of FG pressure vessels is complex, and there are some publications dealing with the subject. You, et al. [45] calculated stresses and creep strain rates in a thick-walled cylindrical FG vessel subjected to internal pressure by considering Norton's creep law parameters as functions of radial coordinate. You and Ou [46] proposed an iterative method to evaluate creep strain rates and stresses for a pressurized FG thick-sphere. Steady state creep behavior under internal pressure was investigated by Singh and Gupta [47], [48]. Chen, et al. [49] investigated creep effects of a spherical FG tank subjected to internal/external pressure only. Young's modulus and creep parameters were expressed using power functions but thermal effects were not included in that studies. Nejad, et al. [50] developed a closed-form analytical solution for steady-state creep stresses of rotating thick cylindrical pressure vessel made of FGM. The effect of different parameters in the Norton's creep law on the radial and circumferential stresses, and equivalent strain-rate were investigated. A limitation of these published articles is that they deal with a situation after a steady-state has been attained, and do not reveal the time-dependent responses. A difficulty associated with this is that the stresses, and rate of creep damage varies with time. For comprehensive analysis, the determination of stress history is inevitable.

A few articles are dedicated to the time-dependent creep deformation in FGM cylinders and spheres. Yang, et al. [51] presented elastic and asymptotic creep solutions for a FG cylinder under various axial constraints. The coefficient of thermal expansion (CTE) and temperature distribution were combined together to restrict the thermal dilation to special power-law case. Time-dependent creep behavior of a FG cylinder under internal and external pressures was studied by Chen, et al. [52]. Time-dependent creep redistributions of FG cylinders due to internal pressure under uniform magnetic and thermal fields was studied by Loghman, et al. [53]. Singh and Gupta [54] investigated the steady state creep of transversely isotropic SiC_w-Al6061 FG cylinder under internal and external pressures. A threshold based creep law was used in which the creep parameters were estimated by linear extrapolation of experimental uniaxial creep results. Loghman, et al. [55] studied time-dependent creep stress redistribution of a FG thick-walled sphere subjected to internal pressure and constant temperature field. An iterative procedure based on the recalculating stresses and creep strain increments after short time intervals was used. Loghman and Moradi [56] studied time-dependent creep response of a FG piezoelectric sphere subjected to internal pressure, uniform temperature, electric potential and magnetic field. Fesharaki, et al. [57] considered a similar problem with internal/external pressures and temperature gradient with graded material properties based on volume percentage.

Nejad and Kashkoli [58] investigated time-dependent thermoelastic creep response for a rotating thick-walled FG cylindrical pressure vessel under plane stress and plane strain conditions. However, the study's illustrative example indicates violation of necessary boundary conditions. Figure 2.1 illustrates radial stress distributions along the cylinder thickness published in the article's Figures 2a, 6a, 8a and 12a. To counterbalance constant applied pressures at all times, radial stresses at inner and outer surfaces must remain constant corresponding to the applied values

regardless of creep or material exponents. However, unusually high stress values are noticed in the results, and radial stress distributions appear to violate imposed mechanical boundary conditions, suggesting impractical solutions. It is to be noted that the values were normalized by the internal pressure applied. An objective of this project is to correct, and improve the analytical model for time-dependent creep deformations of FG hollow-cylinders under various thermal and mechanical boundary conditions.

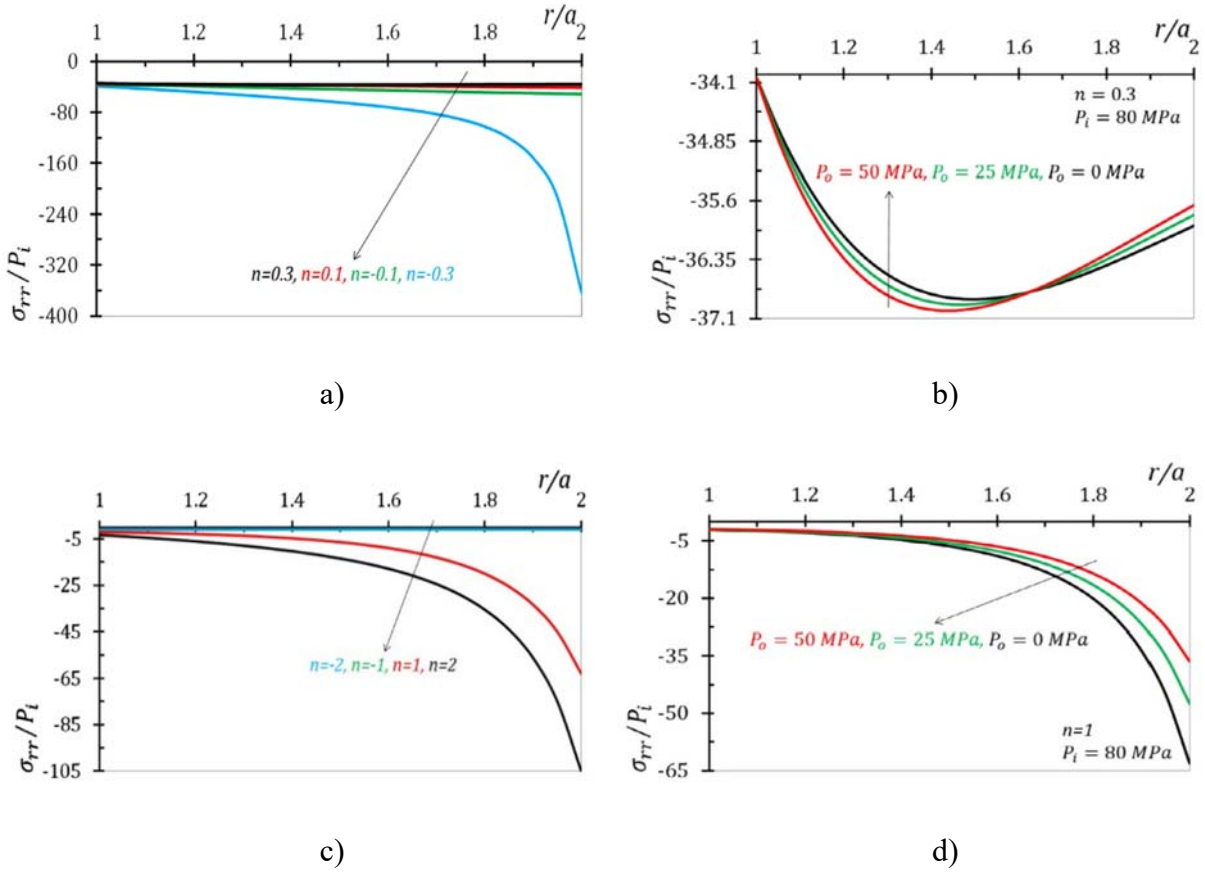

Figure 2.1: Radial stress distribution after 10 h of creep for a) different material exponents under plane strain, b) added external pressure under plane strain, c) different material exponents under plane stress, and d) added external pressure under plane stress

2.1.6 Miscellaneous topics

Some researchers have concentrated on creep of studies of non-cylindrical structures. Qu, et al. [59] simulated the fabrication and operation phases of Tungsten-EUROFER FG systems

using finite element analysis. Creep assessment was performed to investigate the influence of the FG layer on residual stresses and creep accumulation. Tungsten coated EUROFER have been widely considered to be used a structural material for first wall of future power plants. Golmakaniyoon and Akhlaghi [60] investigated the time-dependent steady-state creep of FG beams subjected to thermal loading using a successive elastic solution method. Thermal stress and curvature of the beams were predicted to decrease with time.

Heat generation within hollow cylinders are common in many engineering applications. In nuclear plants, γ-rays emitted from the reactor cores are absorbed by pressure vessels, resulting in volumetric heat generation of the vessel. The vessels are cooled by fluids at their inner and outer surfaces. Limited studies have been conducted, for example, on the temperature and stress/strain responses for homogenous cases. Goshima and Miyao [61] studied transient thermal stresses resulting from internal heat generation due to γ-rays, and convective cooling at inner and outer surfaces. Heat generation was assumed to decay exponentially along the radius. Aziz and Torabi [62] considered a hollow cylinder with convective surfaces and uniform heat generation. Analytical solutions derived in the study serve as references to validate further complicated cases, and illustrates the effects of boundary condition parameters on stress distributions.

Although these recently published studies have widened the understanding of behavior of cylinders, but restricting temperature field to uniform profiles may have limited applicability to structures where internal heat generation is of primary concern. Thus, in this research we attempt to expand the studies about thermo-elastic, and time dependent response of hollow cylinders by the including internal heat generation in convective heat-transfer environments. The research also corrects existing solutions found in recent literature as mentioned in Section 2.1.5.

Current studies are only able to calculate the secondary creep characteristics of FG cylinders by assuming power-law profile for the creep coefficient. In reality, the creep parameters do not limit themselves to such profiles, and often vary by orders of magnitudes within the graded structure. To expand the research area by eliminating limitation of assuming specific creep models and parameter variation, a microscopic finite element (FE) based creep evaluation technique is used in conjunction to a macroscopic FE model of the FG cylinder. Although creep models of metal matrix composites have been previously investigated, they are yet to be addressed in multiscale creep models of FGMs.

2.2 Multiscale modeling of functionally graded materials

FGMs are considered as a special class of metal matrix composites (MMC). Particle reinforced MMCs are preferred due to their low costs, fabrication ease, and high isotropic nature. They demonstrate higher elastic modulus, tensile strength, and temperature stability, but lower ductility, fatigue and fracture properties than their monolithic alloy counterparts. The overall properties depend upon several factors such as volume fraction, interfacial behavior, size, orientation, and aspect ratio of particles. Large difference in length scales between micro and macrostructures, and the problem of spatial variation makes FGM modeling difficult. Multiscale methods are capable of addressing the issues by employing effective property models, or combined macroscopic-microscopic models such as asymptotic methods, or nested boundary value homogenization problems [63]. The effective property models use homogenization techniques of particle-reinforced composites for the determination of elastic and thermal properties for a range of composition. Effective properties are assigned to regions inside FGMs whose composition vary noticeably. Homogenization techniques of creep are only focused only at the micro-level by modeling particle-reinforced MMCs. Such techniques have not been considered in creep studies

of FGMs, and there is a significant scope to improve FGM creep studies by the integration of micromechanical models. Multiscale methods have been widely used in engineering applications. FE based multiscale modeling was used by Li, et al. [64] to represent sub-micron precipitate structure on tempered martensitic steel. Ubachs, et al. [65] developed a global-local multiscale technique to assess multilayer substrates in microelectronic packages.

2.2.1 Evaluation of effective material properties of two-phase composites

Behavior of composites have been primarily estimated using rules of mixture (Voigt and Reuss estimates), modified rules of mixture (TTO scheme), mean field mechanics (Eshelby, Mori-Tanaka [66], self-consistent scheme [67] etc.), theoretical bounding methods (Hashin-Shtrikman lower and upper bounds [68]), and computational simulations (finite or boundary element methods). Rules of mixture are mathematically simple, and are widely used to determine physical properties such as Young's modulus, Poisson's ratio, thermal conductivity, coefficient of thermal expansion, density, specific heat etc. As inclusion percentage increases, interaction between neighboring particles become significant, and influence the effective properties of the composite. ROM fails to incorporate particle interaction into calculations. There are also differences between the Voigt and Reuss estimates for volume fractions not close to 0 or 1, thus constituting upper and lower bounds of the material behavior. The Mori-Tanaka scheme considers spherical reinforcements within a matrix, and accounts for interaction of fields between neighboring particles. The Hashin-Shtrikman model uses variational principles to establish bounds by incorporating phase arrangements. The self-consistent method assumes ellipsoidal particle embedded in a matrix. Large disparity exists between the upper and lower bounds when the material properties are significantly different, and self-consistent methods may not be reliable for such cases. Thus, it is important to model the microstructure more realistically rather than

assuming that the homogenization techniques will yield accurate estimations. However, it is to be noted that the schemes are easier to implement, and lead to reduction of computational time and effort. Commonly used homogenization techniques using for FGMs are tabulated in Table 2.1.

Table 2.1: Commonly used homogenization techniques

Scheme	**Material Property**	**Related Equations**
Mori-Tanaka [66]	Bulk and shear moduli	$\frac{K-K_1}{K_2-K_1}=\frac{V}{1+\frac{(1-V)(K_2-K_1)}{K_1+\frac{4}{3}\mu_1}}$ $\frac{\mu-\mu_1}{\mu_2-\mu_1}=\frac{V}{1+\frac{(1-V)(\mu_2-\mu_1)}{\mu_1+f_1}}$ $f_1=\frac{\mu_1(9K_1+8\mu_1)}{6(K_1+2\mu_1)}$
Hatta-Taya [69]	Thermal conductivity	$\frac{k-k_1}{k_2-k_1}=\frac{V}{1+\frac{(1-V)(k_2-k_1)}{3k_1}}$
Rosen-Hashin [70]	Coefficient of thermal expansion	$\frac{\alpha-\alpha_1}{\alpha_2-\alpha_1}=\frac{\frac{1}{K}-\frac{1}{K_1}}{\frac{1}{K_2}-\frac{1}{K_1}}$
Self-consistent method	Bulk and shear moduli	$\frac{(1-V)K_1}{K_1+\frac{4}{3}\mu}+\frac{VK_2}{K_2+\frac{4}{3}\mu}+5\left[\frac{(1-V)\mu_2}{\mu-\mu_2}+\frac{V\mu_1}{\mu-\mu_1}\right]+2=0$ $K=\frac{1}{\frac{1-V}{K_1+\frac{4}{3}\mu}+\frac{V}{K_2+\frac{4}{3}\mu}}-\frac{4}{3}\mu$
Self-consistent method [71]	Thermal conductivity	$\frac{(1-V)(k_1-k)}{k_1+2k}+\frac{V(k_2-k)}{k_2+2k}=0$

Depending on the fundamental assumptions incorporated in a homogenization technique, determination of closed-from solutions can become too complex, especially when non-linearity is considered. For such cases, computational analyses can be performed by either simulating RVEs of heterogeneous materials into ideal microstructures using regular shapes (spheres, ellipses, cylinder etc.) or using real digital images. Common microstructures used are ensembles of impenetrable and penetrable spheres, randomly sized and oriented elliptical reinforcements, 2D or 3D grids of finite elements, grids of rectangular or voxel shaped finite elements.

2.2.2 Homogenization of representative volume elements (RVE)

Evaluation of microstructural materials properties is of significant interest for the development of MMCs. Such composites may fail through fiber or particle cracking, inclusion-matrix debonding, and brittle and ductile fracture in the matrix. Morphological features such an inclusion size, spacing, directionality, clustering etc. affect the initiation and propagation of damage. With the development of FG MMCs, it is important to analyze the material properties of various compositions. As the material is especially considered for high temperature applications, determination of steady state creep rate is of tremendous importance for the evaluation of reliability of the structure to be designed. Experimental methods to predict material behavior are labor and time intensive, and so numerical techniques are developed to model the structure. Solving a problem at the characteristic length of inhomogeneity (e.g. 50 μm) requires very high computing power. So, material properties are usually homogenized over domains l much larger than the microscopic resolution d, but considerably smaller than the overall loaded structure L. The region over which the macroscopic properties are evaluated is known as a *representative volume element* (RVE). If the length scale requirement $d \ll l \ll L$ is satisfied, the estimates would be applicable for both homogenous, and heterogeneous microstructures. Small unit-cells can accommodate

single particles, or multi-particles to include interactions between particles. Different types of single inclusion RVEs found in the literature are: i) cylindrical, ii) square, and iii) hexagonal. Square and hexagonal RVEs are thought to give best estimations due to their ability to fill up space compared to the cylindrical RVE. Cylindrical RVEs tend to overestimate elastic modulus compared to the square RVE. However, cylinder RVEs are widely used because these can be modeled using 2D axisymmetric finite element model to minimize computational expenses. Analytical/semi-analytical solutions are also available in simple cases. In multi-particle RVEs, the particles can be uniformly distributed or randomly dispersed.

A lot of work has been dedicated in predicting the material properties of regular and random microstructures. Regular microstructures simplified into single particle unit cells do not include the statistical nature of phase distribution. For random morphologies, studies assume regular particles randomly dispersed in a homogeneous matrix. In reality, microstructures may contain of irregular inclusions when particle volume fraction is low, and interconnected skeletal microstructures (matrix or inclusion phases are not clearly defined) for similar particle and matrix percentages. Numerical techniques such as the finite difference method, finite element method, meshless method etc. are required when analytical solutions for governing equations become tedious. Single unit cell models with periodicity may lead to analytical solutions, but are not realistic as they do not represent the random distribution of inclusions, and are limited to very specific microstructure. Therefore, a *statistical representative volume element* (SRVE) is needed to reproduce the microstructural behavior of real materials. As SRVE is a volume that is large enough to be statistically representative of all microstructural heterogeneities in a composite material. Homogenized properties fluctuate with varying RVE sizes, but in order for an RVE to exist, the properties should converge with increasing size. A critical length above which the

macroscopic properties are accepted to remain steady is referred to as the minimum RVE length. A numerical model smaller than the critical size leads to incorrect estimations. The macroscopic properties should also be independent of the applied boundary conditions. RVEs have been extensively combined with finite element analysis (FEA) to correlate effective properties of composites with the properties of constituents and microstructures of the materials. A larger size of RVE allows more microstructural randomness to be contained within identical microstructures, and gives a more accurate estimation. The technique becomes computationally expensive, and so it is crucial to determine the minimum size of RVE to reduce computation time.

Generation of an RVE requires prior determination of spatial arrangement of particles. Regularly arranged particles are easy to generate, but leads to incorrect predictions e.g. underestimation of damage initiation and matrix cracking. The *random sequential adsorption* (RSA) algorithm is commonly used to generate random, non-overlapping particles, and are able to include the effect of non-uniform spatial distribution of inclusions. Llorca and Segurado [72] predicted the elastoplastic behavior of elastic particle reinforced metal matrix composites, taking into account damage induced by void nucleation and growth. However, the hard-ball model is constrained by a jamming limit, and microstructure with high inclusion volume fractions cannot be generated. Kari, et al. [73] were able to evaluate overall elastic properties of spherical particle reinforced composites for volume fractions up to 60% using numerical homogenization based on finite element method. 3D RVE models were generated using the modified RSA algorithm. Spherical particles with different sizes were used to achieve high volume fractions, which are not possible with monodisperse particles. RVE geometry and meshes used in their study are shown in Figure 2.2.

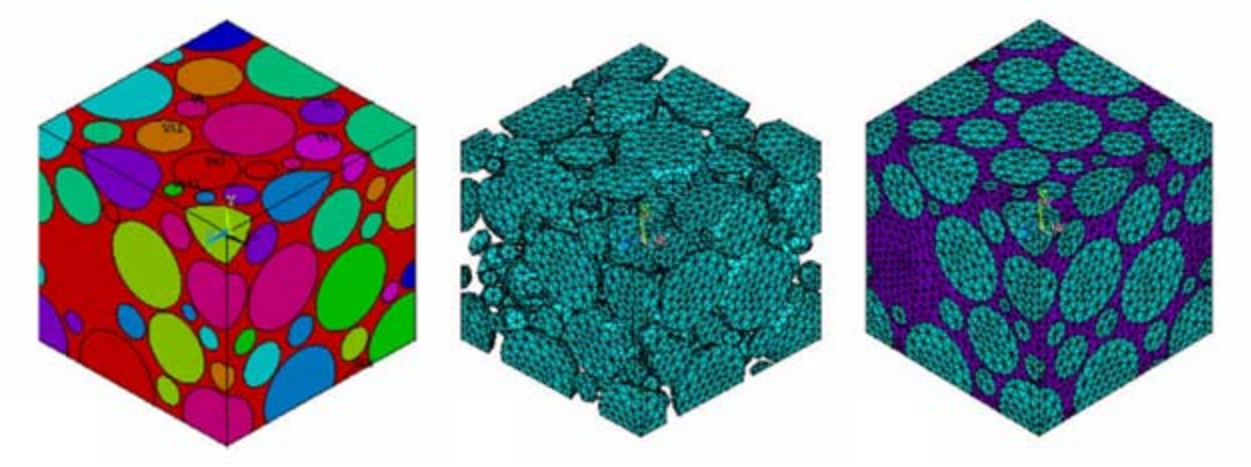

a) b) c)

Figure 2.2: High-volume fraction (60%) RVE [73]: a) geometry, b) particle mesh, and c) composite mesh

Effective elastic properties were calculated as ratios of average stresses and strains under periodic boundary conditions. The influences of particle size and RVE length on the effective composite properties were investigated. Error values in effective elastic properties were less than 1% for RVE sizes greater than 10/3 times of particle diameter (monodisperse). With sufficiently large RVEs, there were no significant fluctuations in elastic properties with different particle diameters. Values were also identical for models with monodisperse and polydisperse (random size) particles. Figure 2.3 shows the variation of Young's modulus with RVE size, and comparison with monodisperse and polydisperse particles. The technique has been used to generate high volume fraction RVEs in the present study. Yang et al. [74] presented a random sequential expansion (RSE) method to overcome the hard-ball model jamming limit, and generated RVEs with high fiber volume fractions. Fiber generation started from the center of the RVE and the microstructure expanded radially based on two parameters: a random orientation direction between 0 and 360°, and a randomly chosen inter-fiber distance depending upon the required volume

fraction. Statistical analyses demonstrated spatial randomness and isotropy, and elastic properties predicted using FEA of the microstructure were verified with experimental results.

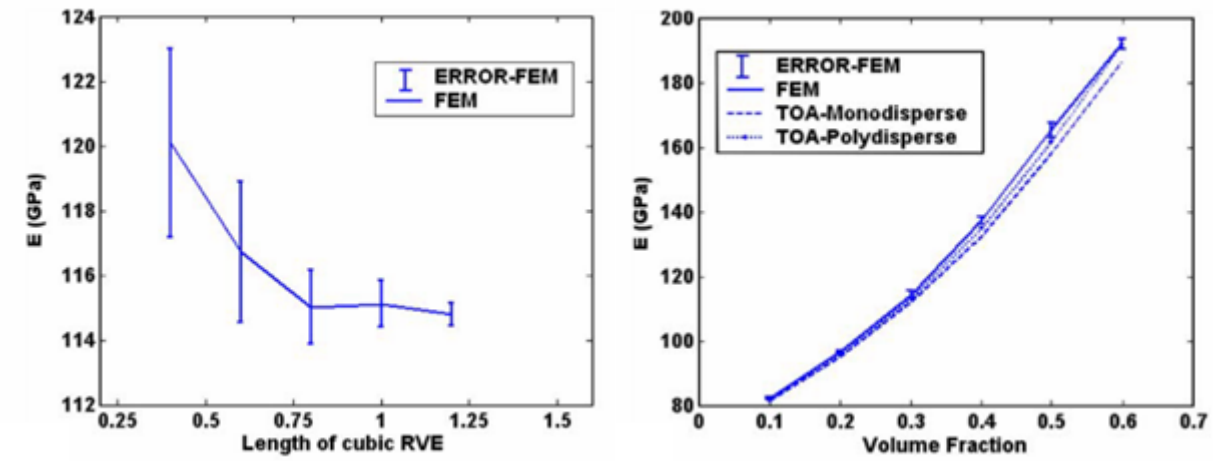

a) b)

Figure 2.3: a) Variation of Young's modulus with RVE size, b) Comparison of Young's modulus for monodisperse and polydisperse particles

Casting and powder metallurgy have been widely used in manufacturing MMCs. After thermomechanical processing, micro-stresses arise at the grain-size scale due to mismatch in coefficient of thermal expansion (CTE) of matrix and reinforcements. Presence of internal residual stresses degrades mechanical properties of the composite via crack initiation and propagation at the interfaces. Bouafia, et al. [75] used finite element analysis to study the effects of particle spacing, volume fraction, particle interaction and particle shape thermal residual stress distributions in SiC particle reinforced aluminum composites. A 3D unit cell model was cooled down at a constant rate from the processing to room temperatures to simulate manufacturing, and then reheated to a high temperature to model in-service environments. Alfonso, et al. [76] calculated the Young's modulus of Al356-SiC MMCs from 3D and 2D axisymmetric single-particle FEA models with different particle aspect ratios to draw comparison with experimental, and two numerical estimations: the rules of mixture and Haplin-Tsai model. When compared with

experimental results, discrepancies were noticed for high aspect ratios, with the 3D models being more accurate than the 2D axisymmetric ones. Barbera, et al. [77] studied the relationships between thermal and mechanical loading history, and creep dwell period on the creep-fatigue interaction of SiC fiber reinforced 2024T3 aluminum matrix composites. Sharma, et al. [78] proposed the use of Gurson-Tvergaard-Needleman (GTN) model to study the influence of void on residual stresses generated during sintering of Al-Al_2O_3 particulate composites. Thermomechanical properties in presence of the residual stresses were studied. Kwok, et al. [79] studied the effective steady-state creep response of porous metals by numerical homogenization based on 3D finite element models of reconstructed from tomographic images, and analytical methods.

Conventional homogenization models have been primarily developed for uniform composites, and are unable to capture the effects of material gradient. Yin, et al. [80] proposed a multiscale modeling technique using graded volume element to derive the thermal conductivity in two -phase graded composites. Muliana [81] showed the dependence of material properties on whether constituent 1 or constituent 2 is modeled the inclusion. Figure 2.4 illustrates a graph obtained in their study, highlighting differences in elastic moduli as a result of interchanging the inclusion and matrix materials. The discrepancies were attributed to a large mismatch between the constituent material properties. Thus, it is important to model the microstructural features more realistically. The differences arising due to whether a material is attributed to inclusions or the matrix were consolidated by dividing the FGM into 3 regions: one containing spherical SiC in C matrix, the transition zone, and the third containing C inclusions in SiC matrix. While the effective properties of regions 1 and 3 were determined directly from the micromechanical models, the properties at the transition zone were assumed to vary linearly between the two bounds. Elastic

moduli, coefficient of thermal expansion and thermal conductivity for volume fractions for 0 to 1 were obtained, showing good comparison experimental data and analytical solutions available in the literature. Relaxation moduli of a polymer-composite were also determined. A micromechanical framework was proposed to analyze time-dependent thermo-mechanical response of an FGM.

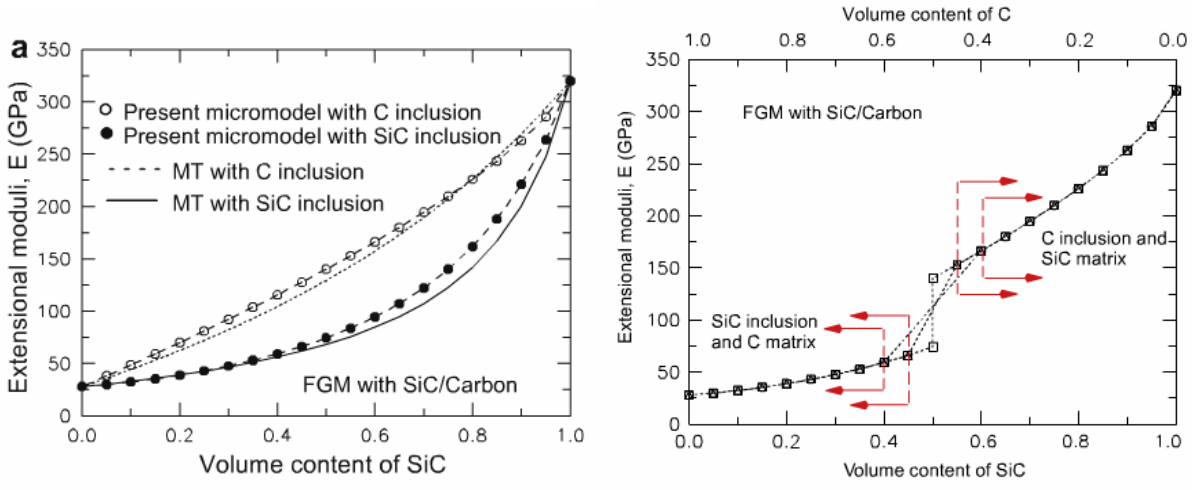

a) b)

Figure 2.4: Effective elastic moduli for a range of volume fraction [81]

An important aspect in perspective of applications is the choice of the micromodel. Numerous studies in the literature attempt to predict the behavior of MMCs. In particular, single inclusions assumptions have been widely implemented due to its simplicity. On the other hand, large multiparticle models have been developed to include interaction between inclusions. This study uses three different micromechanical models: i) 2D axisymmetric single-particle, ii) 3D single-particle, and iii) 3D multi-particle RVE to predict local creep properties of an FGM.

2.2.3 Boundary conditions used in representative volume elements

Apparent properties of RVEs are highly influenced by two factors: the RVE size, and the choice of boundary conditions. The RVE size handles the number of microstructural factors that can be contained within the model. Different kinds of boundary conditions used in the literature are: i) static uniform boundary condition (SUBC), ii) kinematic uniform boundary condition (KBC), iii) orthogonal mixed boundary condition (OMBC), and iv) periodic boundary condition (PBC). As a composite is represented as a repeating array of RVE, the deformed boundaries should not allow separation or overlap between adjacent RVEs. OMBC and PBC ensures geometric compatibility with surrounding cells. OMBC ensures that the deformed shape remains cylindrical (for axisymmetric 2D model) or orthorhombic with planar walls (for 3D model), not allowing gap between neighboring cells. The periodic boundary conditions require meshes on the opposite boundary surfaces (with normal along x_j axis) in the model must be identical, and the displacement components u_i are coupled by:

$$u_i^{K^+} - u_i^{K^-} = \bar{S}_{ij}\left(x_j^{K^+} - x_j^{K^-}\right), \tag{2.1}$$

where $\bar{S}_{ij}$ is the average strain, and K^+ and K^- represents surfaces on the +ve and –ve x_j directions respectively. Three faces along the coordinate directions are first meshed with planar elements and then copied on the opposite surfaces. The entire volume is meshed with 3D elements, resulting in identical meshes on opposite boundaries. Constraint equations are used to correlate displacement components of nodal pairs having identical in-plane coordinates on opposite surfaces.

Apparent properties evaluated from the KUBC and SUBC models are considered as the upper and lower bounds for the effective properties, with that from the OMBC and PBC lying between them. The OMBC has been applied to determine the creep response of the micromechanical models in the present work. With increasing RVE size, the two bounds become

identical, and the apparent properties are said to converge to the effective value. For practical purposes, it is important to determine the minimum RVE size in order to obtain an acceptable estimation of effective properties.

A representative volume element is assumed to be repeatable over the entire domain. Its size is chosen to be very small compared to the macroscopic body but much larger compared to atomic scales for continuum mechanics to be applicable. Average stress and strains in the RVE are calculated by integrating the corresponding quantities over the RVE domain and dividing by its volume:

$$\bar{\sigma}_{ij} = \frac{1}{V}\sum_{\beta=1}^{N}\int_{V^{(\beta)}} \sigma_{ij}^{(\beta)}\left(x_k^{(\beta)}\right) dV^{(\beta)} = \frac{1}{V}\sum_{\beta=1}^{N} V^{(\beta)}\,\sigma_{ij}^{(\beta)} \tag{2.2}$$

$$\bar{\epsilon}_{ij} = \frac{1}{V}\sum_{\beta=1}^{N}\int_{V^{(\beta)}} \epsilon_{ij}^{(\beta)}\left(x_k^{(\beta)}\right) dV^{(\beta)} = \frac{1}{V}\sum_{\beta=1}^{N} V^{(\beta)}\,\epsilon_{ij}^{(\beta)}. \tag{2.3}$$

Subscript (β) is the element number and V is the total number of elements in the RVE. $\sigma_{ij}^{(\beta)}$ and $\epsilon_{ij}^{(\beta)}$ are the average stress and strain respectively within element (β). This type of averaging allows the heterogeneous composite to be represented by a globally homogeneous one with approximately equal strain energy.

Huet [82] considered the four kinds of BCs and concluded that apparent properties obtained from KUBC and SUBC give the upper and lower bounds for effective properties, and OMBC and PBC give better overall response than that from imposed force or displacement BCs. Cho, et al. [83] compared the application of two different boundary conditions (BC): SUBC and OMBC on 2D RVEs. Elastic strain fields on the inner portion of the RVE were identical, but differences were noticed at boundaries, mainly near the particle-matrix interfaces. Thickness of the BC-affected region remained identical for all RVE sizes for a given BC, and the apparent elastic moduli became

independent of the applied boundary condition with the increase in RVE size. An RVE may not exists if the BC-affected thickness increases with increasing RVE length, and the apparent property will diverge away from the effective value. BC-affected thicknesses are generally larger with greater heterogeneity (higher particle percentage) or non-linearity (plasticity etc.) within the model. Larger RVE sizes should be considered for such cases.

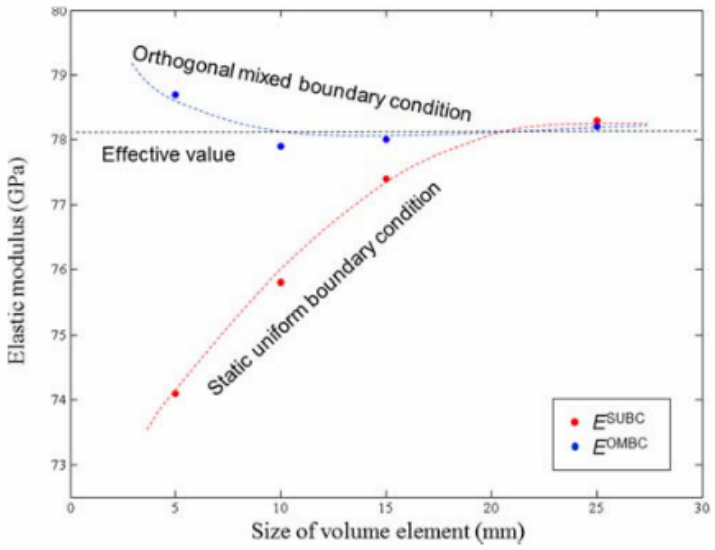

Figure 2.5: Apparent elastic moduli obtained for different boundary conditions [83]

The study was extended by Cho et al. [84] to incorporate plasticity, and creep into the model. Again, BC-affected thicknesses were found to be independent of RVE sizes for the same particle content, but larger than that in linear elastic models. The BC-affected thickness gradually increased with increasing volume fraction up to a critical value, and became stable for the elastic and creep models. However, in the plasticity model, the thickness increased continuously, and the strain fields of the whole RVEs became sensitive to the type of BC applied for high reinforcement contents.

2.2.4 Prediction of creep properties of metal matrix composites

FGMs have great potential in high temperature components used in automotive, aerospace applications etc. Advanced classes of composite materials such as metal-matrix and ceramic-matrix composites demonstrate suitable manufacturability for graded structures. SiC reinforced aluminum composites have been widely considered especially in the aerospace industry due to its low cost, mass production, formability using conventional processes, superior mechanical properties and retention at high temperatures compared to aluminum alloys. Al-SiC composites are also frequently considered in the potential high-temperature applications of FG thick-walled cylinders, and discs. The composite exhibits creep behavior at elevated temperatures. At elevated temperatures, these composites undergo time-dependent deformations through creep mechanism, requiring material scientist and engineers to have thorough understanding of creep behaviors at the micro and macro levels. As the FGM technology opens the possibility of endless material compositions and grading profiles, experimental approaches become quite expensive and time consuming. Experimental investigations of creep behavior at high temperatures being time consuming and costly, a need for numerical techniques arises in order to efficiently predict creep behavior as a function of the constituent properties and features. Thus, computational models become useful in predicting time-dependent deformations of FG composites.

Creep constitutive equations are non-linear, and solutions of arising differential equations become extremely complicated. Mondali, et al. [85] developed an analytical model based on shear-lag theory to predict steady state creep deformation of short fiber composites. Perfect fiber-matrix interfaces were assumed. While analytical and FEM results were close, they were significantly differently from experimental results. Ghavami, et al. [86] used a finite difference approach to predict steady state creep rates of short SiC fiber reinforced Al6016 composite considering

interfacial debonding. TEM studies have shown voids and interfacial debonding at fiber-matrix interfaces even at low strains. Governing equations were developed for a single fiber using an axisymmetric unit cell model, linearized and solved using a finite difference method. Results were in good agreement with that using FEM. Monfared, et al. [87] developed three analytical methods using approximation of creep constitutive equations (ACCE), difference of the stress exponents (DSC) and boundary value approaches (BVA) to present steady-state creep solutions in short-fiber reinforced MMCs. Perfect fiber-matrix interface was assumed.

FEM becomes very useful because it eliminates restrictions of geometry, material properties, number of phases etc. It is capable of evaluating full field solution for time-dependent problems. Park and Holmes [88] performed two and three dimensional finite element modeling of tensile creep and creep recovery behavior of SiC fiber reinforced Si_3N_4 ceramic matrix composites by considering elastic and creep properties of each constituents, fiber-reinforcement bonding and residual stresses resulting from hot-pressing. SiC fibers have a higher coefficient of thermal expansion than the Si_3N_4 matrix. Upon cooling from high processing temperatures, radial tension develops normal to the interface due to the CTE mismatch, causing partial or complete debonding of the fiber-matrix interface. Two limiting cases: i) perfectly bonded, and ii) completely debonded interfaces were considered. It was assumed that the matrix was free from voids or micro-cracking, and no sliding occurred between the fiber and matrix. Complete load transfer was assumed and the interfacial shear was zero. Both 2D and 3D models predicted similar creep rates, however the 3D model revealed that processing related tensile radial stresses near to the fiber-matrix interface decreased the during initial creep stage. Although total creep strain was larger for the debonded case, steady state creep rates were similar for perfectly bonded and debonded interface due to fast

relaxation of matrix stress approaching nearly the same limiting value. Half of the accumulated creep strain was recovered on unloading.

The 2D axisymmetric model imposes infinite number of neighboring whiskers along the transverse and circumferential directions, thus over estimating the strengthening effect. The distances between surrounding whiskers is also an averaged one, which is different than in the case of 3D unit-cells. A single-inclusion unit cell assumes regular, periodic array of embedded particles. Such models do not include the influence of local stress concentrations due to spatial distribution of inclusions in the microstructure and assume that all reinforcements deform simultaneously. As creep deformations are highly sensitive to stress levels, the spatial distributions have a large influence on the overall creep response, although the effect of may be small for effective physical properties. 3D morphologies with random multi-inclusions are expected to give more accurate predictions than the single-inclusion models.

Most models developed to predict the creep behavior of MMCs used the single inclusion unit-cell model, while the RSA algorithm motivated a research group to model multi-particle RVEs. Lee, et al. [89] predicted steady-state creep behavior of discontinuous silicon carbide whisker reinforced aluminum 6061 composite. Unidirectional and periodic composites were generated using a modified RSA algorithm. Localized stress concentrations due to particle interactions played an important role in the creep behavior and showed differences with those from commonly used single inclusion 2D and 3D models. Steady-state creep rates were close to experimental data.

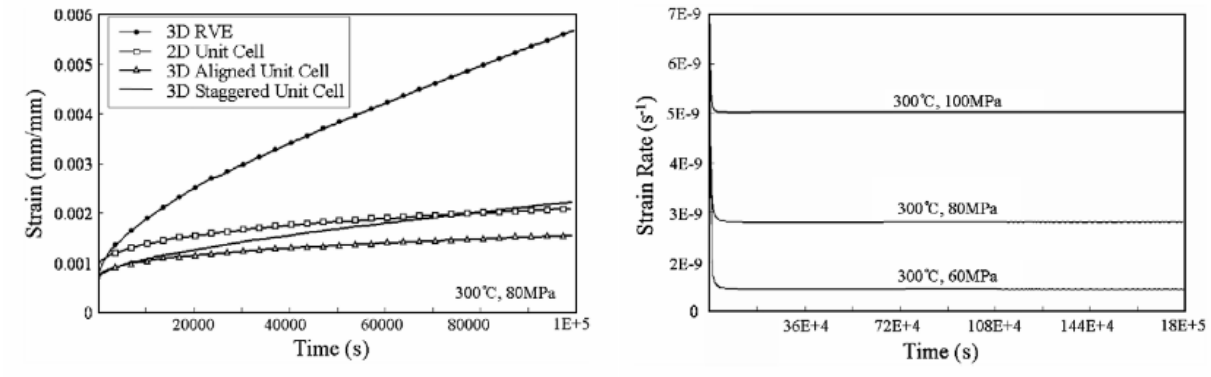

a) b)

Figure 2.6: a) Creep strain curves predicted using different RVE models, b) Variations of creep strain rate with time for 2D axisymmetric model

It was found that with creep deformations, equivalent stress in the matrix decreased and reached a steady-state condition. The creep strain-rate also decreased and became constant with time. Creep curves from single-inclusion 2D axisymmetric, single inclusion 3D, 3D staggered, and multi-inclusion 3D RVEs demonstrated differences due to inherent assumptions. Overall creep strain and strain-rates were found to be considerably higher for multi-inclusion 3D RVEs compared to the other models. The aim of the study was to demonstrate a numerical approach to predict creep behaviors of MMCs. Some differences between numerical and experimental results were acknowledged possibly due to the lack of mesoscale heterogeneities such as clustering of inclusions, as arrangement has is seen to influence other material behaviors of MMCs.

MMCs are found to exhibit ‘anomalously high’ stress exponents (stress dependence of steady-state creep rate) compared to the parent matrix. MMCs manufactured using powder metallurgy are typically homogeneous, but in cases of ingot metallurgy, clustering occurs due to settling and rejection of the reinforcement by the formation of matrix dendrites during solidification. Clustered inclusions act as stress concentrators and affect the creep response and other material properties. Lee, et al. [90] studied the effect of reinforcement clustering on the

steady-state creep response of SiC whisker reinforced Al using FEM. Numerical results from a homogenous model (a random and uniform whisker distribution generated using the RSA algorithm) was compared with that from a clustered model (a 2D hierarchical multiscale model generated using image analysis of micrographs) to indicate clustering as a possible origin of the high stress exponent values. The cluster model consisted of a whisker-free area and whisker-rich zones with local volume fractions higher than the average. A homogeneous micromechanical FE model was first used to determine the elastic and creep properties of the local regions. The properties represented the whisker-rich zones and were implemented at the global scale, allowing the local heterogeneity to be ignored. The clustered model revealed high local stresses in the whisker rich zone which represented areas with closely located whiskers, affecting the overall creep response. Figure 2.7 shows that the clustered model compares better with experimental results than the homogenous one, indicating clustering as an important factor in the creep behavior of MMCs. A limitation of the image based hierarchical technique is that it requires the analysis real micrographs, and cannot be implemented for microstructures where experimental images are unavailable. Interfacial debonding could be an additional factor for the explanation of high creep stress exponent. The effectiveness of using multi-inclusion RVEs in predicating creep behavior of MMCs was expanded by Lee, et al. [91]. A modified time-hardening creep model incorporating primary and secondary creep is used to analyze the sensitivity of RVE size on creep curves. RVEs with spherical inclusions were generated using the modified RSA algorithm.

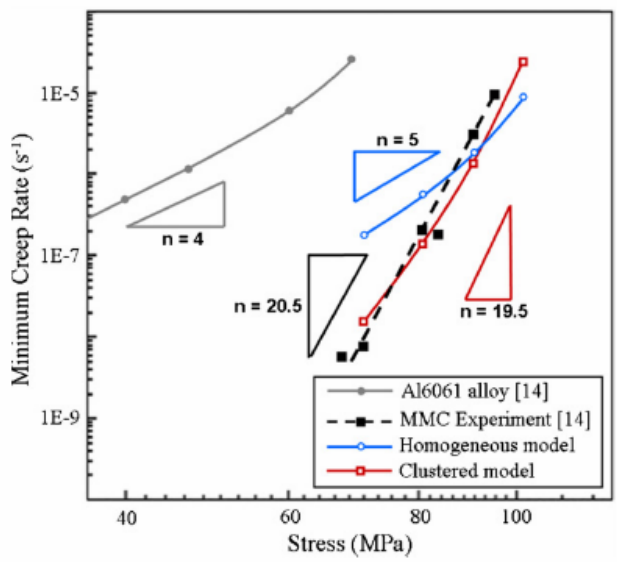

Figure 2.7: Logarithmic plot of steady-state creep rates vs. stress for homogeneous and clustered models of SiC_w-Al MMCs compared with experimental creep tests

Figure 2.8 illustrates that with increasing RVE size, statistical variations of creep curves reduce as a result of improved homogeneity and isotropy. An RVE is said to exist as the creep curve converges with increasing RVE length or number of realizations. Numerical predictions were compared with experimental data for 20% TiC reinforced Al-1.5Mg and 15% TiC reinforced pure Al MMCs [92]. Numerical predictions demonstrated reasonable agreement for the first case, and overestimated the creep response for the latter. The discrepancy was attributed to larger grain size of Al in the pure matrix than that in the composites, altering the major creep mechanism. Overall creep rates of non-creeping inclusion reinforced composites are significantly smaller than those of unreinforced alloys. The model is applicable to cases where the microstructure and creep mechanism of the matrix in the composite is similar to that of the unreinforced alloy under the same conditions.

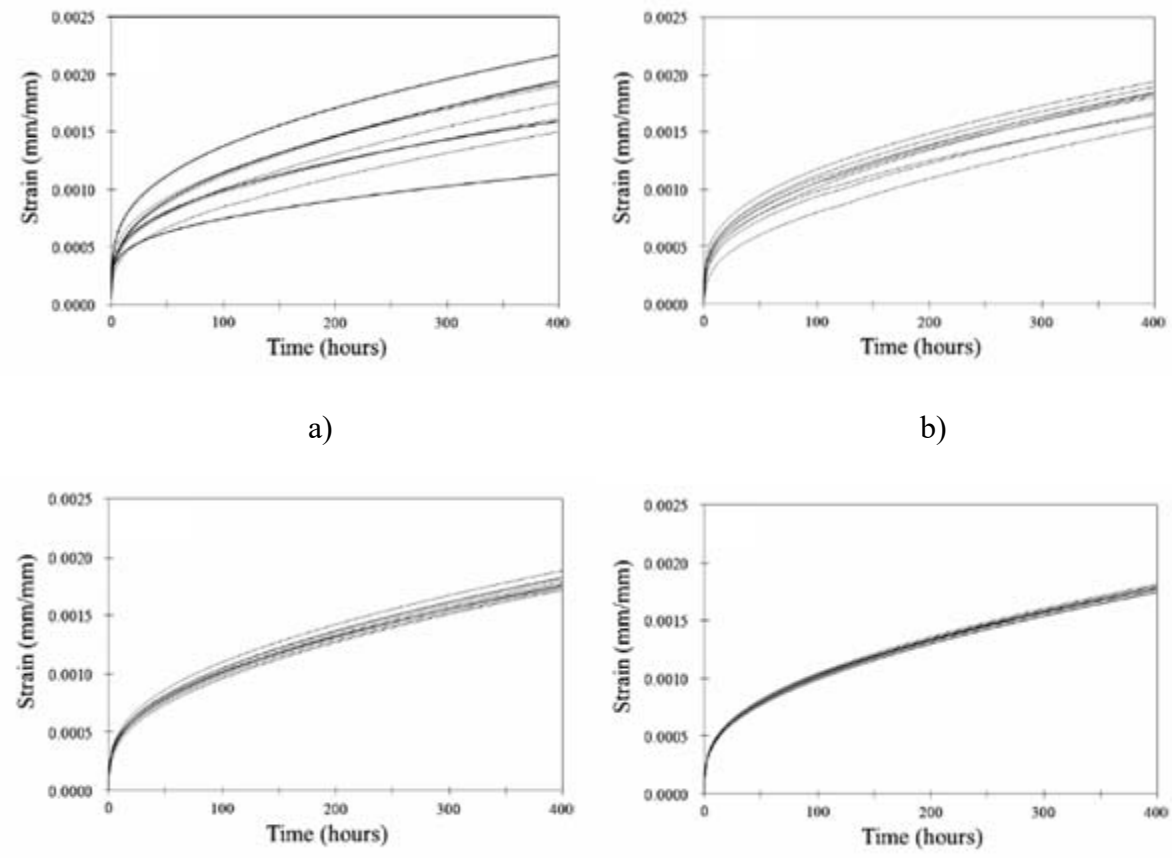

Figure 2.8: Creep curves predicted using different RVE sizes: a) $L = 5$ μm, b) $L = 10$ μm, c) $L = 15$ μm, and d) $L = 20$ μm

Yu, et al. [93] incorporated the creep mechanisms (diffusional creep and grain boundary sliding) in finite element micromodels to study the creep deformation of zirconium diboride-silicon carbide composites.

2.2.5 Matrix Creep models

Creep deformation in MMCs has been an active research topic because of the composite's potential application in high-temperature environments. It depends mainly of time, stress, and temperature. For composites with multiple phases, it is also a function of the material composition. Numerical prediction of creep of SiC reinforced aluminum composites have been studied by some

authors. An important aspect of creep damage analysis is the constitutive model. Table 2.2 lists the creep models used in the studies used in conjunction with the finite element method, where ϵ_{cr} and $\dot{\epsilon}_{cr}$ are creep strain and strain-rates respectively at time t, and σ denotes the effective stress.

Table 2.2: Creep models of aluminum found in literature

Reference	Material	Creep model	Equation
Mondali et al. (2005)	Al6061 (300°C)	Exponential	$\log \dot{\epsilon}_{cr} = -10.7 + 0.0671 \log \sigma$
Lee et al. (2010)	Al6010 (300°C)	Exponential	$\dot{\epsilon}_{cr} = 1.87\times10^{-11} e^{\frac{\sigma}{6.47}}$
Lee et al. (2011)	Al6016 (288°C)	Exponential and Norton's	$\dot{\epsilon}_{cr} = \begin{cases} 4.2\times10^{-9} e^{\left(\frac{\sigma}{8.5}\right)}, \sigma \geq 45 \text{ MPa} \\ 2\times10^{-13}\sigma^{4.0}, \sigma < 45 \text{ MPa} \end{cases}$
Lee et al. (2014)	Al-1.5Mg	Combined time-hardening	$\epsilon_{cr} = 4.6\times10^{-7}\sigma^{0.5}t^{0.45} + 1\times10^{-22}\sigma^{7.6}t$
Lee et al. (2014)	Pure Al	Time-hardening	$\epsilon_{cr} = 1.5\times10^{-38}\sigma^{20.8}t$

Most commercial finite element packages have the capability of modeling creep. The Norton's law (steady state) is commonly used for its simplicity. The combined time-hardening model [8] is able to model both primary and secondary creep; the creep strain ϵ_{cr} at time t and uniaxial stress σ is given by:

$$\epsilon_{cr} = A\sigma^n t^q + B\sigma^m t, \tag{2.4}$$

where A and B are coefficients and m, n and q are creep exponents. The two terms in the equation represent the primary and secondary creep stages respectively. A Newton-Raphson iterative method is used to compute the creep strain increment at each time step. The equation is implemented using an explicit Euler forward algorithm. The modified total strain is calculated as:

$$\{\epsilon'_n\} = \{\epsilon_n\} - \{\epsilon_n^{pl}\} - \{\epsilon_n^{th}\} - \{\epsilon_{n-1}^{cr}\}, \tag{2.5}$$

where n denotes the time point, and the superscripts pl, th, and cr refer to plastic, thermal, and creep components respectively.

The equivalent modified total strain and equivalent stress are computed by:

$$\epsilon_{et} = \frac{1}{\sqrt{2}(1+\nu)} \begin{bmatrix} (\epsilon'_x - \epsilon'_y)^2 + (\epsilon'_y - \epsilon'_z)^2 + (\epsilon'_z - \epsilon'_x)^2 \\ + \frac{3}{2}(\gamma'_{xy})^2 + \frac{3}{2}(\gamma'_{yz})^2 + \frac{3}{2}(\gamma'_{zx})^2 \end{bmatrix}^{\frac{1}{2}}, \tag{2.6}$$

$$\sigma_e = E\ \epsilon_{et}, \tag{2.7}$$

where E is the Young's modulus and ν is the Poisson's ratio.

The creep ratio is defined as:

$$C_S = \frac{\Delta\epsilon^{cr}}{\epsilon_{et}}, \tag{2.8}$$

where $\Delta\epsilon^{cr}$ is the equivalent strain increment.

The strain increment components in the 2D formulation are:

$$\Delta\epsilon_x^{cr} = \frac{\Delta\epsilon^{cr}}{\epsilon_{et}} \frac{2\epsilon'_x - \epsilon'_y - \epsilon'_z}{2(1+\nu)} \tag{2.9}$$

$$\Delta\epsilon_y^{cr} = \frac{\Delta\epsilon^{cr}}{\epsilon_{et}} \frac{2\epsilon'_y - \epsilon'_z - \epsilon'_x}{2(1+\nu)} \tag{2.10}$$

$$\Delta\epsilon_z^{cr} = -\Delta\epsilon_x^{cr} - \Delta\epsilon_y^{cr} \tag{2.11}$$

$$\Delta\epsilon_{xy}^{cr} = \frac{\Delta\epsilon^{cr}}{\epsilon_{et}} \frac{3}{2(1+\nu)} \gamma'_{xy}, \tag{2.12}$$

with two additional components in 3D:

$$\Delta\epsilon_{yz}^{cr} = \frac{\Delta\epsilon^{cr}}{\epsilon_{et}} \frac{3}{2(1+\nu)} \gamma'_{yz} \tag{2.13}$$

$$\Delta\epsilon_{xz}^{cr} = \frac{\Delta\epsilon^{cr}}{\epsilon_{et}} \frac{3}{2(1+\nu)} \gamma'_{xz}. \tag{2.14}$$

The elastic and total creep strain components are then calculated by:

$$(\epsilon_x^{el})_n = (\epsilon_x')_n - \Delta\epsilon_x^{cr} \tag{2.15}$$

$$(\epsilon_x^{cr})_n = (\epsilon_x^{cr})_{n-1} + \Delta\epsilon_x^{cr}. \tag{2.16}$$

2.2.6 Inclusion-matrix interface

An important aspect of reinforced composites is the effective transfer of load from the matrix to the inclusions. MMCs consist of a relatively low temperature matrix reinforced with a more refractory phase. This substantially increases the temperature capability than the matrix alone. The inclusion-matrix interface possesses different materials properties than original constituents. An interphase forms due to irreversible chemical reaction during manufacturing, and affects the stress transfer between the matrix and reinforcements. The volume and mechanical properties of interphases play an important part in determining the overall properties of the composite. Constitutive behavior of the interface can be implemented using finite element analysis with special interface elements. Progressive matrix-reinforcement debonding results in softening behavior of the composite. The quality of reinforcement-matrix bond can affect a wide range of mechanical properties. Detailed studies are necessary to expand the development of MMCs and application to FGMs.

From a theoretical and computational mechanics point of view, the interface can be classified into two categories: i) interface with perfect bonding, and ii) interface with imperfect bonding. In the case of perfect bonding, the interfacial region is considered to have infinite stiffness, and complete load transfer takes place between the reinforcements and matrix. The average elastic properties, strengths etc. can be obtained by rules-of-mixture based on iso-stress and iso-strain conditions. The models are functions of inclusion and matrix stiffness and volume fractions. In reality, perfect conditions do not hold and interface stiffness are always finite resulting in overestimation of material properties by the ROM models. Complete load transfer does not

occur between the inclusions and matrix, as a portion of the external load is absorbed by the interface undergoing finite deformation. It is necessary to capture the interface behavior to be able to accurately predict the creep properties. Crack propagation at interfaces can be analyzed using fracture mechanics techniques such as linear elastic fracture mechanics (LEFM), J-integral method, virtual crack extension (VCE), virtual crack closure (VCC) etc. These methods require an initial crack and the crack propagation path to be predefined. Other techniques adopt softening relationships between tractions and displacements, and introducing the energy required to separate interfacial surfaces, known as critical fracture energy. This is known as the cohesive zone model, and can solve fracture mechanics problems using continuum mechanics, as the displacement field remains continuously differentiable across the interface. The CZM the interfaces are represented by separate surface with zero thickness, and the model characterizes a constitutive relation between the traction vector T acting along the interface and the corresponding interfacial separation δ. CZM is usually represented by a traction-displacement $(T-\delta)$ curve. Physically, as the surfaces separate, the traction initially increases to reach a maximum value and then approaches zero with further separation. The areas under the normal traction-separation and shear traction separation graphs represent the critical fracture energies for normal and shear separations respectively. Various types of $T-\delta$ functions used are: i) exponential, ii) polynomial, iii) multilinear, iv) trigonometric etc.

Studies related to stress transfer have been discussed here capture the role of interface/interphases. Ghosh, et al. [94] modeled the interfacial debonding of fiber interfaces of fiber reinforced composites by implementing cohesive some models in Voronoi cell finite element model (VCFEM). Tvergaard [95] used cohesive zone model to analyze the fiber-matrix debonding of Al-SiC unit cells. Benabou, et al. [96] computed the overall elastic properties of two-phase

composites using finite element analysis. The interface was modeled as an elastic medium with normal and tangential stiffnesses. Mondal, et al. [97] modeled single-inclusion FE models of MMCs to investigate elastoplastic behaviors as functions of interface stiffness and thickness, and reinforcement volume fraction. The effective material properties were significantly reduced for interface stiffness less than 25% of the matrix stiffness. Romanowicz [98] determined stress-strain curves for glass-epoxy laminates using computational micromechanics. A unit cell consisting of fiber, matrix, and interphase under transverse tension was simulated using FEA, in which interface debonding was modeled using a bi-linear cohesive zone model (CZM). The CZM parameters were found to influence the macroscopic behavior of the composite. Reinforcement-matrix interface also plays an important role in macroscopic mechanical properties of MMCs. Kulkarni, et al. [99] used a multiscale approach employing finite element method to evaluate the effective elastic properties of carbon nanotube fiber reinforced polymeric composites by considering imperfect interfaces. Yuan, et al. [100] analyzed the influence of interfacial stiffness, fracture toughness, reinforcement volume fractions and reinforcement aspect ratio on the macro stress-strain curve for a single SiC particle reinforced Al-6064 unit cell using cohesive zone model. Figure 2.9 illustrates that the interface micro-stress increased with the increase of interfacial stiffness, and flow stress increased with the increase of interfacial fracture toughness as a result of enhanced load transfer capacity of the interface. Wang et al. [101] simulated the damage initiation and propagation in unidirectional glass fiber reinforced epoxy composites by extended finite element method (XFEM). Aghdam and Morsali [102] studied the effects of coating, interaction layer, and stress relaxation due to matrix viscoplasticity on the thermal residual stress generated in SiC fiber reinforced titanium composites using a 3D finite element unit-cell model. Aghdam, et al. [103]

then extended the model to predict the effects of interface damage, fiber coating, and thermal residual stresses on the off-axis loading characteristics of the composite.

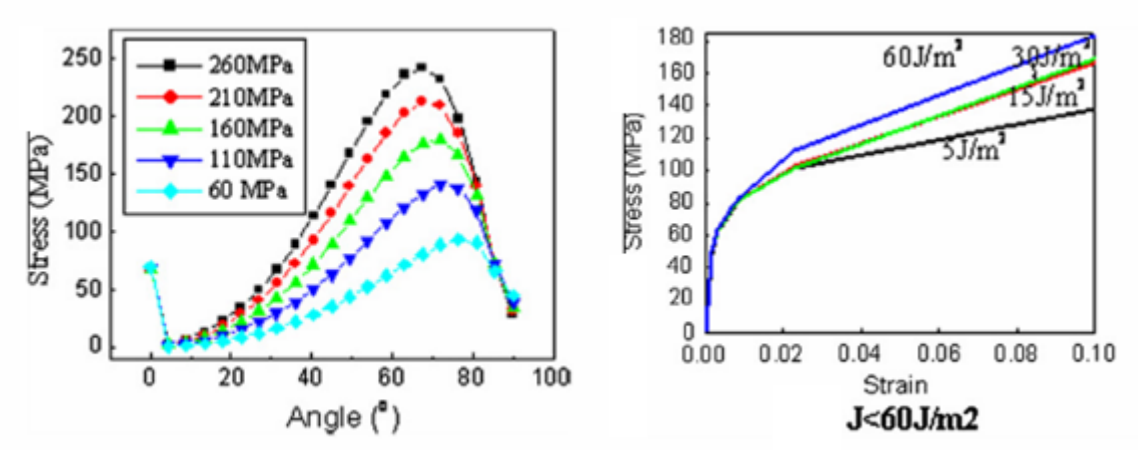

a) b)

Figure 2.9: a) Stress distribution along the interface for different interfacial Young's modulus, b) The effect of interfacial fracture toughness on overall stress-strain curve

A few articles aimed to study the effects of interfaces on material creep behavior. Goto and McLean [104] represented the effect of slipping interface by a thin layer of material (weaker than the matrix), separating the fiber and matrix. The model predicted that slipping at fiber/matrix interfaces had a dominant effect on the creep behavior of short fiber reinforced composites. Mondali, et al. [105] studied the effect of fiber-matrix debonding on the creep behavior of Al6061-SiC MMCs. Exponential law was assumed for creep behavior of the matrix. To reduce computational time and complexity, an axisymmetric single inclusion unit cell was used to represent regularly arranged cylindrical fibers in Al matrix. Imperfections in interfaces were introduced by debonding section of length of the interface itself, thereby controlling the effective length of the perfectly bonded region. This affected the load transfer capability between the matrix and fibers, along with the creep behavior of the composite. FEM model with exponential creep law showed better prediction of creep response than that using power law. Figure 2.10 shows the influence of interface delamination on the predicted steady-state creep rates of the composite.

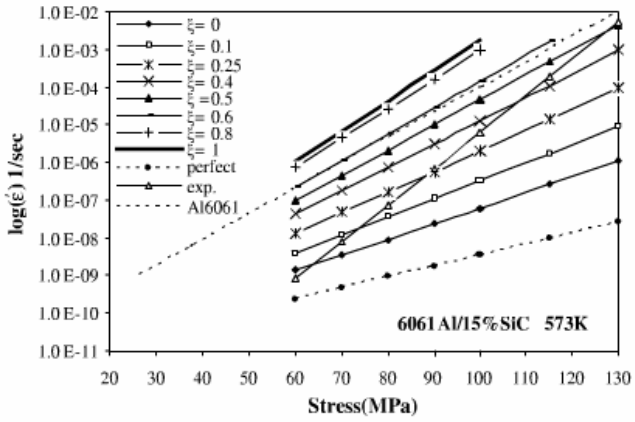

Figure 2.10: Steady-state creep rates for a range of interface damage [105]

Pan, et al. [106] studied the effect of interfacial sliding on the time-dependent creep, and stress relaxation behaviors of multi-walled carbon nanotube-polypropylene nanocomposites. The predicted creep compliance was found to be too stiff when imperfect load transfer condition was not used, but a weakened interface captured creep curves accurately.

2.3 Fabrication of functionally graded cylinders

Experimental advancement in functionally graded cylindrical structures is slow, and articles which are present are limited in scope. Sivakumar, et al. [107] processed and characterized a mullite/molybdenum FG hollow cylinder shown in Figure 2.11 using centrifugal molding technique.

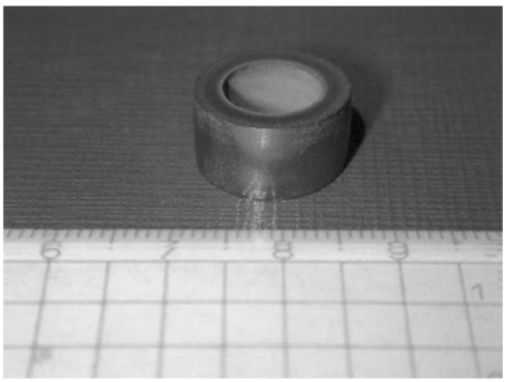

Figure 2.11: Mullite/Mo FG cylinder by centrifugal molding technique [107]

Rajan, et al. [108] fabricated a SiC particle reinforced 365 cast and 2121 wrought aluminum FG cylinders using liquid metal stir casting followed by horizontal centrifugal casting methods. Figure 2.12 shows the FG cylinder and the graded distribution of SiC particles along the wall thickness.

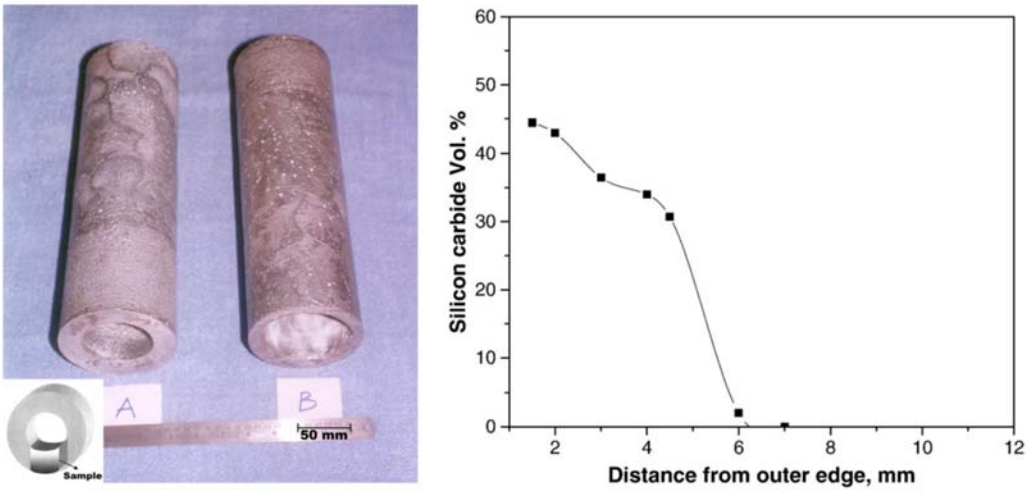

a) b)

Figure 2.12: a) SiC particle reinforced aluminum FG hollow-cylinder by horizontal centrifugal casting, b) SiC particle concentration from outer periphery of the cylinder

Lin et al. [109] fabricated FG Al-Si-Mg tubes using centrifugal casting method. Ulukoy, et al. [110] produced cylindrical SiC_p reinforced aluminum 2014 FGM samples using centrifugal casting to investigate fatigue crack behavior. Variation of Young's modulus along the wall thickness is presented in Figure 2.13.

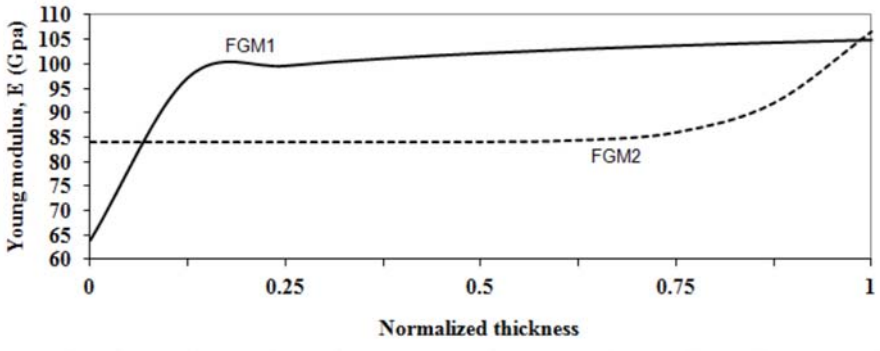

Figure 2.13: Variation of Young's modulus of cylindrical FGM samples [110]

Zygmuntowicz, et al. [111] fabricated nickel reinforced alumina ceramic hollow cylinders with three graded zones using centrifugal slip casting. To the authors' knowledge, experimental investigations have not been performed yet on FG pressure vessels.

2.4 Optimization of functionally graded materials

Farshi and Bidabadi [112] studied the weight minimization of inhomogeneous rotating discs under a high temperature gradient, while restricting equivalent creep stresses at all points within allowable limits. Nemat-Alla [113] investigated the composition optimization of 2D FGMs subjected to severe thermal loading cycle, by minimizing the maximum temperature or maximum equivalent stress. Strain hardening models was adopted to represent the elastic-plastic behavior of materials. Boussaa [114] studied a constrained optimization problem to determine the optimal composition profile of a thick-walled FG sphere subjected to high thermal gradient. Temperature dependent material properties were used in the formulation, and a gradient-based algorithm was used for optimization. Na and Kim [115] investigated the volume fraction optimization of FG panels to reduce stresses and improve thermal buckling using 3D finite element method. Temperature dependent material properties were used, and the volume fraction of constituents were varied in the thickness direction using the power-law distribution. The authors extended their work for step-formed plates by considering the structure to be composed of numerous homogeneous layers of different material properties [116]. Sadollah and Bahreininejad [117] implemented metaheuristic algorithms (genetic algorithm, and simulated annealing) to develop multi-objective optimization of FG dental implants. Kou, et al. [118] used particle swarm optimization technique to investigate the optimal design of FGMs, in which a feature tree based procedural method to represent generic material heterogeneities. Fereidoon, et al. [119] presented the application of particle swarm-based algorithms for volume fraction optimization of FGMs.

Chiba and Sugano [120] presented a method for material composition optimization for thermal stress relaxation of FGMs using a multiscale thermoelastic analysis (asymptotic expansion homogenization technique coupled with a finite element method) analysis and a genetic algorithm. Xu et al. [121] investigated the minimization of thermal residual stress in C/SiC FG coating, arising while cooling down from the processing temperature. An analytical model used to determine the residual stress was interfaced with particle swarm-based algorithms to determine an optimal design. Khanoki and Pasini [122] used multiscale mechanics and design optimization to minimize bone resorption and implant interface failure of graded cellular hip implants. Noh, et al. [123] proposed a reliability-based design optimization (RDBO) technique to optimize volume fraction profiles of FG composites considering uncertainty arising from manufacturing processes. Statistical information (mean, standard deviation, and distribution) were considered for homogenous layers, and a target reliability was set to maintain structural integrity of the composite. Silva and Loja. [124] considered the application of differential evolution algorithm to the optimization of residual stress distribution of sandwich panel composed of FGMs.

2.5 Research novelties

Portion of the present work is based on a problem statement considered by Nejad and Kashkoli [58] in which time-dependent creep solutions were sought. However, the numerical results tend to violate important boundary conditions as highlighted in Section 2.1.5, thereby deeming the solutions to be ineffective. Furthermore, the problem is extended to include effects of internal heat generation within the FGM. Another objective of the study is to introduce a more direct technique to characterize and incorporate FGM properties in analyzing the macroscopic behavior of pressure vessel structures.

The main features of this method are: i) integration of the lower scale by considering basic microstructural features (constituent material properties, volume fractions, and particle distribution), ii) comparison of simulation results from different micromechanical models, and iii) study of effects of exponents in power-function, and sigmoid-function material gradation. Based on finite element analysis, homogenization, and creep curve-fitting, the technique enables to vary material properties, constitutive behaviors, arrangements and interaction between phases to study the influence on the overall creep response of FG composites. The advantage of this model over other research works is the implementation of creep properties based on microstructure instead of fictitious profiles. As in any composite materials, the material properties and composition of constituents play and important role in its overall response. Recent developments in additive manufacturing technologies at the micro level enables possibilities of multiscale designs with complex architecture. With the development of new FGMs, there is an obvious demand of advanced numerical tools to correlate microstructural features to the macroscopic response. Further efforts can be made to advance to hierarchical multiscale models with many scales and architecture, starting from basic constituents at smaller levels.

CHAPTER 3: ANALYTICAL CREEP SOLUTIONS FOR FGM CYLINDER

The open literature contains numerous theoretical studies suggesting the development of *functionally graded* (FG) pressure vessels. An important part of the problem linking the gradation profile to the structural response. The purpose of this chapter is to recall basic equations and underlying assumptions to obtain closed-form solutions for thermoelastic stresses and strains, and time-dependent solutions for strain accumulated during creep of a FG hollow cylinder. Problem description

3.1 Problem description

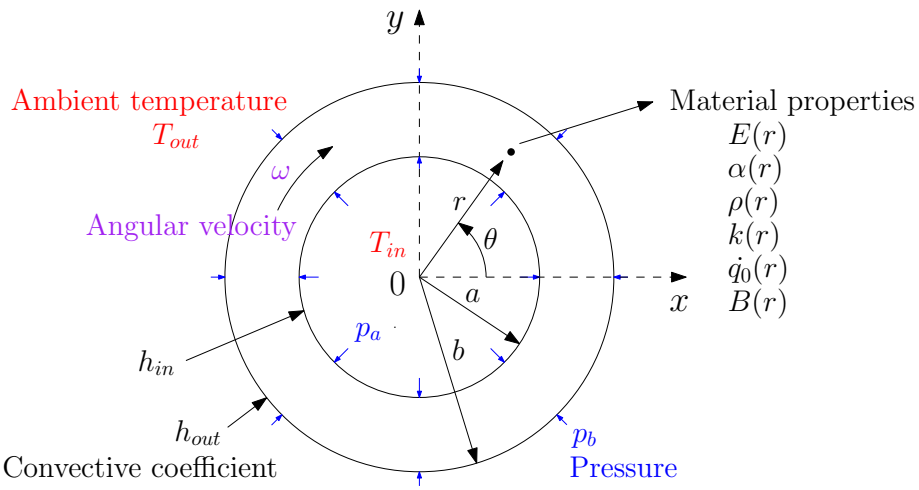

Figure 3.1: Illustration of the thermomechanical problem

A heat-generating hollow FG cylinder with inner and outer radii a and b respectively is considered. FG properties are described using the commonly used power law distributions. The cylinder is subjected to axisymmetric mechanical and thermal loadings: internal pressure p_a, external pressure p_b, and convective environment temperatures T_{in} and T_{out} at the inner and outer surfaces respectively, and angular velocity ω. The thermomechanical problem is illustrated in Figure 3.1. All cross-sections of the cylinder are in the same condition, and the problem becomes one-dimensional. There are two major objectives in this study: i) to derive closed-form expressions

for thermoelastic stresses and strains generated due to the combined loading, and ii) to establish functional relationships between creep strain rates and stresses, with subsequent implementation of a numerical procedure to obtain stress and strain histories.

3.2 Governing equations and solutions

3.2.1 Thermoelastic analysis

The thermoelastic problem is at first, decoupled, and the thermal portion solved to input the temperature solution into the mechanical problem. Based on the Fourier's law of heat conduction, the steady-state heat equation with internal heat source is:

$$\frac{1}{r}\frac{d}{dr}\left(r.k\frac{dT}{dr}\right)+\dot{q}=0, \tag{3.1}$$

where thermal conductivity, and internal heat generation rate are expressed using power law formulae:

$$k(r)=k_0\left(\frac{r}{a}\right)^{m_4} \tag{3.2}$$

$$\dot{q}(r)=\dot{q}_0\left(\frac{r}{a}\right)^{m_5}. \tag{3.3}$$

It is to be noted that there are no elastic terms in equation (3.1) (classical uncoupled thermoelasticity theory). Energy from hot fluid, and that generated within the cylinder are removed by an outer coolant, giving convective boundary conditions:

$$-k(a)\frac{dT}{dr}\Big|_{r=a}=h_{in}\big(T_{in}-T(a)\big) \tag{3.4}$$

$$-k(b)\frac{dT}{dr}\Big|_{r=b}=h_{out}(T(b)-T_{out}), \tag{3.5}$$

where h_{in} and h_{out} are convective heat transfer coefficients at the inner and outer surfaces respectively. T_{in} and T_{out} are the inner and outer ambient temperatures respectively.

The temperature field is obtained by solving equations (3.1)-(3.5) mentioned above,

$$T(r) = K_3 - K_2 r^{-m_4} - K_1 r^{2-m_4+m_5}, \tag{3.6}$$

where

$$\begin{aligned}
K_1 &= \frac{\dot{q}_0 a^{m_4-m_5}}{k_0(2+m_5)(2-m_4+m_5)} \\
K_2 &= -\frac{B_2 h_{in} + B_1 h_{out}}{A_2 h_{in} + A_1 h_{out}} \\
K_3 &= -\frac{A_2 B_1 - A_1 B_2}{A_2 h_{in} + A_1 h_{out}} \\
A_1 &= -a^{-1-m_4}(a h_{in} + k_0 m_4) \\
A_2 &= b^{-1-m_4}\left(b h_{out} - \left(\frac{b}{a}\right)^{m_4} k_0 m_4\right) \\
B_1 &= a^{1-m_4+m_5} k_0 K_1 (2 - m_4 + m_5) - h_{in}(a^{2-m_4+m_5} K_1 + T_{in}) \\
B_2 &= a^{-m_4} b^{1+m_5} k_0 K_1 (2 - m_4 + m_5) + h_{out}(b^{2-m_4+m_5} K_1 + T_{out}).
\end{aligned} \tag{3.7}$$

Prediction of stresses requires solving differential equations related to heat transfer, equilibrium, compatibility along with stress-strain and strain-displacement relations and appropriate boundary conditions.

For small-deformation, the strain-displacement relations are:

$$\epsilon_r = \frac{du_r}{dr} \tag{3.8}$$

$$\epsilon_\theta = \frac{u_r}{r}, \tag{3.9}$$

where u_r is the displacement in the radial direction. Stress equilibrium, and strain compatibility equations are:

$$\frac{d\sigma_r}{dr} + \frac{\sigma_r - \sigma_\theta}{r} = -\rho r \omega^2 \tag{3.10}$$

$$\frac{d\epsilon_\theta}{dr} + \frac{\epsilon_\theta - \epsilon_r}{r} = 0. \tag{3.11}$$

Relations between radial, tangential, and axial stress and strain components are given by:

$$\epsilon_r = \frac{1}{E}\{\sigma_r - \nu(\sigma_\theta + \sigma_z)\} + \alpha T \tag{3.12}$$

$$\epsilon_\theta = \frac{1}{E}\{\sigma_\theta - \nu(\sigma_z + \sigma_r)\} + \alpha T \tag{3.13}$$

$$\epsilon_z = \frac{1}{E}\{\sigma_z - \nu(\sigma_r + \sigma_\theta)\} + \alpha T, \tag{3.14}$$

where Young's modulus, coefficient of thermal expansion and density are assumed as:

$$E(r) = E_0 \left(\frac{r}{a}\right)^{m_1} \tag{3.15}$$

$$\alpha(r) = \alpha_0 \left(\frac{r}{a}\right)^{m_2} \tag{3.16}$$

$$\rho(r) = \rho_0 \left(\frac{r}{a}\right)^{m_3}. \tag{3.17}$$

Poisson's ratio ν has little effect on stress distributions, and can be assumed constant. For an infinite cylinder, the displacement is axial direction is prevented (plane strain condition), i.e.

$$\epsilon_z = 0. \tag{3.18}$$

The radial stress at the inner and outer surfaces must be equal to the compressive stress of internal and external pressures respectively, and the mechanical boundary conditions can be written as:

$$\sigma_r(a) = -p_a \tag{3.19}$$

$$\sigma_r(b) = -p_b. \tag{3.20}$$

By solving equations (3.6) - (3.20), radial and circumferential strains can be explicitly deduced as:

$$\epsilon_r = 2r^{1+\eta_3} d_3 + 2r^{1+\eta_4} d_4 + 2r^{1+\eta_5} d_5 + 2r^{1+\eta_6} d_6 + r^{-1+\eta_1} d_1 \eta_1 \tag{3.21}$$

$$\epsilon_\theta = r^{-1+\eta_1}d_1 + r^{-1+\eta_2}d_2 + r^{1+\eta_3}d_3 + r^{1+\eta_4}d_4 + r^{1+\eta_5}d_5 + r^{1+\eta_6}d_6$$
$$+r^{-1+\eta_2}d_2\eta_2 + r^{1+\eta_3}d_3\eta_3 + r^{1+\eta_4}d_4\eta_4 + r^{1+\eta_5}d_5\eta_5 + r^{1+\eta_6}d_6\eta_6, \quad (3.22)$$

where

$$C_1 = m_1 + 1$$

$$C_2 = \frac{\nu m_1}{1-\nu} - 1$$

$$C_3 = \frac{(1+\nu)(2+m_1+m_2-m_4+m_5)a^{-m_2}\alpha_0 K_1}{\nu - 1}$$

$$C_4 = \frac{(1+\nu)(m_1+m_2-m_4)a^{-m_2}\alpha_0 K_2}{\nu - 1}$$

$$C_5 = \frac{(1+\nu)(m_1+m_2)a^{-m_2}\alpha_0 K_3}{1-\nu}$$

$$C_6 = \frac{(2\nu-1)(\nu+1)a^{m_1-m_3}\rho_0\omega^2}{E_0(1-\nu)}$$

$$\eta_{1,2} = \frac{1}{2}\left(1 - C_1 \mp \sqrt{(C_1-1)^2 - 4C_2}\right) \quad (3.23)$$

$$\eta_3 = m_2 - m_4 + m_5 + 1$$

$$\eta_4 = m_2 - m_4 - 1$$

$$\eta_5 = m_2 - 1$$

$$\eta_6 = 1 - m_1 + m_3$$

$$d_3 = \frac{C_3}{(\eta_3+2)(\eta_3+C_1+1)+C_2}$$

$$d_4 = \frac{C_4}{(\eta_4+2)(\eta_4+C_1+1)+C_2}$$

$$d_5 = \frac{C_5}{(\eta_5+2)(\eta_5+C_1+1)+C_2}$$

$$d_5 = \frac{C_6}{(\eta_6+2)(\eta_6+C_1+1)+C_2}$$

$$\lambda_0 = \frac{\nu E_0}{(1+\nu)(1-2\nu)}$$

$$\mu_0 = \frac{E_0}{2(1+\nu)}$$

$$F_1 = a^{-1+\eta_1}(\lambda_0 + \eta_1(\lambda_0 + 2\mu_0))$$

$$G_1 = a^{-1+\eta_2}(\lambda_0 + \eta_2(\lambda_0 + 2\mu_0))$$

$$H_1 = p_a + a(3\lambda_0 + 4\mu_0)(a^{\eta_3}d_3 + a^{\eta_4}d_4 + a^{\eta_5}d_5 + a^{\eta_6}d_6)$$
$$+a(\lambda_0 + 2\mu_0)(a^{\eta_3}d_3\eta_3 + a^{\eta_4}d_4\eta_4 + a^{\eta_5}d_5\eta_5 + a^{\eta_6}d_6\eta_6)$$
$$+\alpha_0(3\lambda_0 + 2\mu_0)(a^{2-m_4+m_5}K_1 + a^{-m_4}K_2 - K_3)$$

$$F_2 = b^{-1+\eta_1}(\lambda_0 + \eta_1(\lambda_0 + 2\mu_0))$$

$$G_2 = b^{-1+\eta_2}(\lambda_0 + \eta_2(\lambda_0 + 2\mu_0))$$

$$H_2 = p_b a^{m_1} b^{-m_1} + b(3\lambda_0 + 4\mu_0)\begin{pmatrix} b^{\eta_3}d_3 + b^{\eta_4}d_4 + b^{\eta_5}d_5 \\ +b^{\eta_6}d_6 \end{pmatrix}$$
$$+ b(\lambda_0 + 2\mu_0)\begin{pmatrix} b^{\eta_3}d_3\eta_3 + b^{\eta_4}d_4\eta_4 + b^{\eta_5}d_5\eta_5 \\ +b^{\eta_6}d_6\eta_6 \end{pmatrix}$$
$$+ \left(\frac{b}{a}\right)^{m_2}\alpha_0(3\lambda_0 + 2\mu_0)\begin{pmatrix} b^{2-m_4+m_5}K_1 + b^{-m_4}K_2 \\ -K_3 \end{pmatrix}$$

$$d_1 = \frac{G_2H_1 - G_1H_2}{F_2G_1 - F_1G_2}$$

$$d_2 = \frac{F_1H_2 - F_2H_1}{F_2G_1 - F_1G_2}.$$

And the stresses are obtained using:

$$\sigma_r = \left(\frac{r}{a}\right)^{m_1}((\lambda_0 + 2\mu_0)\epsilon_r + \lambda_0\epsilon_\theta - (3\lambda_0 + 2\mu_0)\alpha T) \tag{3.24}$$

$$\sigma_\theta = \left(\frac{r}{a}\right)^{m_1}((\lambda_0 + 2\mu_0)\epsilon_\theta + \lambda_0\epsilon_r - (3\lambda_0 + 2\mu_0)\alpha T) \tag{3.25}$$

$$\sigma_z = \nu(\sigma_r + \sigma_\theta) - E\alpha T. \tag{3.26}$$

3.2.2 Time-dependent creep solutions

A functional relationship between creep strain rates and stresses is derived. Taking time derivatives, the strain-displacement relations from equations (3.8)-(3.9) become:

$$\dot{\epsilon}_r = \frac{d\dot{u}_r}{dr} \tag{3.27}$$

$$\dot{\epsilon}_\theta = \frac{\dot{u}_r}{r}. \tag{3.28}$$

Equilibrium and strain compatibility equations are expressed as:

$$\frac{d\dot{\sigma}_r}{dr} + \frac{\dot{\sigma}_r - \dot{\sigma}_\theta}{r} = 0 \tag{3.29}$$

$$\frac{d\dot{\epsilon}_\theta}{dr} + \frac{\dot{\epsilon}_\theta - \dot{\epsilon}_r}{r} = 0. \tag{3.30}$$

The Norton's creep constitutive model relates the effective strain rate $\dot{\epsilon_e}$ and effective stress σ_e as:

$$\dot{\epsilon_e} = B\sigma_e^n, \tag{3.31}$$

where B and n are material creep constants. The Norton's creep coefficient B is assumed to vary along the wall thickness according to:

$$B(r) = B_0 \left(\frac{r}{a}\right)^{m_6}, \tag{3.32}$$

and σ_e is given by:

$$\sigma_e = \frac{1}{\sqrt{2}} \sqrt{(\sigma_r - \sigma_\theta)^2 + (\sigma_\theta - \sigma_z)^2 + (\sigma_z - \sigma_r)^2}\,. \tag{3.33}$$

The exponent n in equation (3.31) is assumed to be constant to make the problem simpler.

The effective stress and effective strain rate facilitates the determination on strain rates under multiaxial states:

$$\dot{\epsilon}_r = \frac{1}{E}\{\dot{\sigma}_r - \nu(\dot{\sigma}_\theta + \dot{\sigma}_z)\} + \frac{3}{2}B\sigma_e^{n-1}\left(\sigma_r - \frac{1}{3}(\sigma_r + \sigma_\theta + \sigma_z)\right) \tag{3.34}$$

$$\dot{\epsilon}_\theta = \frac{1}{E}\{\dot{\sigma}_\theta - \nu(\dot{\sigma}_z + \dot{\sigma}_r)\} + \frac{3}{2}B\sigma_e^{n-1}\left(\sigma_\theta - \frac{1}{3}(\sigma_r + \sigma_\theta + \sigma_z)\right) \tag{3.35}$$

$$\dot{\epsilon}_z = \frac{1}{E}\{\dot{\sigma}_z - \nu(\dot{\sigma}_r + \dot{\sigma}_\theta)\} + \frac{3}{2}B\sigma_e^{n-1}\left(\sigma_z - \frac{1}{3}(\sigma_r + \sigma_\theta + \sigma_z)\right) = 0. \tag{3.36}$$

Equations (3.27) - (3.36) are reduced to form a differential equation of $\dot{\sigma}_r$ shown below:

$$\begin{aligned} &2r^2(-1+\nu^2)\sigma_e^2\frac{d^2\dot{\sigma}_r}{dr^2} - 2r(-3+m_1)(-1+\nu^2)\sigma_e^2\frac{d\dot{\sigma}_r}{dr} \\ &\quad - 2m_1(-1+\nu+2\nu^2)\sigma_e^2\dot{\sigma}_r + rE(r)\sigma_e^{1+n} \\ &\quad + rE(r)\sigma_e^{1+n}\big((1+\nu)\sigma_r + (1-2\nu)\sigma_z + (-2+\nu)\sigma_\theta\big)B'(r) \\ &\quad + E(r)B(r)\sigma_e^n\Big((-1+n)r\big((1+\nu)\sigma_r + (1-2\nu)\sigma_z \\ &\quad + (-2+\nu)\sigma_\theta\big)\sigma_e' \\ &\quad + \sigma_e\Big(3\sigma_r - 3\sigma_\theta \\ &\quad + r\big((1+\nu)\sigma_r' + (1-2\nu)\sigma_z' + (-2+\nu)\sigma_\theta'\big)\Big)\Big) = 0. \end{aligned} \tag{3.37}$$

As the cylinder is exposed to constant pressures, the inner and outer radial stress rates are:

$$\dot{\sigma}_r(a) = 0 \tag{3.38}$$

$$\dot{\sigma}_r(b) = 0. \tag{3.39}$$

$\sigma_r, \sigma_\theta, \sigma_z$ and σ_e in equation (3.37) are complicated, and there is no closed form solution for the above set of equations. Thus, equations (3.37)-(3.38) are solved numerically by approximating each of the quantities into interpolating functions of r in the form of $\sum_i a_i r^i$. Once the stress rates are evaluated, the stresses are calculated using an incremental approach:

$$\sigma_{ij}^{(k)}(r, t_k) = \sigma_{ij}^{(k-1)}(r, t_{k-1}) + \dot{\sigma_{ij}}^{(k)}(r, t_k)\Delta t^{(k)}, \tag{3.40}$$

where the total time after k timing steps t_k is equal to the sum of time increments $\Delta t^{(i)}$ at each step:

$$t_k = \sum_{i=0}^{k} \Delta t^{(i)}. \tag{3.41}$$

A step-by-step flow diagram is shown in Figure 3.2.

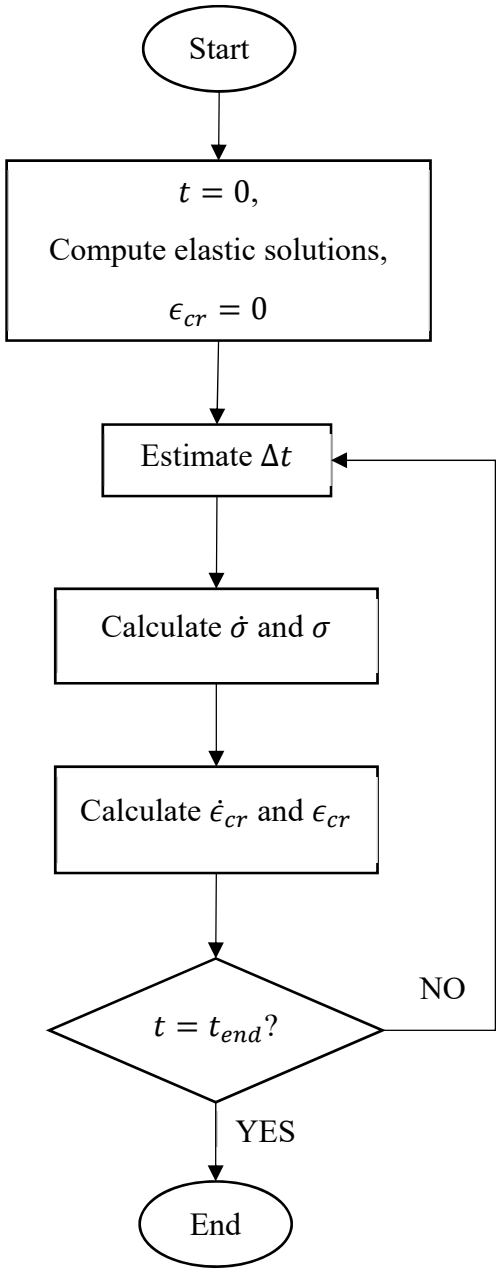

Figure 3.2: Flowchart for the computation of creep stress and strain histories

Initial creep strains are zero. Accumulated strains are calculated similarly using strain rates from equations (3.34)-(3.35) and time increments. Time steps need to be adjusted with time because creep strain rates are high during an early stage and decrease with the passage of time. In order to reduce computing time while ensuring accurate results, time step at each iteration is selected using the equation proposed by [125]:

$$\Delta t = \min_{j} \left[\frac{4(1+\nu)}{3nBE\sigma_e^{n-1}} \right], \tag{3.42}$$

where the smallest time calculated from *j* equally spaced points along the thickness is taken. Based on equations (3.40) - (3.42), a numerical procedure is implemented using Wolfram Mathematica 8.0 [126] which gives the stress and strain histories of the cylinder. The process is continued until the final time is reached.

CHAPTER 4: MULTISCALE CREEP ANALYSIS OF FGM CYLINDERS

The creep response of FG cylinders has been an area of interest to the solid mechanics community. The behavior of such structures depends on the underlying simplifications and assumptions. In the last decades, developments have been limited to ideal cases, but not linked to the study of multiscale models required to design high performance pressure vessels for extreme environments. The studies have been successful in representing the idealized macroscopic behavior but are not consistent with the microstructure of FGMs. To bridge the gap between the micro and macro levels a practical model for the creep behavior of FG cylindrical vessels has been developed. In this chapter, modeling steps and techniques of the proposed multiscale creep analysis of a FG thick-walled cylinder has been described.

4.1 Methodology

A multiscale approach based on the finite element method is developed to link the microscopic and macroscopic scales to predict the creep behavior of FG pressure vessels. The model is implemented sequentially: step 1 characterizes the FG composite by determining the homogenized creep behavior as a function of volume fraction. Finite element models of particle-reinforced composite samples are first constructed to compute their homogenized creep behavior. Creep parameters are estimated by curve-fitting the data obtained from the finite element study to a material model. Step 2 links the estimated parameters to an axisymmetric finite element model at the macroscale. Functional gradation is defined by assigning the volume fraction as a field-variable to each node. Homogenized material properties are interpolated at the integration points in the elastic and creep computations to determine the time-dependent response of a pressurized FG thick-walled cylinder. The step is computationally efficient because there is no need to model

detailed microstructure, or solve an entire RVE at each integration point. A schematic representation of the multiscale framework is illustrated in Figure 4.1.

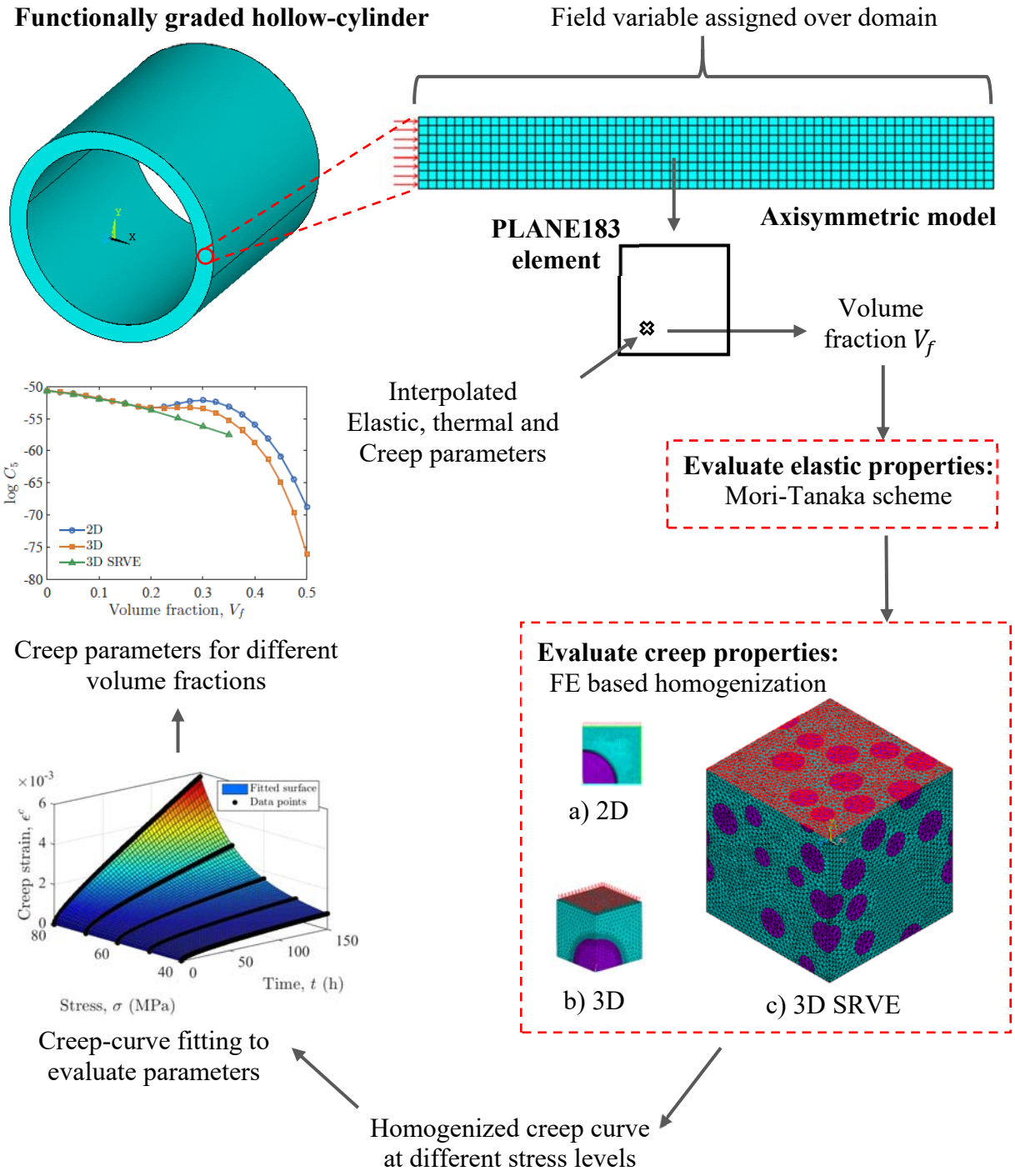

Figure 4.1: Schematic representation of the multiscale framework

4.2 Analysis at the microscale

Consider a FGM composed of two distinct constituents: metal and ceramic. As precise morphological information is not available, the effective properties of the composite can be determined based on properties of the constituents and the volume fraction. At the micro level, the structure is assumed to be composed of spherical ceramic particles of several microns in diameter dispersed within a metal matrix. To account for the functional gradation, the spacing between the particles is gradually changed from one surface to the other. A schematic micrograph of two-phase FGM composite is shown in Figure 4.2.

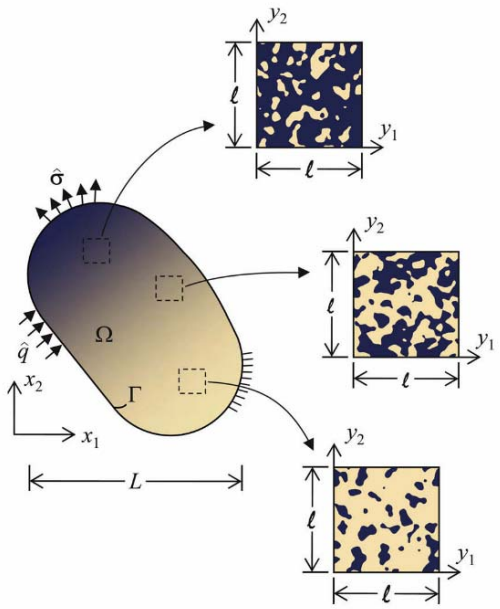

Figure 4.2: Schematic diagram of a two-phase FGMs [7]

Computation of creep properties at the microscale in terms of constituent volume fractions is the first step in understanding the macroscopic response. The method allows to generate ideal microstructures of either periodic (regularly arranged), or random materials accounting for particle interactions to be used for homogenization. Single or multi-particle unit-cells much smaller than the characteristic size of the macroscopic structure are generated and the effective elastic and creep

properties are obtained. Three different models have been used at the micro-level: i) 2D single-inclusion unit-cell, ii) 3D single-inclusion unit-cell, and iii) 3D SRVE. Each model employs FEM to compute creep properties for different local compositions to generate a material model. To automate the entire procedure, the models are prepared using scripts developed in MATLAB [127]. The volume fraction V_f of each single-inclusion model is related to the particle radius r and unit-cell length L using:

2D axisymmetric unit-cell:

$$V_f = \frac{2r^3}{3L^3} \tag{4.1}$$

3D single-particle unit-cell:

$$V_f = \frac{\pi r^3}{6L^3}. \tag{4.2}$$

For the 3D SRVE model, coordinates of centers, and radii of randomly arranged spheres required to meet a required volume fraction are first generated using modified RSA algorithm.

4.2.1 Modified-random sequential adsorption algorithm (RSA)

The modified RSA algorithm is capable of simulating an RVE with a given volume fraction V_f by generating a population of reinforcement particles. Spheres are sequentially added to a cube of length L, not allowing intersection with each other. With identical spheres (monodisperse), a jamming limit exists and it is not possible to generate volume fractions more than 30%. However, spheres of decreasing sizes can be sequentially added to reach values higher values, up to 60% [73]. Flowchart of the RSA algorithm is given in Figure 4.3.

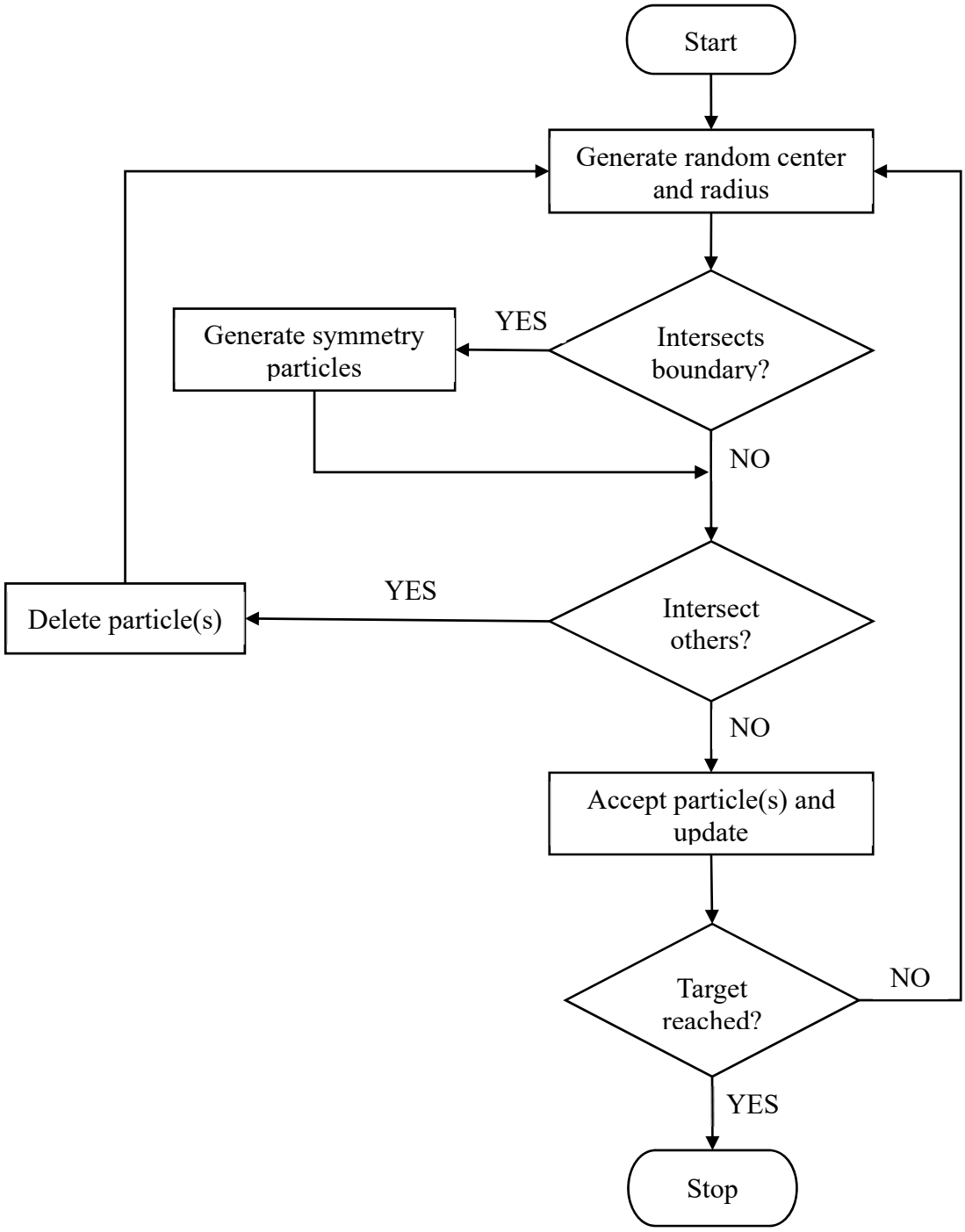

Figure 4.3: Flowchart of the modified-RSA algorithm

Firstly, radii of all incoming particle that satisfies the volume fraction requirement are generated according to desired statistical distribution, and arranged in descending manner. Particle centers are produced using a random number generator, and accepted if the distances between the

its center and previously accepted particles exceed a minimum value of $1.05(R_i + R_j)$, where R_i is the radius of the candidate particle, and R_j is the radius of j-th accepted particle. To maintain periodicity, any particle cutting a face of the unit cell is copied to allowed reappear from the opposite face. The particles are also checked to maintain a minimum distance (one-tenth of particle radius) from the cell face and also between each other in order to generate an adequate finite element mesh. A particle very close to the RVE surface, edge or corner could result in distorted finite elements.

4.2.2 Simulation of creep curves

Once the unit-cell and particle specifications have been generated, an input file readable by ANSYS MAPDL is written, and imported to form a cube with spherical inclusions. Elastic and creep material properties are assigned to the matrix and inclusions. The combined time-hardening constitutive equation delivers a good model for the primary and secondary stages of creep. It is described by a total of 7 parameters. The constitutive equation is given in the ANSYS documentation as creep strain ϵ_{cr} as a function of time t, stress σ, and temperature T:

$$\epsilon_{cr} = \frac{C_1 \sigma^{C_2} t^{C_3+1} e^{-\frac{C_4}{T}}}{C_3 + 1} + C_5 \sigma^{C_6} t e^{-\frac{C_7}{T}}, \tag{4.3}$$

where C_1 through C_7 are the material creep parameters used to fit experimental data. The constants C_4 and C_7 can be assumed to be zero as temperature dependence is not considered. In a single-inclusion unit-cells, only a quarter (for 2D) or one-eighth (for 3D) of the particle-matrix system is modeled as result of symmetry. The inclusion and matrix regions are meshed using 8-noded 2D quadrilateral elements (element type: PLANE183) for the 2D axisymmetric model, or 10-noded 3D tetrahedral elements (element type: SOLID187) of the 3D unit-cell or 3D SRVE models. Elements at the matrix-inclusion interfaces matrix are further refined.

4.2.2.1 Boundary conditions

The orthogonal mixed-boundary condition (OMBC) is imposed on the micromodels. Symmetry boundary condition are applied to the inner surfaces, and iso-displacement boundary conditions are imposed on the outer. An iso-displacement condition is applied a face by coupling normal displacements of all nodes on it. A uniaxial tensile load is applied in the x-direction to simulate creep behavior of the RVE. Figure 4.4 illustrates the three-different unit-cell models considered in this study.

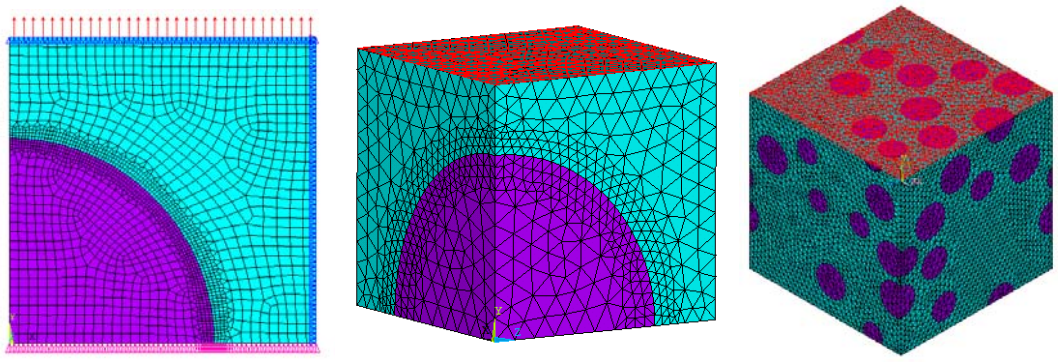

a) b) c)

Figure 4.4: Mesh and boundary conditions for a) 2D unit-cell, b) 3D unit-cell, and c) 3D SRVE. (Figures have different scales)

The models are implemented using ANSYS Mechanical APDL R16.0-17.2. Owing to the large number of degrees-of-freedom to be solved, High Performance Computer (HPC) Philip at Louisiana State University is used. A node of the supercomputing cluster has two 4-core 2.93 GHz Quad Core Nehalem Xeon 64-bit processors with 24GB 1333MHz RAM. Using volume averaging over total elements N, the effective creep strain at current time t for a prescribed volume fraction and load is determined by:

$$\bar{\epsilon} = \frac{1}{V}\sum_{\beta=1}^{N} V^{(\beta)}\,\epsilon^{(\beta)}, \tag{4.4}$$

and the total unit-cell volume is given by:

$$V = \sum_{\beta=1}^{N} V^{(\beta)}. \tag{4.5}$$

4.2.3 Estimation of creep properties

A microscale FE creep analysis is performed for different macroscopic loads. For random microstructures, the homogenized behavior depends of the size of the RVE. The RVE size L should be significantly larger than the particle radius r so as to contain sufficient microstructural features. With increasing size of the RVE, the effective properties tend to become independent of the applied boundary conditions. To study the existence of RVE, a statistical analysis based on mathematical expectation and standard deviation is performed using a series of samples with: i) increasing RVE size, and ii) multiple realizations i.e. samples from different inclusion locations with the same particle volume fraction. For the SRVE model, numerical averaging is performed over several samples to reduce computational resource requirements. The process is repeated for different tensile load values, and the creep curves obtained are fitted to the parent creep constitutive equation to estimate the creep parameters C_1 through C_7. The operation is now performed for successively higher volume fractions until creep parameters for the entire range are evaluated. The ability to estimate the creep parameters over a range of volume fractions forms the basis of the multiscale framework. The operation is then performed for successively higher volume fractions until creep parameters for the entire range are evaluated. To establish the accuracy of homogenized material behavior, it is important to check convergence characteristics of finite element solutions. The convergence of numerical results is investigated by successive refinement of mesh density, time-increments each time halving the corresponding values. The ability to estimate the creep parameters over a range of volume fractions forms the basis of the multiscale framework.

4.2.4 Estimation of thermoelastic properties

In the present study, the Mori-Tanaka scheme [66] is used to determine the elastic properties of the composite. It is applicable for microstructure with a continuous matrix and randomly dispersed spherical particulate phase, and considers the interaction of elastic fields among neighboring inclusions:

$$\frac{K-K_1}{K_2-K_1}=\frac{V}{1+\frac{(1-V)(K_2-K_1)}{K_1+\frac{4}{3}\mu_1}}$$
$$\frac{\mu-\mu_1}{\mu_2-\mu_1}=\frac{V}{1+\frac{(1-V)(\mu_2-\mu_1)}{\mu_1+f_1}} \tag{4.6}$$
$$f_1=\frac{\mu_1(9K_1+8\mu_1)}{6(K_1+2\mu_1)},$$

where K_i and μ_i are the bulk and shear moduli of the two constituents $(i=1,2)$ respectively, related to the Young's modulus and Poisson's ratio as:

$$K_i=\frac{E_i}{2(1+v_i)}$$
$$\mu_i=\frac{E_i}{3(1-2v_i)}. \tag{4.7}$$

The Rosen-Hashin relation [70] is useful for estimating the homogenized coefficients of thermal expansion α:

$$\frac{\alpha-\alpha_1}{\alpha_2-\alpha_1}=\frac{\frac{1}{K}-\frac{1}{K_1}}{\frac{1}{K_2}-\frac{1}{K_1}}, \tag{4.8}$$

where α_i are the coefficient of thermal expansion of the two constituents $(i=1,2)$.

The thermal conductivity k is estimated utilizing the Hatta-Taya relation [69]:

$$\frac{k-k_1}{k_2-k_1}=\frac{V}{1+\frac{(1-V)(k_2-k_1)}{3k_1}}, \tag{4.9}$$

where k_i are the thermal conductivities of the two constituents $(i = 1, 2)$.

The density ρ is calculated using the rule of mixture:

$$\rho = \rho_1(1-V) + \rho_2 V, \tag{4.10}$$

where ρ_i are the densities of the two constituents $(i = 1, 2)$.

4.3 Analysis at the macroscale

Considering radial symmetry, an axisymmetric domain of the hollow cylinder is modeled in ANSYS MAPDL to reduce computational costs. The dimensions, and loadings, mesh and boundary conditions are shown in Figure 4.5. The cylinder has inner and outer radii a and b respectively, and is exposed to an internal pressure p_a, external pressure p_b, angular speed ω, and a heat-flux of q at the outer wall. The inner wall is held reference temperature of zero. The thermoelastic problem is at first decoupled, and the thermal portion solved to input the temperature solution into the mechanical problem. The user programmable feature USERMATTH is used for the implement the functional gradation. This is done by defining a field variable (local volume fraction of constituent 2) at a number of design points in the radial direction.

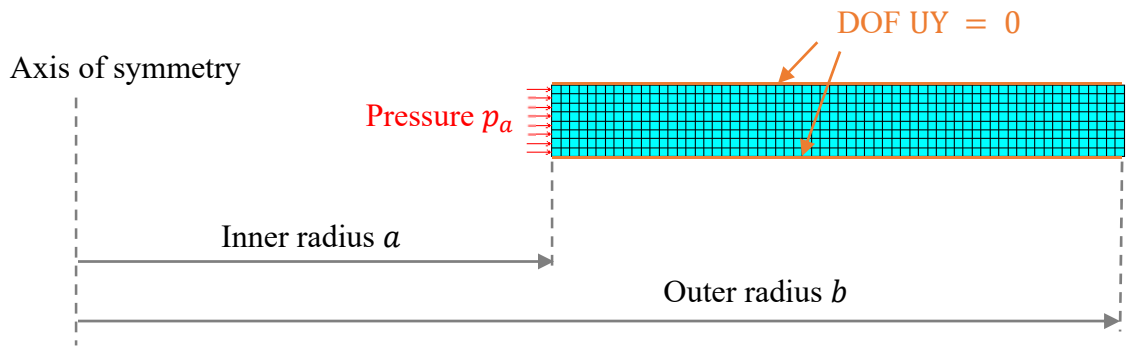

Figure 4.5: FE model for macroscale

A volume fraction profile is implemented to the model by assigning the local volume fraction to each node as an initial state value. Spatial variations of material properties are frequently calculated using simple homogenization schemes by assuming constituent volume fractions in the form of power-law, polynomial, exponential and sigmoidal functions. In this study, a power-function profile is used to smoothly vary the volume fraction of constituent 2 in the radial direction:

Power function profile:

$$V_2 = V_a + (V_b - V_a)\left(\frac{r-a}{r-b}\right)^p, \tag{4.11}$$

where V_a and V_b are the volume fractions at the inner $(r = a)$ and outer $(r = b)$ surfaces respectively, and p is the gradation parameter controlling the shape of the profile. At intermediate volume fraction values, the material properties are automatically calculated by linear interpolation. Initial elastic stress-strain analysis at the macroscopic level is followed by time dependent creep analysis.

4.4 Multi-objective optimization of FGM cylinder

A numerical procedure is presented to determine the optimal material distribution of a functionally graded cylinder undergoing creep deformations. The procedure uses graded finite elements in determining the creep solution and avoids the disadvantage of discretizing the domain into numerous homogeneous layers. Otherwise, the number of design points would be vastly increased, and making the optimization problem difficult to solve. The parallel implementation drastically reduces the total time for completion of the algorithm.

4.4.1 Multiple objective problem

Optimization problems with multiple objectives are commonly encountered in engineering applications. In such cases, the objectives frequently conflict with each other, and instead of a single solution, several solutions with best possible trade-offs are sought for. Multi-objective problem are as follows:

minimize $f_1(x), f_2(x), \dots f_k(x)$

subject to

$$g_i(x) \leq 0, i = 1, 2, \dots m$$

$$h_i(x) = 0, i = 1, 2, \dots p,$$

where $x = [x_1, x_2, \dots x_n]^T$ is the decision variable vector, g_i and h_i represent the constraint functions respectively.

4.4.2 Particle swarm optimization

Particle swarm optimization (PSO) is used to solve the multi-objective optimization problem. It is a heuristic search technique inspired by the movement of a flock of birds aiming to find food. PSO has been found to be effective in engineering structural optimizations. It is a derivative free, population based method that is easily parallelized, and have fewer parameters than other algorithms such as GA. In PSO, a number of particles 'fly' through a multi-dimensional search space to explore for the best solution for the optimization problem. The position of particle i in a swarm of p particles is randomly initialized, and updated at each iteration using:

$$x_{k+1}^i = x_k^i + v_{k+1}^i, \tag{4.12}$$

where a pseudo-velocity v_{k+1}^i represents the socially exchanged information and is calculated by:

$$v_{k+1}^i = w_k v_k^i + c_1 r_1 \left(p_k^i - x_k^i\right) + c_2 r_2 \left(p_k^g - x_k^i\right), \tag{4.13}$$

and k is the pseudo-time, p_k^i is the best position of particle i, and p_k^g is the global best position in the swarm. c_1 and c_2 are cognitive and social scaling parameters representing the attraction of a particle towards its own success or that of its neighbors. These are usually set at 2 to allow greater search area. w_k is the inertial weight which is reduced from an initial value to allow more refined search with time:

$$w_{k+1} = \eta w_k. \tag{4.14}$$

If a particle flies beyond the feasible search space, a 'fly-back mechanism' forces the particle back to the feasible space by positioning at the boundary. For single-objective optimization problems, each particle updates its position based on that of a leader particle. However, in multi-objective problems, the particles have a set of leaders from which one is selected. These leaders are the non-dominated solutions stored in an external achieve known as the repository. The contents of the repository are final output of the algorithm.

The pseudo code of the general PSO is as follows:

Begin

initialize swarm

locate leader

$g = 0$

while $g < g_{max}$

for each particle

update position

evaluation

update p_{best}

end

update leader

g++

end

end

For parallel implementation, the fitness evaluations are performed independently on a parallel machine. The local and global best positions are updated after all evaluations have been completed; the time required to evaluate the swarm is dictated by the slowest evaluation within the swarm.

4.4.3 Problem description

A thick-walled functionally graded cylinder is subjected to internal pressure p_a, rotation ω, and heat flux q at the outer surface for time t. A radial material gradation is characterized by j design points along the radius having volume fraction V_j. The objective of this study is to determine the material distribution for which the maximum effective stress at the beginning and maximum creep strain at end time are as small as possible:

Find $V_j, j = 1 \ldots n$

minimize $\sigma_e(r),\ \epsilon_{cr}(r)$

subject to $V_{min} \leq V_j \leq V_{max}$

A multi-objective particle swarm optimization [128], [129] is employed to solve the problem.

CHAPTER 5: NUMERICAL RESULTS

In the previous chapter, procedures for the proposed analytical, and numerical models for the computation of creep stress and strains histories were elaborated. This chapter presents a collection of important numerical results and observations resulting from the studies. Effects of important material gradient indices are investigated and discussed. Qualitative insights into the creep behavior of FG cylinders, and numerical benchmark data for qualification of numerical solutions are established.

5.1 Thermoelastic solutions

Thermoelastic and time-dependent creep response of the cylinder having inner radius $a = 0.5$ m and outer radius $b = 0.75$ m have been investigated. Material properties used are $E_0 = 200$ GPa, $\nu = 0.3$, $\alpha_0 = 1.2\times10^{-5}\,\mathrm{K}^{-1}$, and $\rho_0 = 7800\,\mathrm{kg/m}^3$. Creep data are assumed to be $n = 3.75$, and $B_0 = 1\times10^{-11}\mathrm{MPa}^{-n}\mathrm{h}^{-1}$. Gradient indices are varied from -2 to $+2$ to illustrate the influence of material property distributions on thermoelastic and creep stress-strain behaviors. A positive index value represents that the physical property at the outer surface is higher than that of the value at the inner surface (with a non-linear radial distribution according to the power-law), and a negative value indicates lower property value.

The formulation includes solutions for combined mechanical and thermal loadings. Typically, studies have performed illustrative examples by taking equal functional grading exponents e.g. $m_1 = m_2 = m_3 = m_4 = m_5 = m$. Controlling all material distributions using a single parameter fails to demonstrate how responses are influenced by individual material gradations, which becomes a primary motivation in materials selection and tailoring of FG structures. Parametric studies are thus performed by varying each index form -2 to $+2$, while keeping the others constant at 1. Plots become more revealing when parametric studies are

separately performed for applied pressures, rotation and heat generation in convective environments only. Firstly, stress distributions along the cylinder wall thickness at zero time are calculated; creep strain components are zero.

Figure 5.1 shows the effect of Young's modulus distribution on the stress components due to internal pressure only ($p_a = 50$ MPa). For all values of m_1, radial stresses are -50 MPa at $r = a$, and zero at $r = b$, ensuring that mechanical boundary conditions have been satisfied. Hoop and axial stress distributions are tensile due to the application of internal pressure, and with the increase of index m_1, hoop and axial stress values at the inner surfaces decrease, and magnitudes at the outer surface increase. Von Mises stress distribution gives an effective representation of the influence of material property inhomogeneity on stress states, and will be considered for the latter case illustrations. In this case, von Mises stress takes a homogenized profile throughout the cylinder for $m_1 = 2$. Thus, Young's modulus variation along the cylinder has significant effect on stress distributions, and an appropriate gradation can be used to attain optimal stresses profiles.

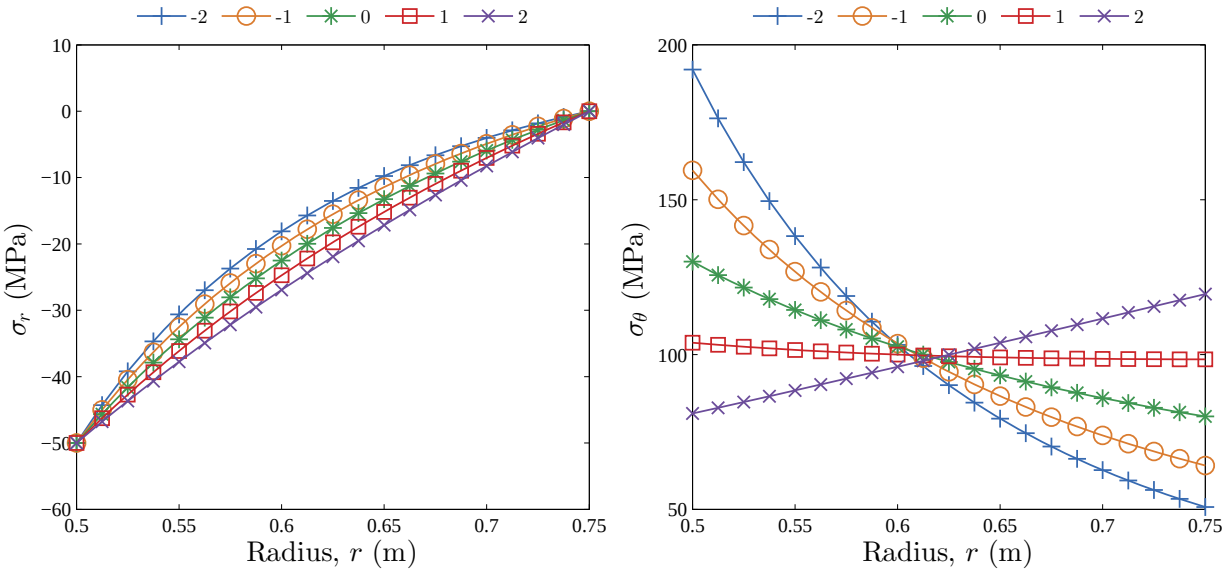

a) b)

Figure 5.1: Effect of m_1 on a) radial, b) circumferential, c) axial, and d) von Mises stress distributions along the cylinder thickness for pressure loading only ($p_a = 50$ MPa)

(Figure 5.1 continued)

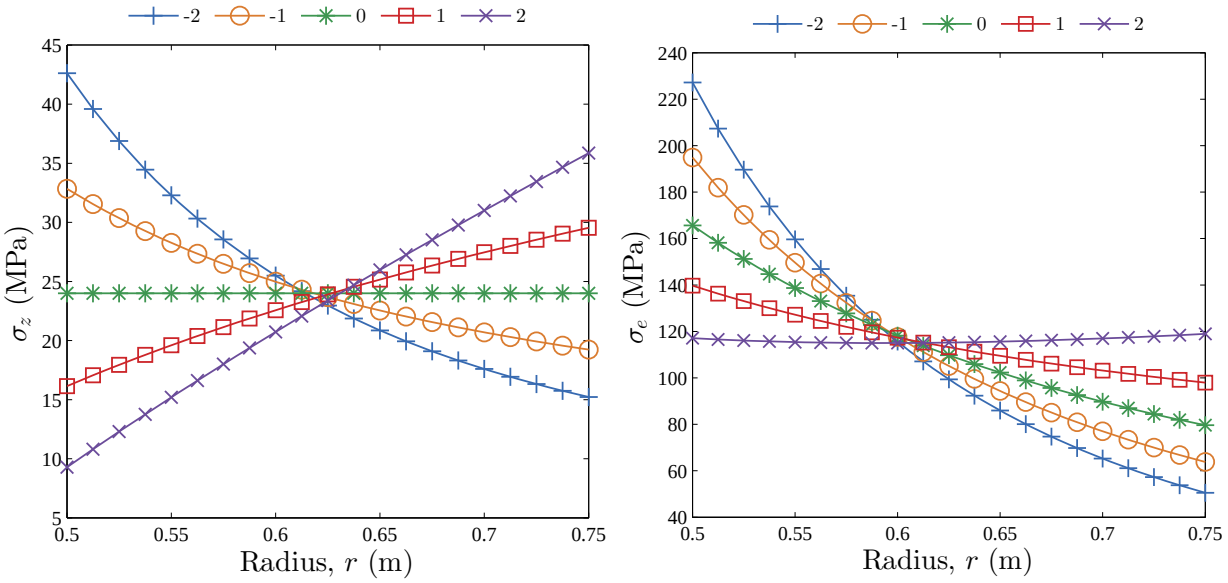

c) d)

Figure 5.2 shows the effect of gradient indices on von Mises stress distribution due to angular speed only ($\omega = 1200$ rpm). In Figure 5.2 a), when m_1 changes from -2 to $+2$ von Mises stress decreases at the inner surface and increases the outer surface. Circumferential and axial stress distributions have similar trends, with axial stress being the dominant component. Radial stresses are much smaller compared to the other components. It is noticed that an appropriate gradation of Young's modulus can be used to redistribute stresses. Figure 5.2 b) illustrates that von Mises stress increases throughout the entire thickness of the cylinder with the increase of m_3. Circumferential and axial stresses show similar trend with circumferential stress as the dominant component. Radial stresses are again comparatively small. Thus, reduction of density along the radius of the cylinder will reduce effective stresses in the entire cylinder.

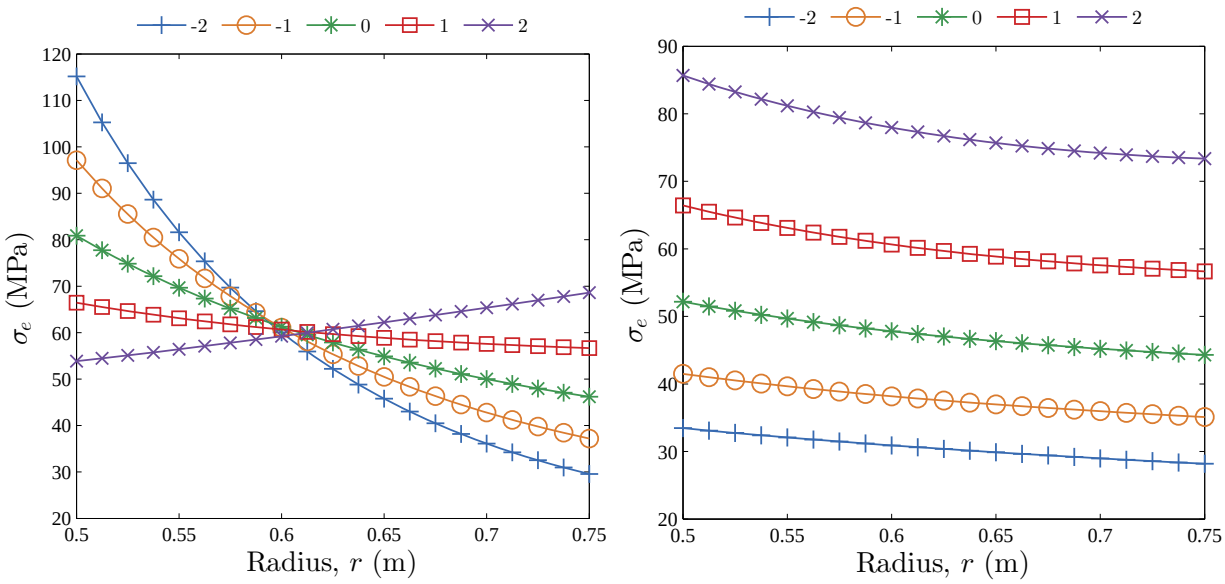

a) b)

Figure 5.2: Effect of a) m_1, and b) m_3 on von Mises stress profile due to angular speed ($\omega = 1200$ rpm)

Figure 5.3 shows the effect of different gradient indices on von Mises stress distribution due to heat generation in thermally conductive environments.

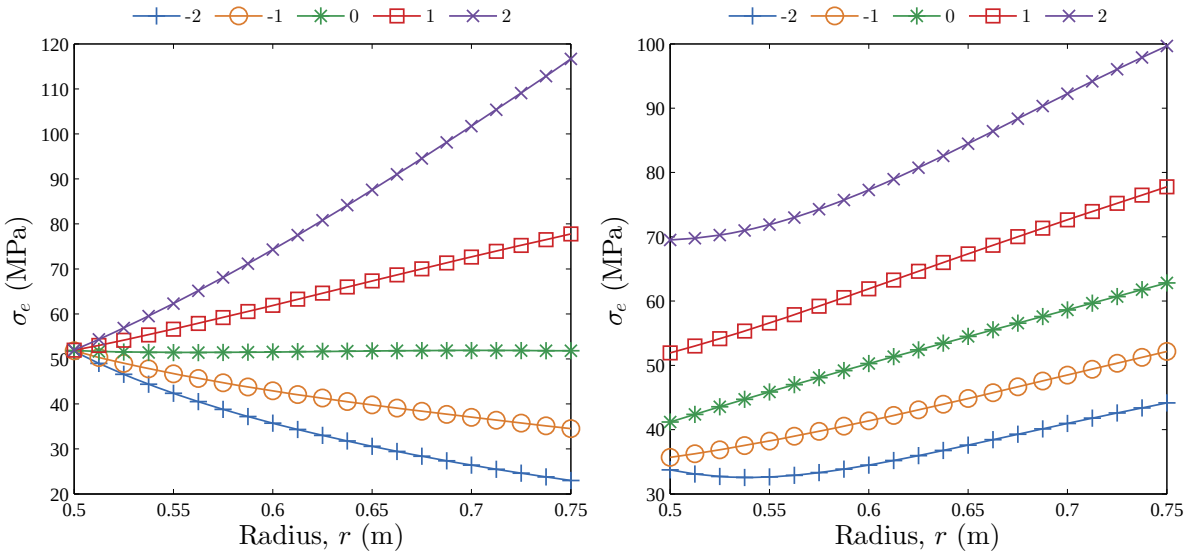

a) b)

Figure 5.3: Effect of a) m_1, b) m_2, c) m_4, and d) m_5 on von Mises stress profile due to heat generation in thermally convective environment ($\dot{q}_0 = 5000\ \mathrm{W/m^3}, T_{in} = 20\ ^\circ\mathrm{C}, T_{out} = 0\ ^\circ\mathrm{C}, h_{in} = h_{out} = 100\ \mathrm{W/(m^2{}^\circ C)}$)

(Figure 5.3 continued)

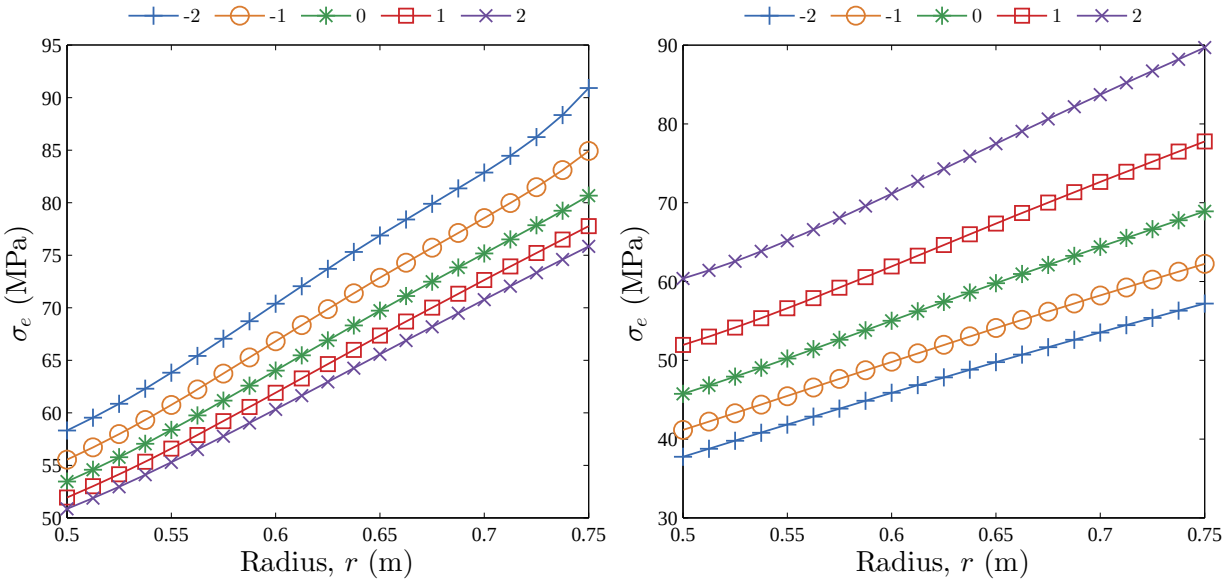

c) d)

Figure 5.3 a) illustrates that with the increase of m_1, stress remains the same at the inner surface of the cylinder and increase at the outer. Thus, reduction of Young's modulus along the radius of the cylinder reduces effective stresses. Figure 5.3 b) shows as m_2 increases, stress throughout the cylinder increases. Thus, gradually decreasing coefficient of thermal expansion along the cylinder reduces the effective stresses. Figure 5.3 c) shows that with the increase of m_4, stress throughout the cylinder decreases. So, a higher thermal conductivity is favored at the outer surface of the cylinder. Figure 5.3 d) shows that when m_5 increases, effective stress throughout the cylinder also increases.

5.2 Creep behavior

In this section, results obtained from the time-dependent creep study are discussed.

5.2.1 Comparison with existing literature and validation

Nejad and Kashkoli [58] studied time-dependent deformations of an FG cylinder without considering any heat generation. Equivalent data used in their illustrative example are $a = 20$ mm, $b = 40$ mm, $E_0 = 207$ GPa, $\nu = 0.292$, $\alpha_0 = 10.8\times10^{-6}\ \mathrm{K}^{-1}$, $p_a = 80$ MPa, $p_b = 0$ MPa, heatflux $= 3000\ \mathrm{W/m^2}$, $k_0 = 43\ \mathrm{W/(m.\,°C)}$, $h_{out} = 6.5\ \mathrm{W/(m^2.\,°C)}$, $T_{out} = 25$ °C, $B_0 = 1.4\times10^{-8}$, $n = 2.25$, $\omega = 1200$ rpm, and $\rho_0 = 7798\ \mathrm{kg/m^3}$.

To verify the time-dependent solutions, finite element analysis (FEA) is performed using a commercial program, ANSYS Mechanical APDL R16.0. Functional gradation is implemented by dividing the cylinder into a large number of homogeneous layers in the radial direction, and discretizing using 8-noded elements for thermal and structural analyses. Material gradation in the finite element model is shown in Figure 5.4.

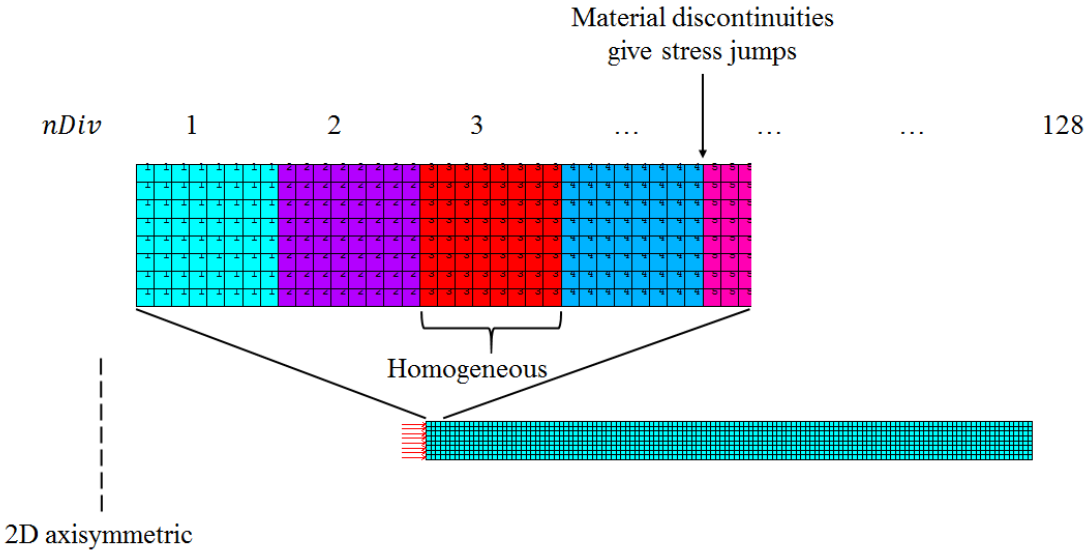

Figure 5.4: Finite element modeling of FG cylinder using ANSYS R16.0

Using the numerical procedure described in Section 3.2.2, stress distributions along the radial coordinate after every 64 time-steps are displayed in Figure 5.5. It is clear that creep effects on radial stresses is small, but that on circumferential and axial stress distributions are significant.

With elapsing time, σ_r, σ_θ, and σ_z redistribute and tend reach a steady state. It can be seen that the stress values become more uniform throughout the cylinder with time. The entire axial stress distribution decreases considerably during the creep process. There is good agreement between the iterative solutions and those using FEA.

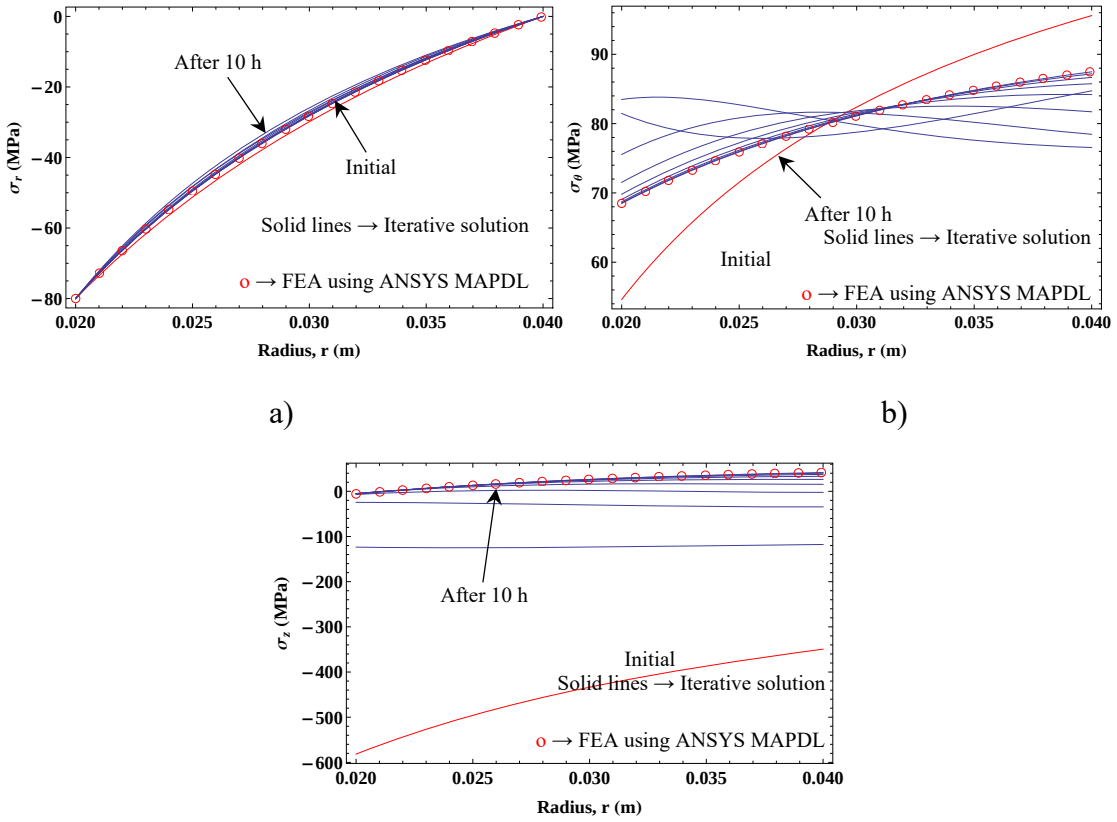

Figure 5.5: Time-dependent stress redistributions for 10 h: a) radial, b) circumferential, and c) axial

Evolution of circumferential stress and strain at the inner and outer surfaces are plotted in Figure 5.6. Strain rate initially decreases and reaches a constant value with time. Strain rate at the inner surface is higher than that at the outer. During the initial period, there is significant increase in circumferential stress at the inner surface, and the value then decays to a steady-state value. The converse holds true at the outer surface. Good agreement is observed between iteratively calculated stress/strain histories and that obtained from FEA using ANSYS MAPDL R16.0, demonstrating

accuracy of iterative solutions. It is to be noticed that during the initial redistributions, the cylinder experiences peak stress values much higher than initial or steady state levels which would not be revealed in a steady-state creep analysis. Thus, time-dependent analyses are vital of design of FG thick cylinders.

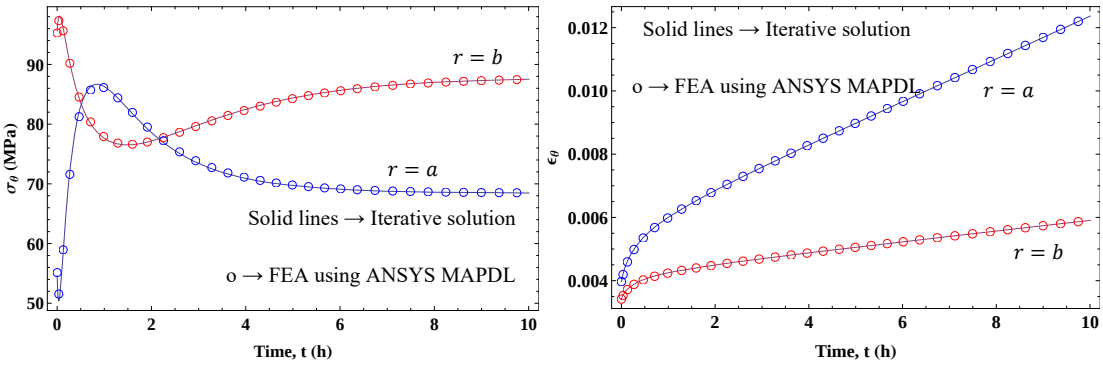

a) b)

Figure 5.6: Evolution of circumferential a) stress, and b) strain at $r = a$ and $r = b$ for 10 h

5.2.2 Parametric studies

The method is used to investigate the influence of material property distributions on time-dependent behavior in FG cylinders. Parametric studies are once again performed by changing the value of each index from -2 to $+2$, while the others are kept constant at 1 for applied pressures, rotation, and heat generation in convective environments respectively.

Figure 5.7 shows creep responses due to internal pressure only ($p_a = 50$ MPa) for different Young's modulus and creep coefficient profiles. Figure 5.7 a) and b) show the effect of elastic graded factors on the evolution of circumferential stress and strain at inner surface. For all values of m_1, stresses appear to converge to the same value. The same behavior holds for radial and axial stresses. Thus, steady state stress values are independent of elastic distribution. Strain at the inner surface increases with time, and for different values of m_1, the curves become parallel to each other. Figure 5.7 c) and d) show the effect of creep coefficient gradation on the circumferential

stress and strain histories at the inner surface. For higher values of m_6, steady state stresses, and strain rates are also higher. So, smaller creep coefficient at the outer surface leads to smaller creep rates in the entire cylinder.

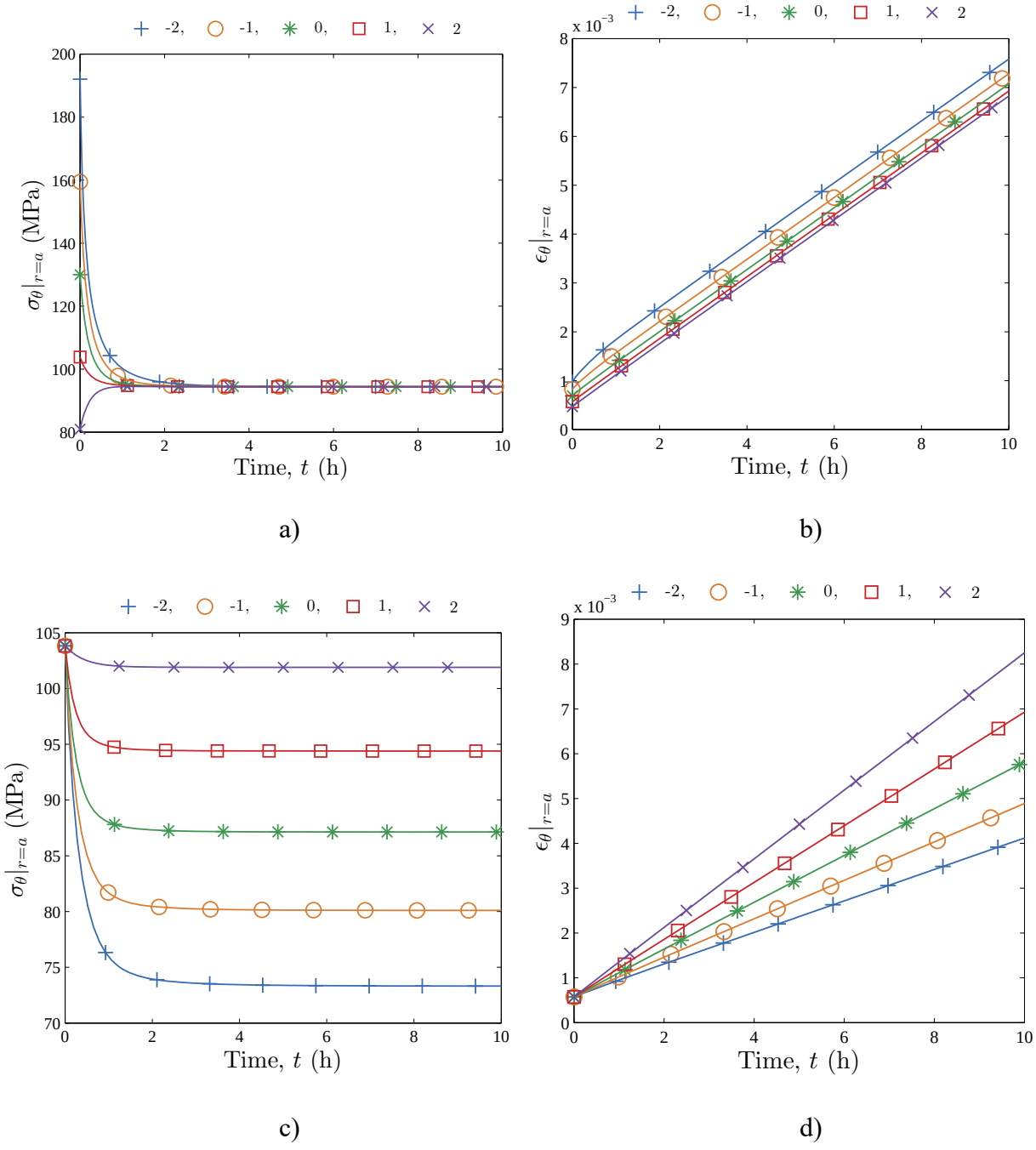

Figure 5.7: Effect of a) m_1 on circumferential stress, b) m_1 on circumferential strain, c) m_6 on circumferential stress, and d) m_6 on circumferential strain, at $r = a$ for pressure loading only, ($p_a = 50$ MPa)

Figure 5.8 illustrates time-dependent behaviors of the cylinder subjected to rotation only ($\omega = 1200$ rpm) for different density and creep coefficient profiles.

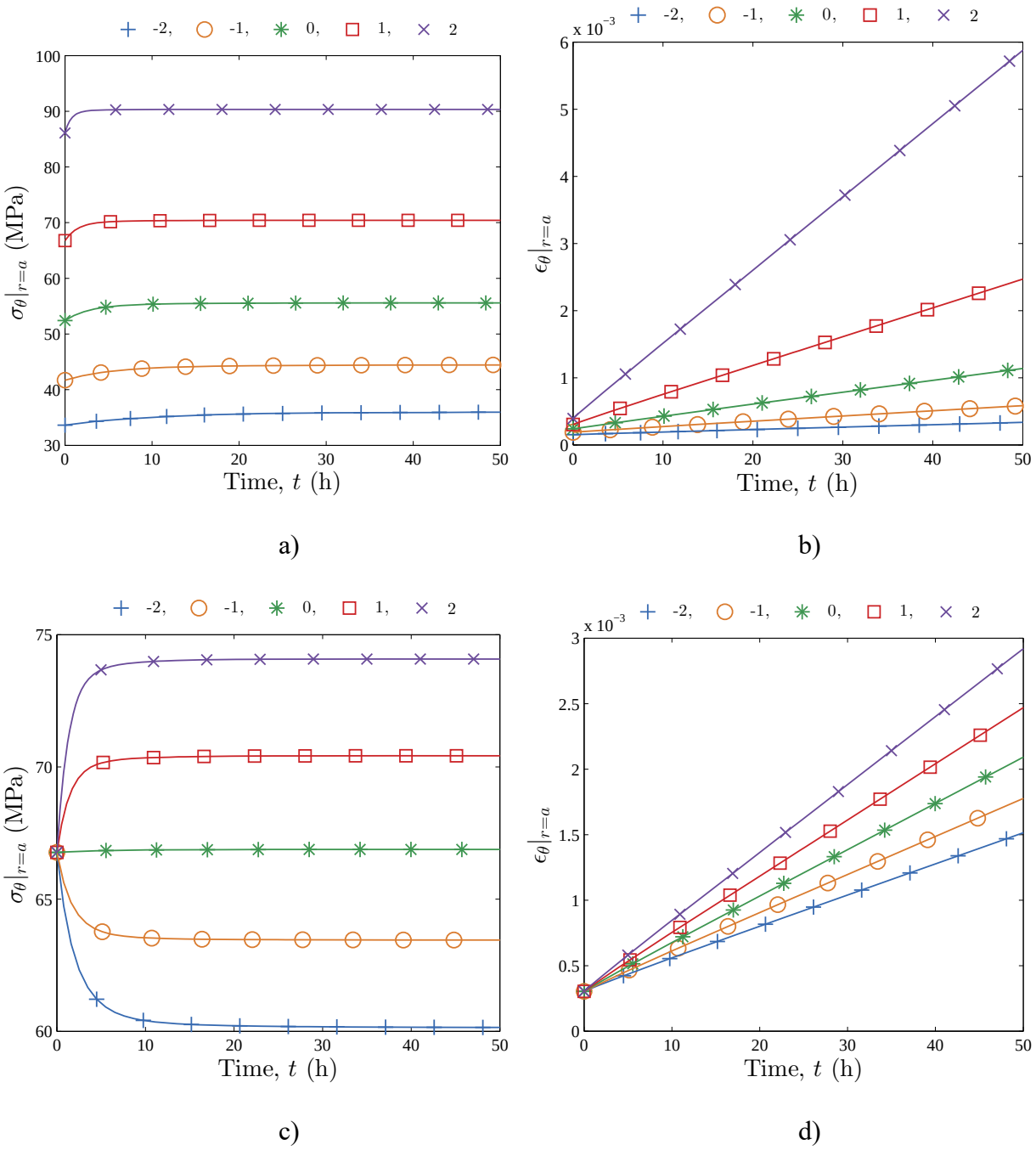

Figure 5.8: Effect of a) m_3 on circumferential stress, b) m_3 on circumferential strain, c) m_6 on circumferential stress, and d) m_6 on circumferential strain at $r = a$ due to rotation only, ($\omega = 1200$ rpm)

Figure 5.8 a) and b) shows the development of circumferential stress and strains at the inner surface for different density distributions. Steady state stresses, and strain rates are higher for larger values of m_3, i.e. stress and creep rate at the inner surface is significantly higher when the density along the radius is gradually increased. Figure 5.8 c) and d) show the effects of creep coefficient gradation on the evolution of circumferential stress and strain at the inner surface. Higher steady stress and creep rate is experienced at the inner surface when creep coefficient is gradually increased along the radius. Gradation of Young's modulus has no effect on long-term response of the cylinder. Figure 5.9 shows the effects of different gradient indices of the time-dependent strains due to heat generation in a thermally convective environment. Coefficient of thermal expansion, thermal conductivity, and heat generation rate distributions only affect the initial thermoelastic behavior, but the influences decrease with time. This occurs because stresses due to the temperature field quickly relaxes to low values, and do not contribute significantly to the strain evolution.

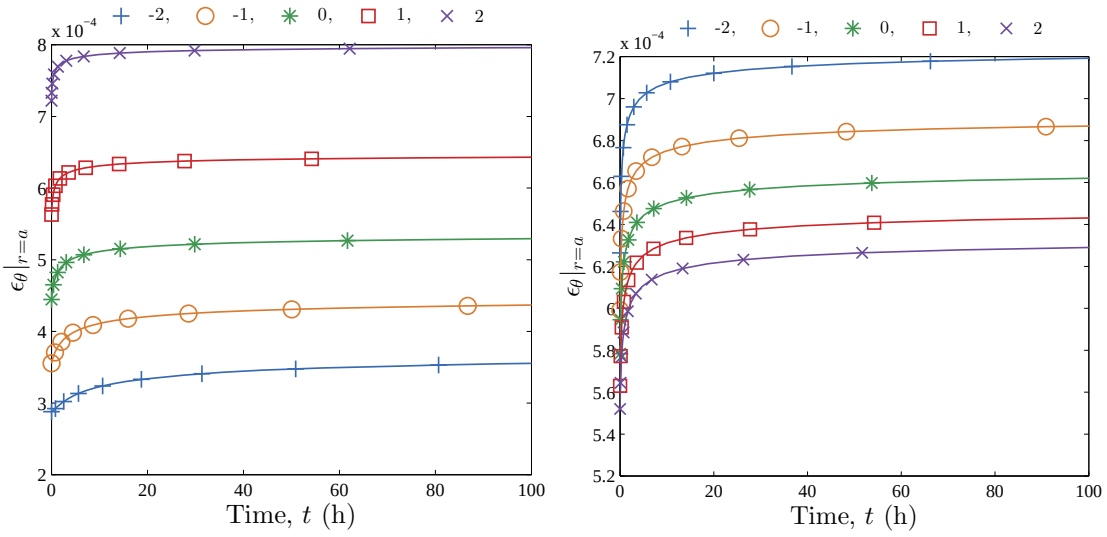

Figure 5.9: Effect of a) m_2, b) m_4, and c) m_5 on the evolution of circumferential strain at $r = a$ due to heat generation in thermally convective environment ($\dot{q}_0 = 5000\ \mathrm{W/m^3}, T_{in} = 20\ ^\circ\mathrm{C}, T_{out} = 0\ ^\circ\mathrm{C}, h_{in} = h_{out} = 100\ \mathrm{W/(m^2{}^\circ C)}$)

(Figure 5.9 continued)

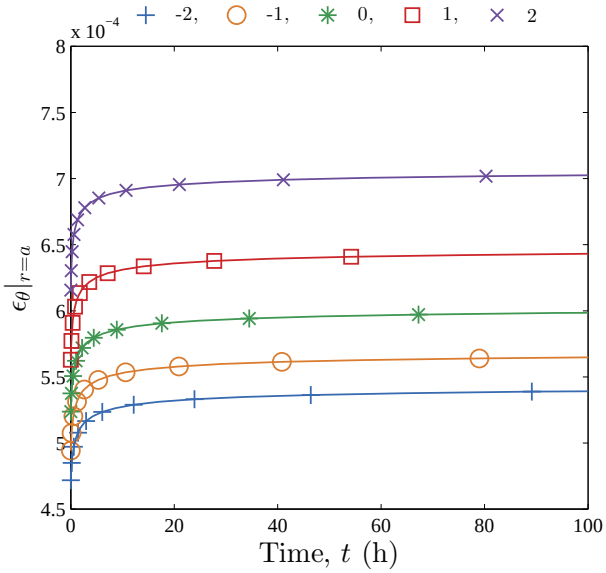

c)

5.3 Multiscale framework results

Computational limitations make traditional numerical methods unrealistic and ineffective in modeling detailed spatial heterogeneities within FGMs. A practical approach is to predict the material behavior by solving a boundary value problem of an idealized microstructure, and incorporating it into the macro-model. The idealized microstructure, known as the representative volume element (RVE) is commonly modeled by two methods. The first one is a unit-cell model, which is the smallest repeatable geometry in the RVE, e.g. a single inclusion within a domain. The model inherently assumes regular microstructural arrangements, which does not always correspond to real microstructures. The second approach is by generating a larger domain - the statistically representative volume element (SRVE) - which includes sufficient microstructural features into the domain, and captures the random arrangement of heterogeneities. However, this requires greater computational effort and expenses. It should be noted that any assumptions made

on the ideal model affects the predictive capacity of solutions. Estimation of structural response would enable the efficient exploration of material gradation within the design space.

The focus of this research is to develop a multiscale framework to predict the creep response of a FG pressure vessel. To demonstrate the capability of the framework, simulations are performed for a FG vessel composed of discontinuous SiC inclusions within a homogeneous creeping Al matrix. Three different micromechanical models are compared: i) 2D unit-cell, ii) 3D unit-cell, and iii) 3D SRVE. The 2D axisymmetric and 3D unit-cell models represent regularly arranged reinforcements, while the 3D SRVE closely depicts the random distribution of particles. The creep responses of FG thick cylinders are modeled in two steps. The first step involves the micromechanical finite element modeling over a range of volume fractions of SiC particles dispersed in Al matrix to predict the overall mechanical properties. The second step requires modeling the FG structure using material properties evaluated in the first step. The variation of local effective properties in FGMs are characterized by gradual change of volume fraction of the two constituents. The results from the FE analysis of three micromodels are described first, followed by that from macro-model.

5.3.1 Results of homogenized creep properties from different micro models

The homogenized creep properties are presented for a range of volume fractions using different micromechanical models. Silicon carbide particle reinforced aluminum composite is considered for the FGM. This material combination is chosen since it is widely considered for high temperature applications. SiC typically does not undergo noticeable deformation with time compared to Al. As a result, it can be modeled as a non-creeping, elastic material. As for aluminum, the combined time-hardening creep constitutive model incorporates primary and secondary deformation stages. The material properties of Al and SiC are tabulated in Table 5.1. The creep

parameters have been reported by Lee, et al. [91] by fitting experimental data of Al-1.5Mg obtained from work of Krajewski, et al. [92].

Table 5.1: Elastic and creep properties of Al-6061 and SiC

Material	$\boldsymbol{E}$ **(GPa)**	$\boldsymbol{\nu}$	$\boldsymbol{C_1}$	$\boldsymbol{C_2}$	$\boldsymbol{C_3}$	$\boldsymbol{C_5}$	$\boldsymbol{C_6}$
Al	68.3	0.345	2.07e-7	0.5	-0.55	1e-22	7.6
SiC	470	0.17	-	-	-	-	-

For a given volume fraction, creep strain versus time curves are obtained for different load values. A commercial package, ANSYS Mechanical APDL R16.0 is used to solve and post-process the creep results for the FEM. To model the particles and matrix, PLANE183 (8 node quadrilateral) elements are used for 2D simulations, and SOLID187 (10 node quadratic tetrahedral solid) elements for 3D. The creep curves are fitted to the combined time-hardening equation using the curve-fitting tool in ANSYS MAPDL to estimate the parameters. Figure 5.10 illustrates the variation of homogenized creep strain versus time curves for different stress values of 40, 50, 60, 70 and 80 MPa obtained using the 2D unit-cell model of 20% SiC composite.

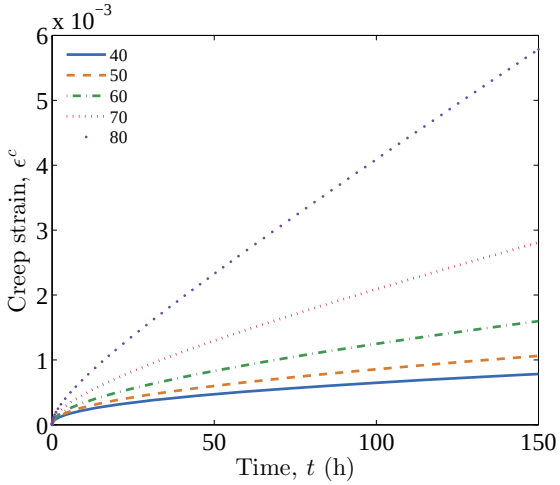

Figure 5.10: Homogenized creep curves for different load values (2D unit-cell model, $V_f = 0.2$)

5.3.1.1 Creep curve fitting

Once the homogenized creep strain versus time output data at different stress levels are obtained, they are fitted to the combined time-hardening equation using a curve-fitting tool in ANSYS MAPDL. The toolbox determines creep parameters using non-linear regression. Parameters of the parent Al matrix are used as initial seed to obtain a successful solution. A non-normalized error norm is employed, and the results are verified by considering the regression error and comparison with test data. Five parameters: C_1, C_2, C_3, C_5, C_6 are primarily adjusted to fit the simulated creep curves. C_4 and C_7 characterize the temperature dependence of creep curves and are taken as zero. Figure 5.11 shows the fitted surface for $V_f = 0.2$ using the 2D unit-cell model. The markers represent data points obtained from homogenization of micromechanical model, and the surface represents the fitted equation. The procedure is repeated for a range of volume fraction values to incorporate the influence of volume fraction into the FG micromodel.

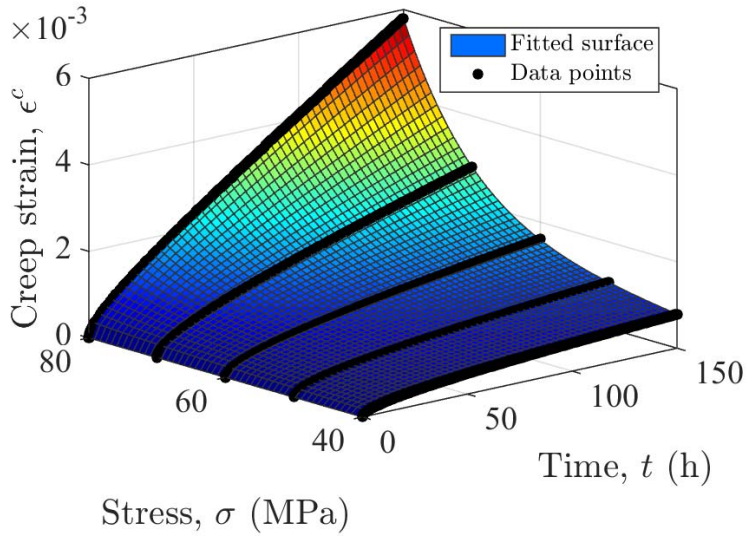

Figure 5.11: Surface fit of creep curves (2D model, $V_f = 0.2$)

5.3.1.2 Convergence study of creep parameters

Typically, the homogenized properties will depend upon the element size and time-step used in the FEA. Convergence checks on mesh and time discretization of finite element solutions are performed prior to providing numerical results. Our particular interests are on homogenized creep curves, and fitted creep parameters. Convergence checks on the mesh and time discretization are performed by successively halving the element size and maximum time-step respectively. Figure 5.12 depicts the convergence characteristics of parameter C_6 obtained from the 2D model for all volume fraction values as the element size or maximum time-step is refined. The values are found to be almost identical for different element sizes of $R/8$ and $R/16$.

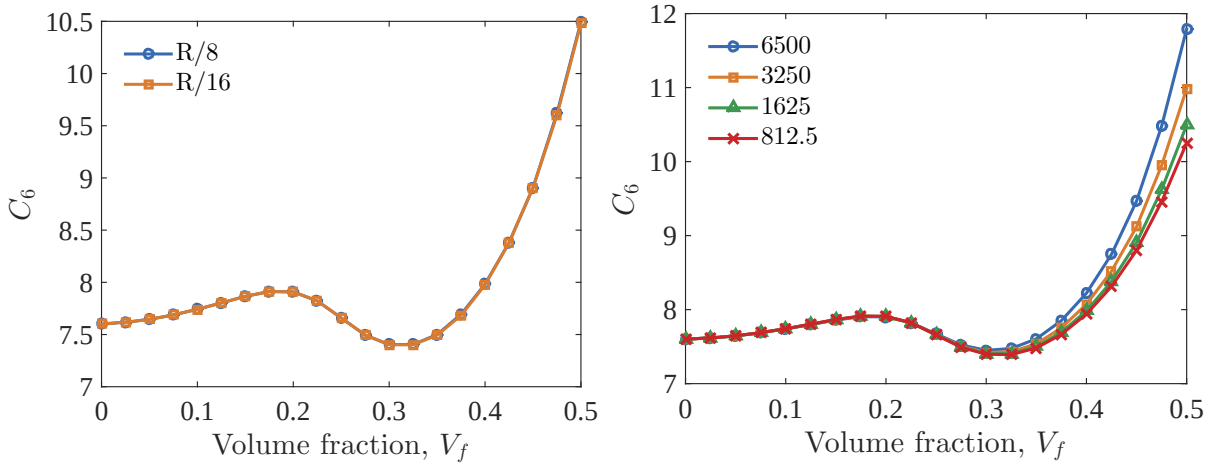

a) b)

Figure 5.12: Sensitivity analysis of parameter C_6 as a function of volume fraction: a) element sizes of $R/8$ and $R/16$, and b) maximum time-step of 6500, 3250, 1625, and 812.5 s

For the time setting convergence study, maximum time-steps of 6500 s, 3125 s, 1625 s, and 812.5 s are considered. Creep parameters are found to be similar for smaller volume fractions, and the differences at higher concentration decreases with successive refinements. There is only a 2.3% change during the final refinement. The maximum time-step have often been controlled by

employing a maximum creep ratio $C_S = 1$ [130]. Although a high value reduces the computational time, it may lead to some discretization error.

5.3.1.3 Comparison of different micromodels

For the multi-particle model, the SRVE size should be much smaller than the length scale of the FGM cylinder but large enough to contain sufficient microstructural features occurring for a particular volume fraction. For small SRVE sizes, there will be variation in homogenized creep response between distinct RVE realizations with the same volume fraction. Figure 5.13 illustrates three SRVE realizations generated for $V_f = 0.2$ and $L = 20$ μm.

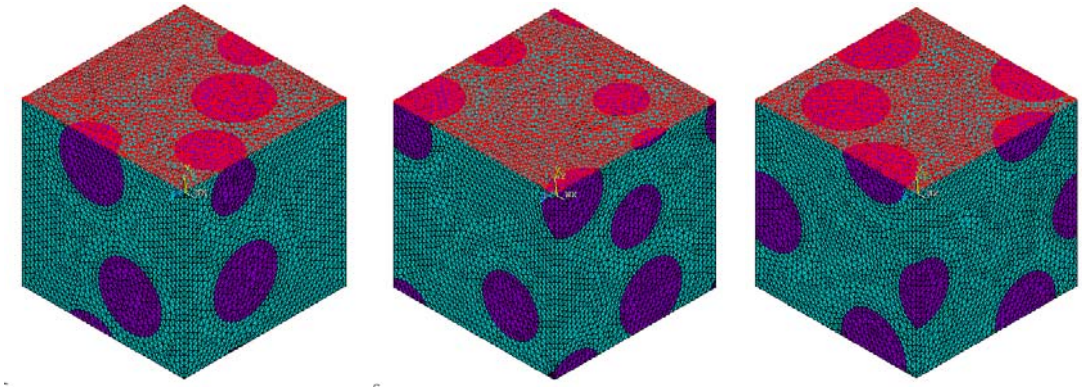

Figure 5.13: Three random RVE samples for $V_f = 0.2011$ and $L = 20$ μm

Figure 5.14 shows the homogenized creep curves for 150 h obtained from 25 different SRVE realizations and the averaged curve for two different RVE lengths $L = 20$ & 40 μm. It is to be noted that volume fraction values are slightly offset of 0.2 for $L = 20$ and 40 μm, because the RVEs can only accommodate full-sized spheres of a fixed radius (mono-disperse). Increasing the RVE size leads to smaller variation of homogenized creep response within the samples, but the average curves remains the same for $L = 20$ and 40 μm. In other words, the ensemble average of homogenized creep response becomes independent of the RVE size. Instead of performing one finite element simulation of a very large SRVE, averaging the homogenized responses over a large

number of smaller RVEs appear to be a computationally more efficient approach. To ensure good accuracy and reasonable run times, the finite element settings listed in Table 5.2 have been used in the simulations.

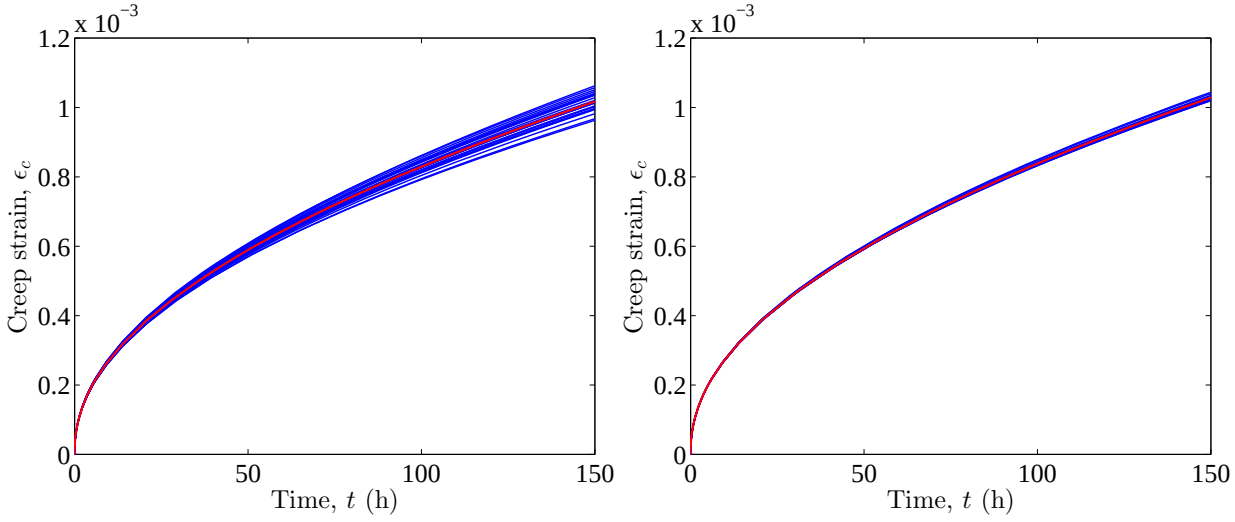

a) b)

Figure 5.14: Average creep curve of 25 realizations for $V_f \approx 0.2$ and $\sigma = 50$ MPa: a) $L = 20$ µm, and b) $L = 40$ µm

Table 5.2: RVE size, number of realizations, and element size used in different models

Model	**RVE size, L (µm)**	**Realizations**	**Element size**
Single-inclusion 2D axisymmetric	varies	-	$R/8$
Single-inclusion 3D	varies	-	$R/4$
Multi-inclusion SRVE	20	20	$L/32$

The final meshes used 2D and 3D unit-cell models contain approximately 2,000 eight-node quadrilateral elements and 30,000 ten-node tetrahedral elements respectively. The 3D SRVE micromodels contain about 250,000 elements and 340,000 nodes. The three-dimensional models require supercomputing facilities. Evaluation of a creep curve from a single realization of 3D SRVE model requires 1.53 h of computing time on an 8-core, 24 GB memory supercomputer, and

that from a 3D unit-cell model takes 0.29 h. The 2D axisymmetric model is far less complex and requires only 68 s. The fitted parameters of the homogenized creep response from different types of FE models (2D, 3D single-inclusion, and 3D SRVE) are plotted as a function of volume fraction in Figure 5.15. In total, 100 individual FE simulations are performed for each single-inclusion model, and 700 for the 3D SRVE.

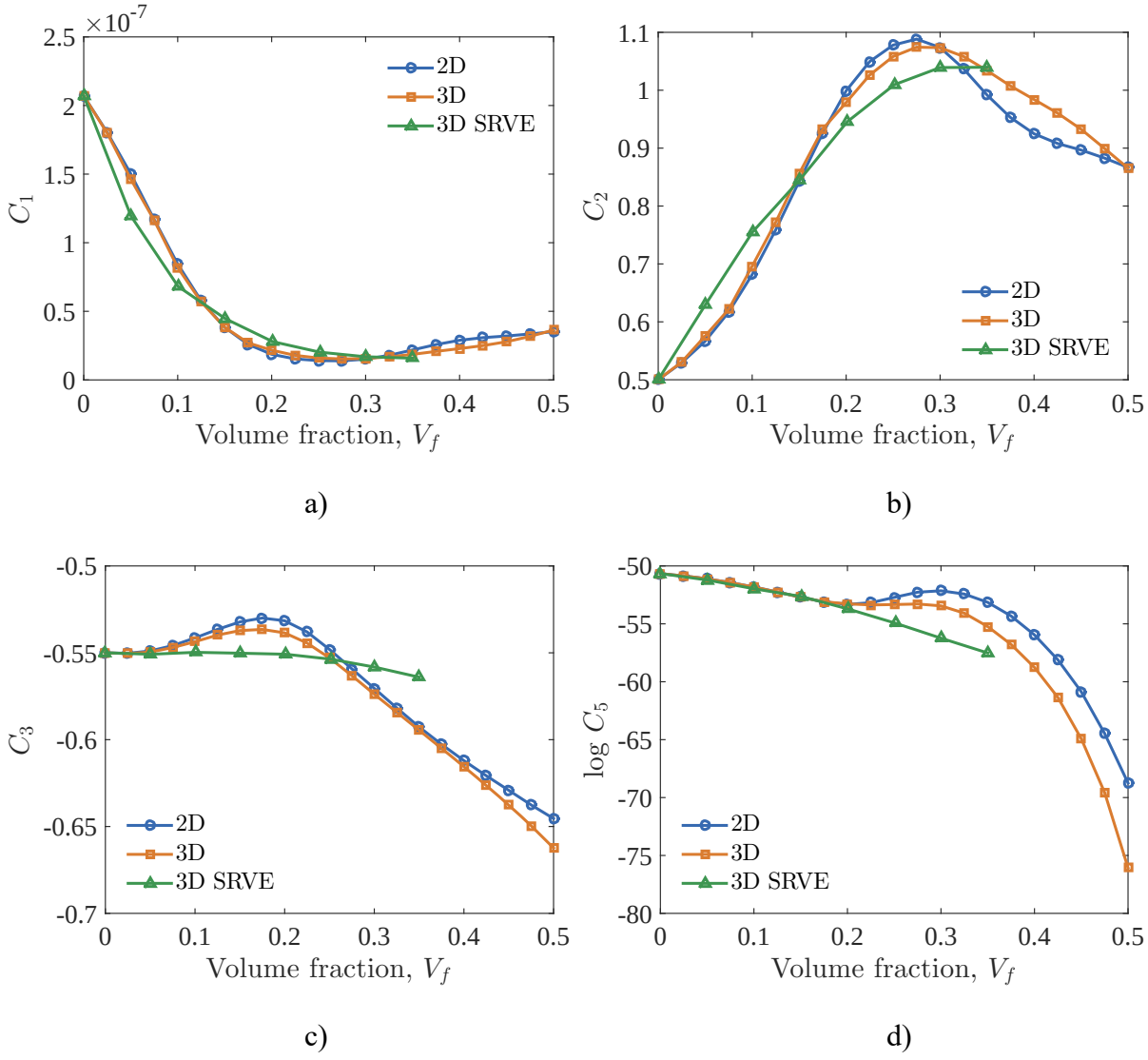

Figure 5.15: Dependence of creep parameters on SiC volume fraction for different type of models

(Figure 5.15 continued)

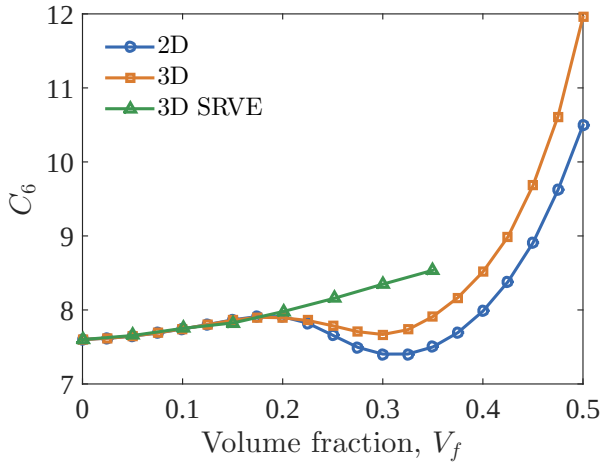

e)

Up to this point, the creep behavior at the microscopic level for a range of inclusion volume fraction has been determined. To demonstrate applicability of the multiscale approach, an Al/SiC FGM hollow cylinder subjected to pressure loadings is considered. The SiC composition (constituent 2) smoothly varies in the radial direction, from V_a at the inner to V_b at the outer surface of the cylinder. The hollow-cylinder has an internal radius $a = 1$ m and an outer radius $b = 1.2$ m is subjected to a uniform pressure $p_a = 15$ MPa on its inner surface.

5.3.2 Results of macroscopic creep analysis

A 2D axisymmetric finite element model using ANSYS MAPDL is used to analyze the macroscopic creep behavior of the FG thick-cylinder for different volume fraction profiles. The finite element is meshed with 8-noded quadrilateral (PLANE183) elements. The volume fraction of constituent 2 at each location over the domain are determined from the gradation profile, and assigned to each node as an initial state variable $V_2(r) \in [0,1]$. The fraction of the two constituents add up to 1, i.e. $V_1 + V_2 = 1$. The homogenized thermoelastic properties are calculated using the

Mori-Tanaka [66], Rosen-Hashin [70], and Hatta-Taya [69] schemes. The effective creep properties for range of field-variable values are determined using the homogenization, ensemble averaging and surface fitting procedure. A macroscopic analysis is performed to obtain time-dependent stresses and strains. Validity of the time-dependent finite element results has already been established in Section 5.2.1.

Figure 5.16 illustrates the volume fraction profiles for different values of p for power-function (Eq. 4.11) for $V_a = 0$ and $V_b = 0.5$.

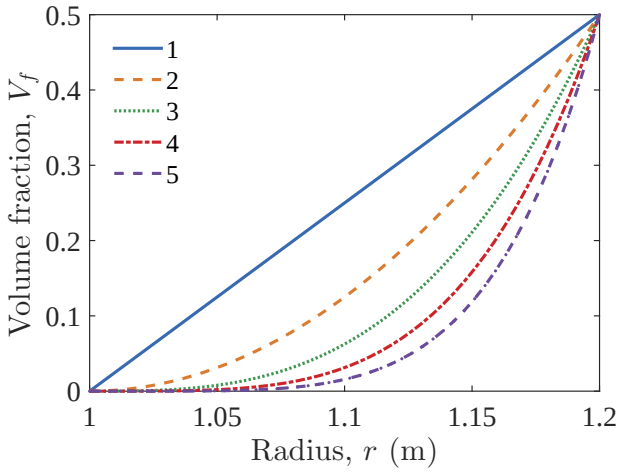

Figure 5.16: Power-function volume fraction profiles for different values of p ($V_a = 0, V_b = 0.5$)

As exponent p increases, the SiC content in the interior region (and the overall SiC content) of the cylinder decrease. The effect of parameter p is translated into the macroscopic problem through a change in thermoelastic and creep behavior within the cylinder.

Figure 5.17 shows the macroscopic creep strain histories at inner and outer surfaces, and stress distributions up to 150 h of creeping using the homogenized creep curves from the 2D micromechanical model. The composite is graded linearly ($p = 1$) in the radial direction with $V_a = 0$ and $V_b = 0.5$. The initial stress distribution curves (at $t = 0$) are also shown as dashed lines. Initially, the radial stress is compressive throughout the cylinder and is equal to -15 MPa

on the inner surface, and zero on the outer boundary surface, satisfying the imposed boundary conditions.

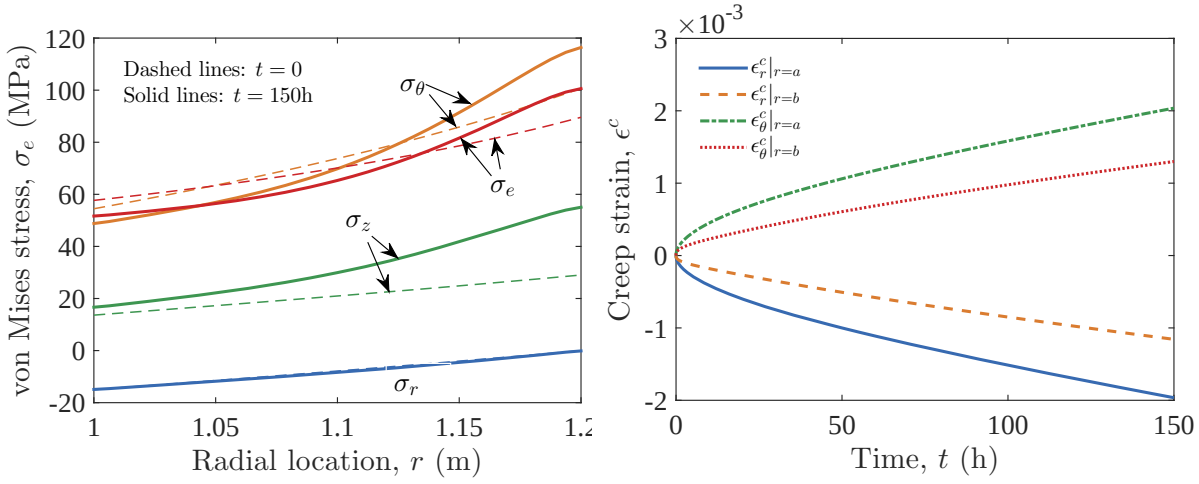

a) b)

Figure 5.17: a) Stress component distributions along the thickness, b) Evolution of creep strain components with time at different locations, (dotted lines indicate initial conditions, and the solid lines represent after reaching steady state)

Both tangential and axial stresses are tensile, and increases with increasing radius to attain a maximum at the outer surface. The effective stress also increases with increasing radius. With creep accumulation, the radial stress changes little, but the tangential stress is decreases at the inner surface, and increases at the outer surface. The axial stress component increases throughout the cylinder. Each section of the cylinder experiences a multiaxial state of time-varying stresses, whereas the creep model is generated from a uniaxial model. Since the maximum creep strain components are located at the inner surface of the cylinder, history of the tangential creep strain at the inner surface and von Mises effective stress distribution throughout the cylinder wall at steady state have been selected to represent the stress and creep strain situation in the following investigations.

5.3.2.1 Effects of using different micromechanical models

To compare the effects of different homogenization models, creep strains histories and von Mises stress distribution are shown in Figure 5.18. The macroscopic creep strain histories and steady-state stresses are found to be close for all three models. The 2D unit-cell model is fast and provides results close to those from the larger 3D models.

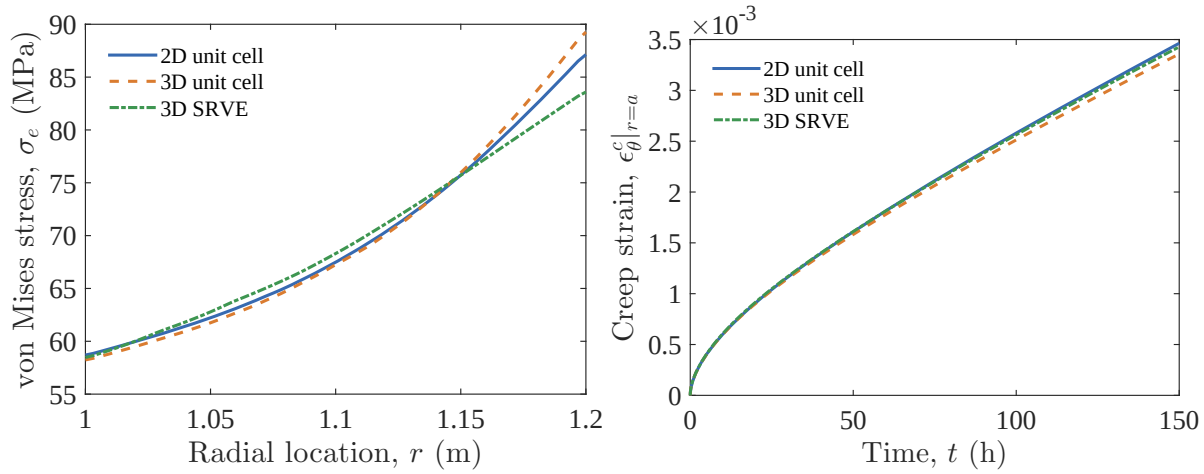

a) b)

Figure 5.18: Comparison of a) von Mises stress distribution, and b) evolution of maximum creep strain for different micromechanical models (2D, 3D, and 3D SRVE)

5.3.2.2 Parametric studies using thermoelastic creep model

Parametric studies are conducted for a FGM pressure vessel to examine the effect of boundary conditions on the creep strain and stress distributions. The hollow-cylinder is subjected to a uniform pressure p_a on its inner surface, and angular speed ω. The inner surface is held at the stress-free reference temperature $T_a = 0$, and the outer surface is exposed to a heat flux q. Figure 5.19 - Figure 5.21 show the creep strain history, and von Mises stress distribution for increased loadings. In all cases, the creep strain and von Mises stresses are higher throughout the cylinder.

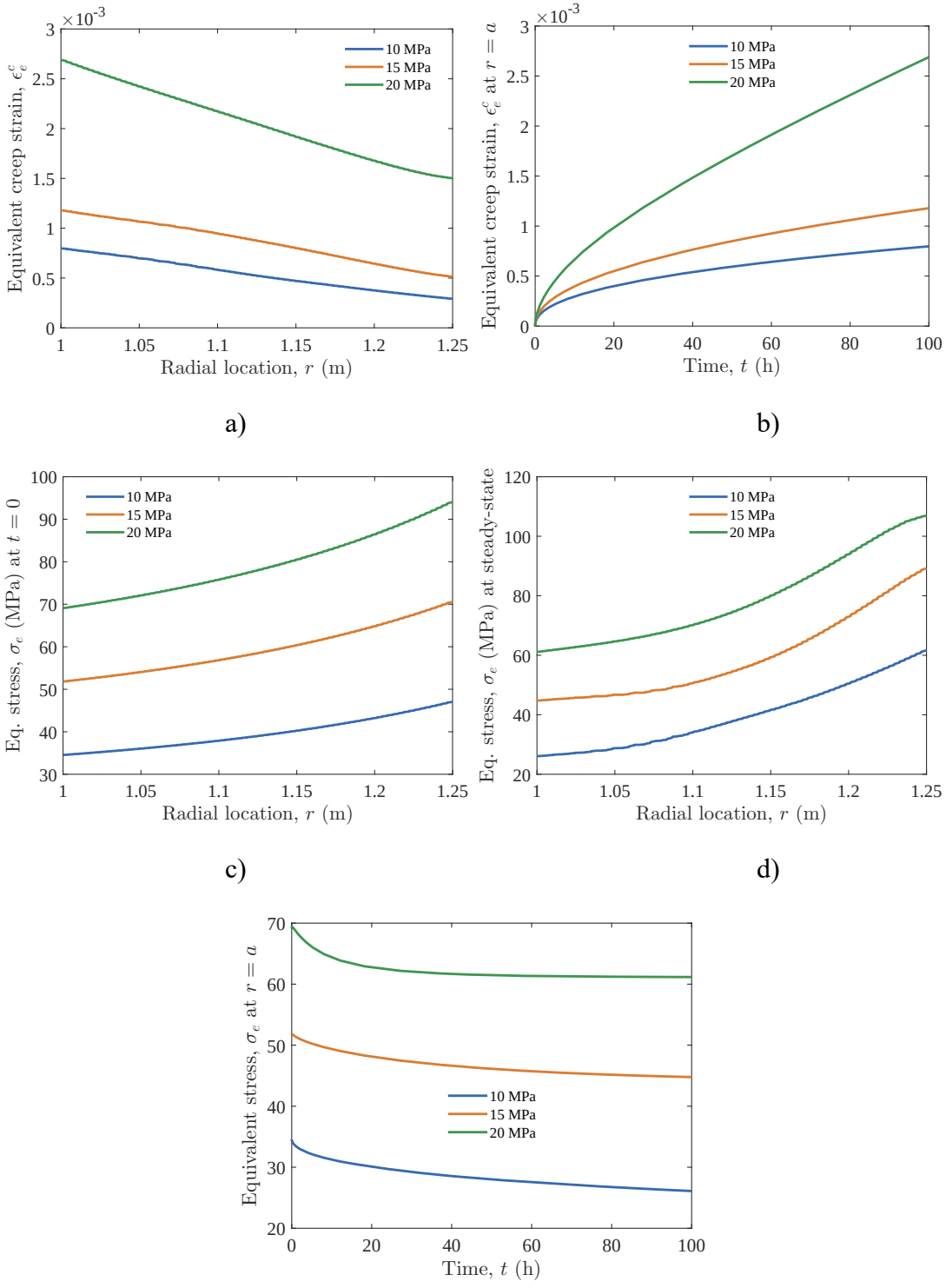

Figure 5.19: Effect of internal pressure p_a on a) equivalent creep strain along radius, b) equivalent creep strain history at $r = a$, c) equivalent stress distribution at $t = 0$, d) equivalent stress distribution at $t = 100$ h, and e) equivalent stress history at $r = a$, ($V_a = 0$, $V_b = 0.5$, $p = 1$)

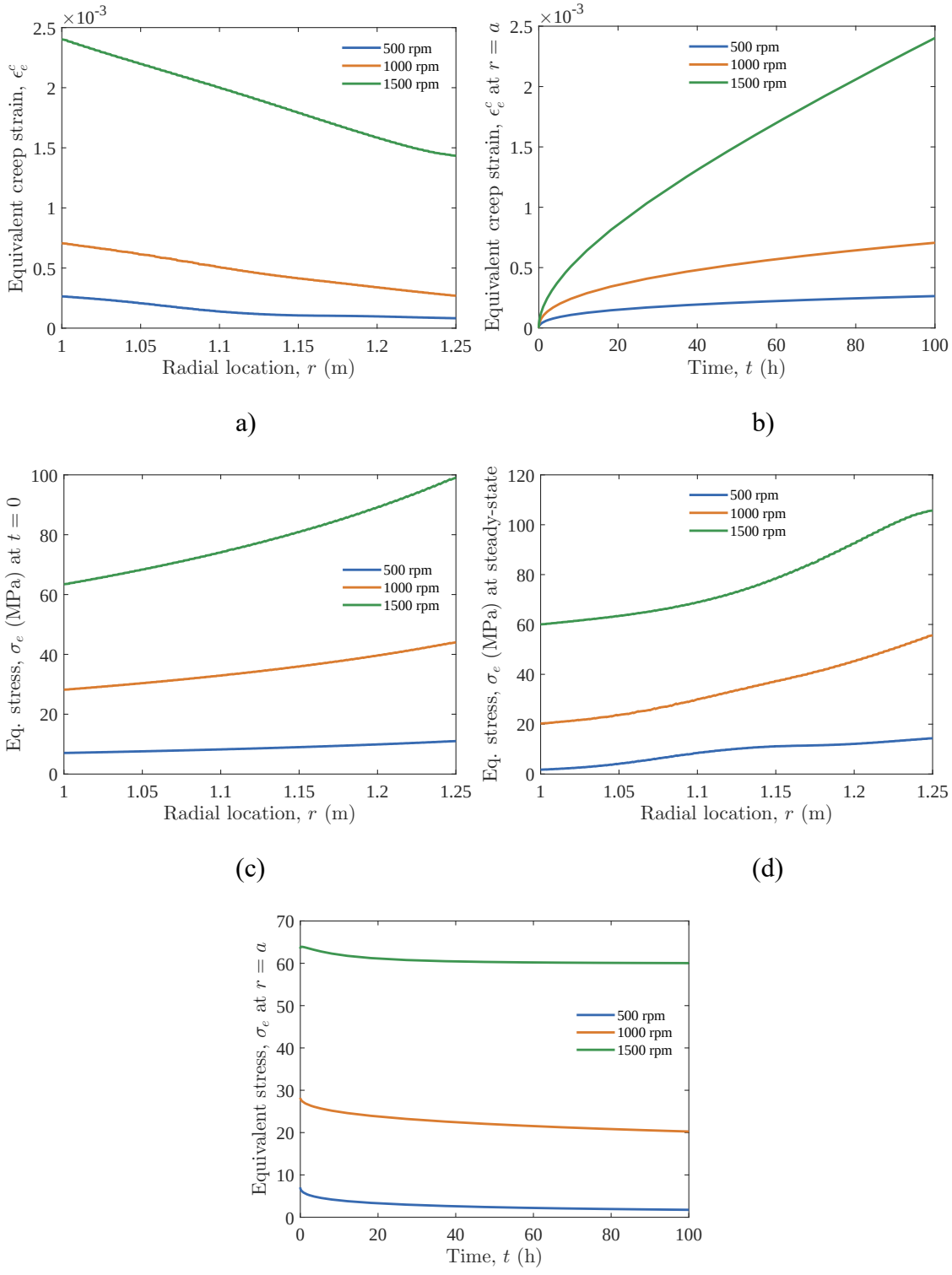

Figure 5.20: Effect of angular speed ω on a) equivalent creep strain along radius, b) equivalent creep strain history at $r = a$, c) equivalent stress distribution at $t = 0$, d) equivalent stress distribution at $t = 100$ h, and e) equivalent stress history at $r = a$, ($V_a = 0, V_b = 0.5, p = 1$)

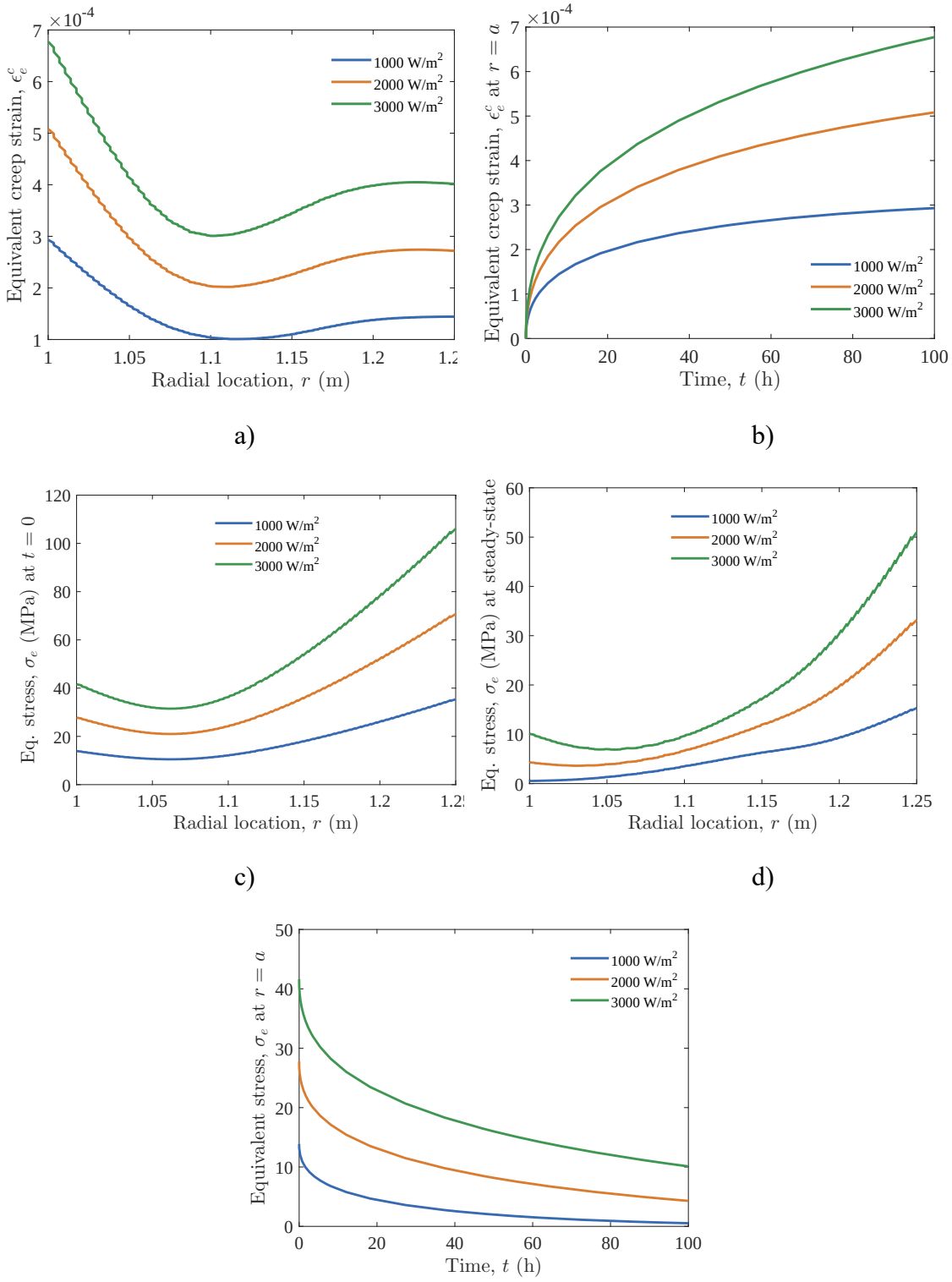

Figure 5.21: Effect of heat flux q on a) equivalent creep strain along radius, b) equivalent creep strain history at $r = a$, c) equivalent stress distribution at $t = 0$, d) equivalent stress distribution at $t = 100$ h, and e) equivalent stress history at $r = a$, ($V_a = 0, V_b = 0.5, p = 1$)

5.4 Multi-objective optimization results

Table 5.3 lists the loading data and multi-objective particle swarm optimization (MOPSO) parameters used in the optimization study. Figure 5.25 shows the Pareto front and non-dominated solutions obtained from five individual runs to minimize maximum stress and creep strain.

Table 5.3: Geometry, loading, and MOPSO parameters

FGM geometry, loading, and MOPSO parameters	
Inner radius, $a = 1$ m	Repository size $= 100$
Outer radius, $b = 1.25$ m	Initial inertial weight, $w = 0.9$
Internal pressure, $p_a = 10$ MPa	Personal learning coefficient, $c_1 = 2$
Angular speed, $\omega = 500$ rpm	Global learning coefficient, $c_2 = 2$
Heat flux, $q = 10{,}000$ W/m^2	Number of grids per dimension $= 7$
Inner temperature, $T_a = 0$	Inflation rate $= 0.1$
	Leader selection pressure, $\beta = 2$
Maximum iteration $= 200$	Deletion selection pressure, $\gamma = 2$
Swarm population size $= 8$	Mutation rate, $\mu = 0.1$

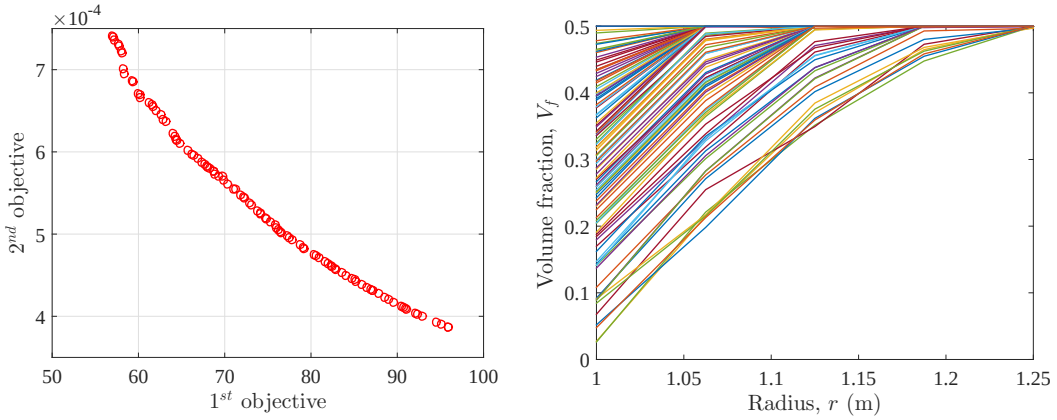

a) b)

Figure 5.22: a) Pareto front, and b) corresponding non-dominated solutions obtained from five runs

CHAPTER 6: CONCLUSIONS AND RECOMMENDATIONS

6.1 Conclusions

To determine safety requirements of *functionally graded* (FG) pressure vessels, time-dependent structural integrity assessment procedures need to be established. Firstly, thermoelastic and time-dependent stress/strain solutions of a heat generating and rotating FG cylindrical vessel are studied in this paper. Individual material property profiles are described using power-functions. Exact solutions are obtained for thermoelastic stress and strain distributions. A numerical procedure based on successive solutions is employed to obtain time-varying stress and strain histories. Results are presented, which are useful for validation purposes of more complicated cases e.g. temperature dependent materials, more general material property distributions etc. The study provides valuable hints to material scientists and engineers in choosing material gradients for minimizing creep damage. Significant results and observations from this work are summarized as follows:

1. Temperature and initial stress distributions are strong functions of the radial variations of Young's modulus, coefficient of thermal expansion, thermal conductivity, and heat generation rate.

2. An objective of the work is the identification of qualitative trends. By increasing the gradient parameter for Young's modulus, effective stress due to internal pressure or rotation is reduced at the inner surface and increased at the outer surface. In case of rotation, increasing the density gradient index increases stresses throughout the cylinder. For heat generation in convective environment, increasing indices controlling Young's modulus, coefficient of thermal expansion and heat generation rate increase effective stresses throughout the cylinder, while increasing the thermal conductivity

gradient index reduces the stress profile. When the loading conditions are present together, parametric studies using the derived expressions will facilitate the determination of appropriate material property gradients favorable structural integrity of the cylinder.

3. Although a steady state creep constitutive equation is used, the time-dependent curves illustrate two stages of deformation: initial redistribution of stresses, followed by constant stress values. Stress redistribution take place until each point attains a steady creep rate compatible with the rest of the material.

4. With elapsing time, stresses approach steady-state values. Final stress levels depend upon the density and creep parameter distributions only. Gradual reduction of density and creep coefficient along the thickness improves creep resistance of the cylinder. Gradation of elastic modulus, thermal conductivity, and coefficient of thermal expansion affect strain rates only during the initial stage and does not contribute in long term creep behavior. The cylinder may experience peak stresses during initial redistribution. FE results are in good agreement with semi-analytical solutions. The findings have been published in [131].

FGMs are composed of gradually varying composition, with the possibility of hierarchical microstructures. In order to predict the time-dependent response at the macroscale, effects of microstructural features on the creep behavior need to be quantified. Multiscale techniques are effective in incorporating underlying deformation and failure mechanisms at smaller scales. However, limited work has been reported on the multiscale creep modeling of FGMs. A multiscale model has been developed to incorporate material properties of constituents into the creep study.

The framework relates the time-dependent behavior of the matrix into the micromechanical model, and further integrates it to the macroscopic model. At a local scale, the Mori-Tanaka scheme is used to estimate the homogenized elastic properties, and a finite-element based homogenization techniques is used to estimate the creep response. Creep characteristics are described by the combined time-hardening creep model. The model has been successfully implemented to study the time-histories of creep strains and stress distributions of FG thick-cylinder. The model has been further employed to compare the creep response of any internally pressurized cylinder (linearly graded) using three different micromechanical models: a) 2D axisymmetric unit cell, b) 3D unit cell, and c) 3D SRVE. It is found that the macroscopic stress-strain results based on the 2D single-inclusion micromechanical model are close to that obtained from more realistic 3D SRVE model, while providing computational simplicity. The framework is being currently used examine the influence on different composition profiles of Al-SiC_p the evolution of creep stresses and strains with time.

It is obvious that manufacturing guidance of functionally graded materials requires the availability of material properties depending upon the microstructural features. The application of non-linearities in RVEs opens the path to relating the macroscopic responses to material properties the microscale. Analytical and numerical analysis plays a crucial role in understanding functionally graded materials in absence of experimental mechanics theoretical comprehension of structural response in order to obtain outstanding properties through design at microstructural length scales. This work illustrates a numerical technique to provide insights into the creep behavior of FG cylinders. It is to be noted that MMCs are hugely affected by the fabrication process itself, so it is possible for experimental analysis to reveal different predictions. The procedure aims to develop

an efficient tool to investigate the general influence of functional gradation on the creep response of FG cylinders.

6.2 Recommendations for future work

1. The analytical formulation is being modified to include generalized plane strain formulation to investigate axial stresses developed due to closed ends.

2. The mechanical behaviors of particulate composites are influenced by the matrix-inclusion bonding. Interfaces often get weakened due to high residual stresses arising from mismatches in thermo-mechanical properties during fabrication. Sometimes, the bonding is intentionally weakened by the addition of a thin interphase material between the inclusion and matrix, to introduce beneficial improve properties such as the ability to withstand high residual stresses during processing, chemical compatibility, fracture toughness etc. However, it come at the expense of decreased creep and fatigue resistance of the composite. The effects of interface properties on the creep behavior of MMCs can be investigated.

3. Presently, the dissertation has only dealt with temperature independent material properties. For materials which experience large variations in temperature, the creep properties are sensitive to temperature. To account for temperature effects, the temperature range experienced by the material needs to be considered to adjust the fitting-parameters. The multiscale model can be modified to study the effects of elevated temperatures and temperature-dependent material properties on the creep behavior of FG cylinders.

REFERENCES

1. Grujicic, M. and Y. Zhang. (1998). Determination of effective elastic properties of functionally graded materials using Voronoi cell finite element method. *Materials Science and Engineering: A,* 251(1-2), 64-76.

2. Rodel, J. (2005). Modelling of FGM-behaviour under extreme temperature and high-rate loading conditions. *Functionally graded materials: Properties, Modeling and Applications Part III.*

3. Xin, L., G. Dui, S. Yang, and D. Zhou. (2015). Solutions for behavior of a functionally graded thick-walled tube subjected to mechanical and thermal loads. *International Journal of Mechanical Sciences,* 98, 70-79.

4. Silva, E.C.N., M.C. Walters, and G.H. Paulino. (2006). Modeling bamboo as a functionally graded material: lessons for the analysis of affordable materials. *Journal of Materials Science,* 41(21), 6991-7004.

5. Ghavami, K. (2005). Bamboo as reinforcement in structural concrete elements. *Cement and Concrete Composites,* 27(6), 637-649.

6. Moreno, A. (2005). FGM in technology: needs and applications. *Functionally graded materials: Properties, Modeling and Applications Part IV.*

7. Vel, S.S. and A.J. Goupee. (2010). Multiscale thermoelastic analysis of random heterogeneous materials Part I: Microstructure characterization and homogenization of material properties. *Computational Materials Science,* 48(1), 22-38.

8. ANSYS® Academic Research, Release 16.0-17.2, ANSYS Documentation, ANSYS, Inc.

9. Dai, H.-L., Y.-N. Rao, and T. Dai. (2016). A review of recent researches on FGM cylindrical structures under coupled physical interactions, 2000–2015. *Composite Structures,* 152, 199-225.

10. Tutuncu, N. and M. Ozturk. (2001). Exact solutions for stresses in functionally graded pressure vessels. *Composites Part B: Engineering,* 32(8), 683-686.

11. Xiang, H., Z. Shi, and T. Zhang. (2006). Elastic analyses of heterogeneous hollow cylinders. *Mechanics Research Communications,* 33(5), 681-691.

12. Tutuncu, N. (2007). Stresses in thick-walled FGM cylinders with exponentially-varying properties. *Engineering Structures,* 29(9), 2032-2035.

13. Chen, Y.Z. and X.Y. Lin. (2008). Elastic analysis for thick cylinders and spherical pressure vessels made of functionally graded materials. *Computational Materials Science,* 44(2), 581-587.

14. Tutuncu, N. and B. Temel. (2009). A novel approach to stress analysis of pressurized FGM cylinders, disks and spheres. *Composite Structures,* 91(3), 385-390.

15. Li, X.-F. and X.-L. Peng. (2009). A Pressurized Functionally Graded Hollow Cylinder with Arbitrarily Varying Material Properties. *Journal of Elasticity,* 96(1), 81-95.

16. Afshar, R., M. Bayat, R.K. Lalwani, and Y.H. Yau. (2011). Elastic behavior of glass-like functionally graded infinite hollow cylinder under hydrostatic loads using finite element method. *Materials & Design,* 32(2), 781-787.

17. Sburlati, R. (2012). Analytical elastic solutions for pressurized hollow cylinders with internal functionally graded coatings. *Composite Structures,* 94(12), 3592-3600.

18. Nejad, M., M. Jabbari, and M. Ghannad. (2015). Elastic analysis of axially functionally graded rotating thick cylinder with variable thickness under non-uniform arbitrarily pressure loading. *International Journal of Engineering Science,* 89.

19. Tarn, J.-Q. (2001). Exact solutions for functionally graded anisotropic cylinders subjected to thermal and mechanical loads. *International Journal of Solids and Structures,* 38(46-47), 8189-8206.

20. Jabbari, M., S. Sohrabpour, and M.R. Eslami. (2002). Mechanical and thermal stresses in a functionally graded hollow cylinder due to radially symmetric loads. *International Journal of Pressure Vessels and Piping,* 79(7), 493-497.

21. Liew, K.M., S. Kitipornchai, X.Z. Zhang, and C.W. Lim. (2003). Analysis of the thermal stress behaviour of functionally graded hollow circular cylinders. *International Journal of Solids and Structures,* 40(10), 2355-2380.

22. Ruhi, M., A. Angoshtari, and R. Naghdabadi. (2005). Thermoelastic analysis of thick-walled finite-length cylinders of functionally graded materials. *Journal of Thermal Stresses,* 28(4), 391-408.

23. Shao, Z.S. (2005). Mechanical and thermal stresses of a functionally graded circular hollow cylinder with finite length. *International Journal of Pressure Vessels and Piping,* 82(3), 155-163.

24. Jabbari, M., A. Bahtui, and M.R. Eslami. (2009). Axisymmetric mechanical and thermal stresses in thick short length FGM cylinders. *International Journal of Pressure Vessels and Piping,* 86(5), 296-306.

25. Jabbari, M., A. Bahtui, and M.R. Eslami. (2006). Axisymmetric mechanical and thermal stresses in thick long FGM cylinders. *Journal of Thermal Stresses,* 29(7), 643-663.

26. Pelletier, J.L. and S.S. Vel. (2006). An exact solution for the steady-state thermoelastic response of functionally graded orthotropic cylindrical shells. *International Journal of Solids and Structures,* 43(5), 1131-1158.

27. Kordkheili, S.A.H. and R. Naghdabadi. (2007). Thermoelastic analysis of functionally graded cylinders under axial loading. *Journal of Thermal Stresses,* 31(1), 1-17.

28. Shao, Z.S., K.K. Ang, J.N. Reddy, and T.J. Wang. (2008). Nonaxisymmetric thermomechanical analysis of functionally graded hollow cylinders. *Journal of Thermal Stresses,* 31(6), 515-536.

29. Peng, X.L. and X.F. Li. (2010). Thermoelastic analysis of a cylindrical vessel of functionally graded materials. *International Journal of Pressure Vessels and Piping,* 87(5), 203-210.

30. Zhang, Q., Z.W. Wang, C.Y. Tang, D.P. Hu, P.Q. Liu, and L.Z. Xia. (2012). Analytical solution of the thermo-mechanical stresses in a multilayered composite pressure vessel considering the influence of the closed ends. *International Journal of Pressure Vessels and Piping,* 98.

31. Mehrabadi, S.J. and B.S. Aragh. (2013). On the thermal analysis of 2-D temperature-dependent functionally graded open cylindrical shells. *Composite Structures,* 96, 773-785.

32. Leu, S.Y. and L.C. Chien. (2015). Thermoelastic analysis of functionally graded rotating disks with variable thickness involving non-uniform heat source. *Journal of Thermal Stresses,* 38(4), 415-426.

33. Eraslan, A.N. (2003). Thermally induced deformations of composite tubes subjected to a nonuniform heat source. *Journal of Thermal Stresses,* 26, 167-193.

34. Eraslan, A.N. and T. Akis. (2006). Plane strain analytical solutions for a functionally graded elastic–plastic pressurized tube. *International Journal of Pressure Vessels and Piping,* 83(9), 635-644.

35. Ozturk, A. and M. Gulgec. (2011). Elastic–plastic stress analysis in a long functionally graded solid cylinder with fixed ends subjected to uniform heat generation. *International Journal of Engineering Science,* 49(10), 1047-1061.

36. Parvizi, A., R. Naghdabadi, and J. Arghavani. (2011). Analysis of Al A359/SiCp Functionally Graded Cylinder Subjected to Internal Pressure and Temperature Gradient with Elastic-Plastic Deformation. *Journal of Thermal Stresses,* 34(10), 1054-1070.

37. Nejad, M.Z. and P. Fatehi. (2015). Exact elasto-plastic analysis of rotating thick-walled cylindrical pressure vessels made of functionally graded materials. *International Journal of Engineering Science,* 86, 26-43.

38. Khoshgoftar, M.J., G.A. Arani, and M. Arefi. (2009). Thermoelastic analysis of a thick walled cylinder made of functionally graded piezoelectric material. *Smart Materials and Structures,* 18(11).

39. Dai, H.-L., L. Hong, Y.-M. Fu, and X. Xiao. (2010). Analytical solution for electromagnetothermoelastic behaviors of a functionally graded piezoelectric hollow cylinder. *Applied Mathematical Modelling,* 34(2), 343-357.

40. Dai, H.-L., Y.-N. Rao, and H.-J. Jiang. (2011). An analytical method for magnetothermoelastic analysis of functionally graded hollow cylinders. *Applied Mathematics and Computation,* 218(4), 1467-1477.

41. Arani, G.A., K.Z. Maraghi, M.R. Mozdianfard, and A.R. Shajari. (2011). Thermo-piezo-magneto-mechanical stresses analysis of FGPM hollow rotating thin disk. *International Journal of Mechanics and Materials in Design,* 6(4), 341-349.

42. Bayat, M., M. Rahimi, M. Saleem, A.H. Mohazzab, I. Wudtke, and H. Talebi. (2014). One-dimensional analysis for magneto-thermo-mechanical response in a functionally graded annular variable-thickness rotating disk. *Applied Mathematical Modelling,* 38(19-20), 4625-4639.

43. Zenkour, A.M. (2014). Hygrothermoelastic responses of inhomogeneous piezoelectric and exponentially graded cylinders. *International Journal of Pressure Vessels and Piping,* 119, 8-18.

44. Atrian, A., J. Jafari Fesharaki, and S.H. Nourbakhsh. (2015). Thermo-electromechanical behavior of functionally graded piezoelectric hollow cylinder under non-axisymmetric loads. *Applied Mathematics and Mechanics,* 36(7), 939-954.

45. You, L.H., H. Ou, and Z.Y. Zheng. (2007). Creep deformations and stresses in thick-walled cylindrical vessels of functionally graded materials subjected to internal pressure. *Composite Structures,* 78(2), 285-291.

46. You, L.H. and H. Ou. (2008). Steady-State Creep Analysis of Thick-Walled Spherical Pressure Vessels With Varying Creep Properties. *Journal of Pressure Vessel Technology,* 130(1).

47. Gupta, V.K. and T. Singh. (2009). Creep analysis of an internally pressurized thick cylinder made of a functionally graded composite. *The Journal of Strain Analysis for Engineering Design,* 44(7), 583-594.

48. Singh, T. and V.K. Gupta. (2010). Modeling Steady State Creep in Functionally Graded Thick Cylinder Subjected to Internal Pressure. *Journal of Composite Materials,* 44(11), 1317-1333.

49. Chen, J., K. Yoon, and S.-T. Tu. (2011). Creep Behavior of Pressurized Tank Composed of Functionally Graded Materials. *Journal of Pressure Vessel Technology,* 133(5).

50. Nejad, M.Z., Z. Hoseini, A. Niknejad, and M. Ghannad. (2014). Steady-State Creep Deformations and Stresses in FGM Rotating Thick Cylindrical Pressure Vessels. *Journal of Mechanics,* 31(1), 16.

51. Yang, Y.Y. (2000). Time-dependent stress analysis in functionally graded materials. *International Journal of Solids and Structures,* 37(51), 7593-7608.

52. Chen, J., S. Tu, F. Xuan, and Z. Wang. (2007). Creep analysis for a functionally graded cylinder subjected to internal and external pressure. *The Journal of Strain Analysis for Engineering Design,* 42(2), 69-77.

53. Loghman, A., A.G. Arani, S. Amir, and A. Vajedi. (2010). Magnetothermoelastic creep analysis of functionally graded cylinders. *International Journal of Pressure Vessels and Piping,* 87(7), 389-395.

54. Singh, T. and V.K. Gupta. (2011). Effect of anisotropy on steady state creep in functionally graded cylinder. *Composite Structures,* 93(2), 747-758.

55. Loghman, A., A. Ghorbanpour Arani, and S.M.A. Aleayoub. (2011). Time-dependent creep stress redistribution analysis of thick-walled functionally graded spheres. *Mechanics of Time-Dependent Materials,* 15(4), 353-365.

56. Loghman, A. and M. Moradi. (2012). The analysis of time-dependent creep in FGPM thick walled sphere under electro-magneto-thermo-mechanical loadings. *Mechanics of Time-Dependent Materials,* 17(3), 315-329.

57. Jafari Fesharaki, J., A. Loghman, M. Yazdipoor, and S. Golabi. (2013). Semi-analytical solution of time-dependent thermomechanical creep behavior of FGM hollow spheres. *Mechanics of Time-Dependent Materials,* 18(1), 41-53.

58. Nejad, M.Z. and M.D. Kashkoli. (2014). Time-dependent thermo-creep analysis of rotating FGM thick-walled cylindrical pressure vessels under heat flux. *International Journal of Engineering Science,* 82, 222-237.

59. Qu, D.D., W.W. Basuki, and J. Aktaa. (2015). Numerical assessment of functionally graded tungsten/EUROFER coating system for first wall applications. *Fusion Engineering and Design,* 98, 1389-1393.

60. Golmakaniyoon, S. and F. Akhlaghi. (2016). Time-dependent creep behavior of Al–SiC functionally graded beams under in-plane thermal loading. *Computational Materials Science,* 121, 182-190.

61. Goshima, T. and K. Miyao. (1991). Transient thermal stresses in a hollow cylinder subjected to γ-ray heating and convective heat losses. *Nuclear Engineering and Design,* 125(2), 267-273.

62. Aziz, A. and M. Torabi. (2013). Thermal stresses in a hollow cylinder with convective boundary conditions on the inside and outside surfaces. *Journal of Thermal Stresses,* 36(10), 1096-1111.

63. Zhang, H.W., D.S. Yang, S. Zhang, and Y.G. Zheng. (2014). Multiscale nonlinear thermoelastic analysis of heterogeneous multiphase materials with temperature-dependent properties. *Finite Elements in Analysis and Design,* 88, 97-117.

64. Li, D.-F., B.J. Golden, and N.P. O'Dowd. (2014). Multiscale modelling of mechanical response in a martensitic steel: A micromechanical and length-scale-dependent framework for precipitate hardening. *Acta Materialia,* 80, 445-456.

65. Ubachs, R.L.J.M., O. van der Sluis, W.D. van Driel, and G.Q. Zhang. (2006). Multiscale modelling of multilayer substrates. *Microelectronics Reliability,* 46(9-11), 1472-1477.

66. Mori, T. and K. Tanaka. (1973). Average stress in matrix and average elastic energy of materials with misfitting inclusions. *Acta Metallurgica,* 21(5), 571-574.

67. Hill, R. (1965). A self-consistent mechanics of composite materials. *Journal of the Mechanics and Physics of Solids,* 13(4), 213-222.

68. Hashin, Z. and S. Shtrikman. (1963). A variational approach to the theory of the elastic behaviour of multiphase materials. *Journal of the Mechanics and Physics of Solids,* 11(2), 127-140.

69. Hatta, H. and M. Taya. (1985). Effective thermal conductivity of a misoriented short fiber composite. *Journal of Applied Physics,* 58(7), 2478-2486.

70. Rosen, B.W. and Z. Hashin. (1970). Effective thermal expansion coefficients and specific heats of composite materials. *International Journal of Engineering Science,* 8(2), 157-173.

71. Benveniste, Y. (1986). On the effective thermal conductivity of multiphase composites. *Zeitschrift für angewandte Mathematik und Physik ZAMP,* 37(5), 696-713.

72. Llorca, J. and J. Segurado. (2004). Three-dimensional multiparticle cell simulations of deformation and damage in sphere-reinforced composites. *Materials Science and Engineering: A,* 365(1-2), 267-274.

73. Kari, S., H. Berger, R. Rodriguez-Ramos, and U. Gabbert. (2007). Computational evaluation of effective material properties of composites reinforced by randomly distributed spherical particles. *Composite Structures,* 77(2), 223-231.

74. Yang, L., Y. Yan, Z. Ran, and Y. Liu. (2013). A new method for generating random fibre distributions for fibre reinforced composites. *Composites Science and Technology,* 76, 14-20.

75. Bouafia, F., B. Serier, and B.A.B. Bouiadjra. (2012). Finite element analysis of the thermal residual stresses of SiC particle reinforced aluminum composite. *Computational Materials Science,* 54, 195-203.

76. Alfonso, I., I.A. Figueroa, J.M. Sierra, M. Abatal, G. Gonzalez, V. Rodriguez-Iglesias, A. Medina-Flores, and J.E. Flores. (2013). Young's modulus estimation based on high symmetry 3-D finite element model for metal matrix composites. *Computational Materials Science,* 69, 304-310.

77. Barbera, D., H.F. Chen, and Y.H. Liu. (2015). On the creep fatigue behavior of metal matrix composites. *Procedia Engineering,* 130, 1121-1136.

78. Sharma, N.K., R.K. Mishra, and S. Sharma. (2016). 3D micromechanical analysis of thermo-mechanical behavior of Al2O3/Al metal matrix composites. *Computational Materials Science,* 115, 192-201.

79. Kwok, K., D. Boccaccini, Å.H. Persson, and H.L. Frandsen. (2016). Homogenization of steady-state creep of porous metals using three-dimensional microstructural reconstructions. *International Journal of Solids and Structures,* 78-79, 38-46.

80. Yin, H.M., G.H. Paulino, W.G. Buttlar, and L.Z. Sun. (2005). Effective thermal conductivity of two-phase functionally graded particulate composites. *Journal of Applied Physics,* 98(6).

81. Muliana, A.H. (2009). A micromechanical model for predicting thermal properties and thermo-viscoelastic responses of functionally graded materials. *International Journal of Solids and Structures,* 46(9), 1911-1924.

82. Huet. (1990). Application of variational concepts to size effects in elastic heterogeneous bodies. *Journal of the Mechanics and Physics of Solids,* 38, 813-841.

83. Cho, Y.J., W.J. Lee, and Y.H. Park. (2014). Effect of boundary conditions on the numerical solutions of representative volume element problems for random heterogeneous composite microstructures. *Metals and Materials International,* 20(6), 1085-1093.

84. Cho, Y.J., W.J. Lee, and Y.H. Park. (2015). Effect of boundary conditions on plasticity and creep behavior analysis of particle reinforced composites by representative volume element approach. *Computational Materials Science,* 100, 67-75.

85. Mondali, M., A. Abedian, and A. Ghavami. (2009). A new analytical shear-lag based model for prediction of the steady state creep deformations of some short fiber composites. *Materials & Design,* 30(4), 1075-1084.

86. Ghavami, A., A. Abedian, and M. Mondali. (2010). Finite difference solution of steady state creep deformations in a short fiber composite in presence of fiber/matrix debonding. *Materials & Design,* 31(5), 2616-2624.

87. Monfared, V., M. Mondali, and A. Abedian. (2013). Novel mathematical approaches for analyzing time dependent creep deformations in reinforced metals. *Journal of Mechanical Science and Technology,* 27(11), 3277-3285.

88. Park, Y.H. and J.W. Holmes. (1992). Finite element modelling of creep deformation in fibre-reinforced ceramic composites. *Journal of Materials Science,* 27(23), 6341-6351.

89. Lee, W.J., J.H. Son, I.M. Park, J.-J. Oak, H. Kimura, and Y.H. Park. (2010). Analysis of 3D random Al18B4O33 whisker reinforced Mg composite using FEM and Random Sequential Adsorption. *Materials Transactions,* 51(6), 1089-1093.

90. Lee, W.J., S.K. Jo, I.M. Park, and Y.H. Park. (2011). The effect of reinforcement clustering on the steady-state creep behaviors of discontinuous metal matrix composite: A possible origin of 'anomalously high' stress exponent. *Materials Science and Engineering: A,* 528(13-14), 4564-4568.

91. Lee, W. (2014). Practical applicability and limitation of representative volume element approach to model creep behaviors of metal matrix composites. *Materials transactions,* 55(9).

92. Krajewski, P.E., J.W. Jones, and J.E. Allison. (1995). The effect of particle reinforcement on the creep behavior of single-phase aluminum. *Metallurgical and Materials Transactions A,* 26(12), 3107-3118.

93. Yu, C.H., M.W. Bird, C.W. Huang, C.S. Chen, Y.F. Gao, K.W. White, and C.H. Hsueh. (2014). Micromechanics modeling of creep fracture of zirconium diboride–silicon carbide composites at 1400–1700°C. *Journal of the European Ceramic Society,* 34(16), 4145-4155.

94. Ghosh, S., Y. Ling, B. Majumdar, and R. Kim. (2000). Interfacial debonding analysis in multiple fiber reinforced composites. *Mechanics of Materials,* 32(10), 561-591.

95. Tvergaard, V. (2003). Debonding of short fibres among particulates in a metal matrix composite. *International Journal of Solids and Structures,* 40(25), 6957-6967.

96. Benabou, L., N.t.M. Abdelaziz, and N. Benseddiq. (2004). Effective properties of a composite with imperfectly bonded interface. *Theoretical and Applied Fracture Mechanics,* 41(1-3), 15-20.

97. Mondal, D.P., N. Ramakrishnan, and S. Das. (2006). FEM modeling of the interface and its effect on the elastio-plastic behavior of metal matrix composites. *Materials Science and Engineering: A,* 433(1-2), 286-290.

98. Romanowicz, M. (2009). Effect of interfacial debonding on the failure behavior in a fiber-reinforced composite subjected to transverse tension. *Computational Materials Science,* 47(1), 225-231.

99. Kulkarni, M., D. Carnahan, K. Kulkarni, D. Qian, and J.L. Abot. (2010). Elastic response of a carbon nanotube fiber reinforced polymeric composite: A numerical and experimental study. *Composites Part B: Engineering,* 41(5), 414-421.

100. Yuan, M.N., Y.Q. Yang, C. Li, P.Y. Heng, and L.Z. Li. (2012). Numerical analysis of the stress–strain distributions in the particle reinforced metal matrix composite SiC/6064Al. *Materials & Design,* 38, 1-6.

101. Wang, H.W., H.W. Zhou, H.W. Ji, and X.C. Zhang. (2014). Application of extended finite element method in damage progress simulation of fiber reinforced composites. *Materials & Design,* 55, 191-196.

102. Aghdam, M.M. and S.R. Morsali. (2014). Effects of manufacturing parameters on residual stresses in SiC/Ti composites by an elastic–viscoplastic micromechanical model. *Computational Materials Science,* 91, 62-67.

103. Aghdam, M.M., S.M.A. Hosseini, and S.R. Morsali. (2015). Simulation of interface damage in metal matrix composites under off-axis loading using cohesive zone model. *Computational Materials Science,* 108, 42-47.

104. Goto, S. and M. McLean. (1989). Modelling interface effects during creep of metal matrix composites. *Scripta Metallurgica,* 23(12), 2073-2078.

105. Mondali, M., A. Abedian, and S. Adibnazari. (2005). FEM study of the second stage creep behavior of Al6061/SiC metal matrix composite. *Computational Materials Science,* 34(2), 140-150.

106. Pan, Y., G.J. Weng, S.A. Meguid, W.S. Bao, Z.H. Zhu, and A.M.S. Hamouda. (2013). Interface effects on the viscoelastic characteristics of carbon nanotube polymer matrix composites. *Mechanics of Materials,* 58, 1-11.

107. Sivakumar, R., T. Nishikawa, S. Honda, H. Awaji, and F.D. Gnanam. (2003). Processing of mullite–molybdenum graded hollow cylinders by centrifugal molding technique. *Journal of the European Ceramic Society,* 23(5), 765-772.

108. Rajan, T.P.D., R.M. Pillai, and B.C. Pai. (2010). Characterization of centrifugal cast functionally graded aluminum-silicon carbide metal matrix composites. *Materials Characterization,* 61(10), 923-928.

109. Lin, X., C. Liu, and H. Xiao. (2013). Fabrication of Al–Si–Mg functionally graded materials tube reinforced with in situ Si/Mg2Si particles by centrifugal casting. *Composites Part B: Engineering,* 45(1), 8-21.

110. Ulukoy, A., M. Topcu, and S. Tasgetiren. (2016). An Experimental Crack Propagation Analysis of Aluminum Matrix Functionally Graded Material. *Advances in Functionally Graded Materials and Structures.*

111. Zygmuntowicz, J., A. Miazga, K. Konopka, K. Edrysiak, and W. Kaszuwara. (2015). Alumina matrix ceramic-nickel composites formed by centrifugal slip casting. *Processing and Application of Ceramics,* 9(4), 199-202.

112. Farshi, B. and J. Bidabadi. (2008). Optimum design of inhomogeneous rotating discs under secondary creep. *International Journal of Pressure Vessels and Piping,* 85(7), 507-515.

113. Nemat-Alla, M. (2009). Reduction of thermal stresses by composition optimization of two-dimensional functionally graded materials. *Acta Mechanica,* 208(3-4), 147-161.

114. Boussaa, D. (2009). Optimization of temperature-dependent functionally graded material bodies. *Computer Methods in Applied Mechanics and Engineering,* 198(37-40), 2827-2838.

115. Na, K.-S. and J.-H. Kim. (2009). Optimization of volume fractions for functionally graded panels considering stress and critical temperature. *Composite Structures,* 89(4), 509-516.

116. Na, K.-S. and J.-H. Kim. (2010). Volume fraction optimization for step-formed functionally graded plates considering stress and critical temperature. *Composite Structures,* 92(6), 1283-1290.

117. Sadollah, A. and A. Bahreininejad. (2011). Optimum gradient material for a functionally graded dental implant using metaheuristic algorithms. *Journal of the mechanical behavior of biomedical materials,* 4(7), 1384-1395.

118. Kou, X.Y., G.T. Parks, and S.T. Tan. (2012). Optimal design of functionally graded materials using a procedural model and particle swarm optimization. *Computer-Aided Design,* 44(4), 300-310.

119. Fereidoon, A., F. Sadri, and H. Hemmatian. (2012). Functionally graded materials optimization using particle swarm-based algorithms. *Journal of Thermal Stresses,* 35(4), 377-392.

120. Chiba, R. and Y. Sugano. (2012). Optimisation of material composition of functionally graded materials based on multiscale thermoelastic analysis. *Acta Mechanica,* 223(5), 891-909.

121. Xu, Y., W. Zhang, D. Chamoret, and M. Domaszewski. (2012). Minimizing thermal residual stresses in C/SiC functionally graded material coating of C/C composites by using particle swarm optimization algorithm. *Computational Materials Science,* 61, 99-105.

122. Khanoki, S. and D. Pasini. (2012). Multiscale design and multiobjective optimization of orthopedic hip implants with functionally graded cellular material. *Journal of biomechanical engineering,* 134(3), 31004.

123. Noh, Y.J., Y.J. Kang, S.J. Youn, J.R. Cho, and O.K. Lim. (2013). Reliability-based design optimization of volume fraction distribution in functionally graded composites. *Computational Materials Science,* 69, 435-442.

124. Silva, T.A.N. and M.A.R. Loja. (2013). Differential Evolution on the Minimization of Thermal Residual Stresses in Functionally Graded Structures. *Differential Evolution on the Minimization of Thermal Residual Stresses in Functionally Graded Structures.*

125. Cormeau, I. (1975). Numerical stability in quasi-static elasto/visco-plasticity. *International Journal for Numerical Methods in Engineering,* 9(1), 109-127.

126. Wolfram Research, Inc., Mathematica, Version 8.0, Champaign, IL, 2010.

127. MATLAB Release 2013b, The MathWorks, Inc., Natick, Massachusetts, United States.

128. Coello, C.A.C. and M.S. Lechuga. (2002). MOPSO: a proposal for multiple objective particle swarm optimization. *Proceedings of the 2002 Congress on Evolutionary Computation, 2002. CEC '02,* 2, 1051-1056.

129. Reyes-Sierra, M.C.C., Carlos A. . (2006). Multi-Objective Particle Swarm Optimizers: A Survey of the State-of-the-Art. *International Journal of Computational Intelligence Research,* 2(3), 287-308.

130. Lee, W.J., J.H. Son, I.M. Park, and Y.H. Park. (2010). Direct numerical predictions for the steady-state creep deformation of extruded SiCw/Al6061 composites using a representative volume element with random arrangement of whiskers. *Computational Materials Science,* 48(4), 802-812.

131. Ahmed, J.A. and M.A. Wahab. (2015). Thermoelastic and creep analysis of a functionally graded rotating cylindrical vessel with internal heat generation. *World Journal of Engineering,* 12(6), 517-532.

VITA

Jasem Amjad Ahmed was born in Dhaka, Bangladesh in 1985. He graduated high school from European Standard School in 2004. He attended the Islamic University of Technology from 2004 to 2008 and received a Bachelor of Science in Mechanical Engineering. In August 2010, he enrolled in the Ph.D. program in Mechanical Engineering at the Louisiana State University, Baton Rouge. He worked as a Co-op for three semesters during 2014 and 2017 at ANSYS Inc., headquarters, located at Canonsburg, Pennsylvania.